Influence of the interface structure on the electronic transport in planar tunnel junctions: A first-principles investigation

Dissertation

zur Erlangung des akademischen Grades
doctor rerum naturalium (Dr. rer. nat.)

vorgelegt der
Naturwissenschaftlichen Fakultät II - Chemie und Physik
der Martin-Luther-Universität Halle-Wittenberg

von Diplom-Physiker Peter Bose
geboren am 08. Oktober 1979 in Lutherstadt Eisleben

Gutachter
1: Prof. Dr. Ingrid Mertig, Martin-Luther-Universität Halle-Wittenberg
2: Prof. Dr. Wolfram Hergert, Martin-Luther-Universität Halle-Wittenberg
3: Prof. Dr. Peter Dederichs, Forschungszentrum Jülich

Halle (Saale), den 14. Januar 2010

I don't like it, and I'm sorry I ever had anything to do with it.
Erwin Schrödinger

Everything we call real is made of things that cannot be regarded as real.
Niels Bohr

Contents

Publications **7**

1 Introduction **9**

2 Theoretical Background **11**

2.1 Density functional theory (DFT) 11

2.2 Electronic transport 15

2.2.1 Conductance viewed as transmission 15

2.2.2 Multiple-scattering theory 22

2.2.3 Scattering from layers 27

2.2.4 Bloch-wave scattering and conductance 31

2.2.5 Conductance for disordered interfaces 39

3 Selected Results and Discussion **49**

3.1 Fe(001)/FeO/MgO/Fe(001) 51

3.2 Fe(001)/x(Mn)/Vacuum/Fe(001) 57

3.3 Cr and Co interlayers in Fe/MgO/Fe magnetic tunnel junctions 62

4 Summary **79**

Bibliography **81**

Danksagung **87**

Eidestattliche Erklärung **89**

Curriculum vitae **91**

Publications

- J. Henk, P. Bose, T. Michael and P. Bruno: *"Spin motion of photoelectrons"* Physical Review B **68**, 052403 (2003)
- J. Henk, T. Michael, P. Bose and P. Bruno: *"Photoemission approach to spin motion in electron transmission through magnetic films"* Surface Science **566**, 252-255 (2004)
- P. Bose, J. Henk and I. Mertig: *"Spin-dependent tunneling in the nearly-free-electron model"* arXiv:cond-mat/0603207 (2005)
- P. Bose, J. Henk and I. Mertig: *"Oscillatory tunneling magnetoresistance caused by antiferromagnetic Mn layers"* Physical Review B **75**, 100402(R) (2007) **(see P58ff)**
- P. Bose, A. Ernst, I. Mertig and J. Henk: *"Large reduction of the magnetoresistance in Fe/MgO/Fe tunnel junctions due to small oxygen concentrations at a single FeO interface layer: A first-principles study"* Physical Review B **78**, 092403 (2008) **(see P53ff)**
- P. Bose, P. Zahn, J. Henk and I. Mertig: *"Tailoring TMR Ratios by Ultrathin Magnetic Interlayers: A First-principles Investigation of Fe/MgO/Fe"* in Novel Materials and Devices for Spintronics, edited by O.G. Heinonen, S. Sanvito, V.A. Dediu, N. Rizzo (Mater. Res. Soc. Symp. Proc. Volume **1183**, Warrendale, PA, 2009), 1183-FF07-02 **(see P64ff)**
- P. Bose, P. Zahn, J. Henk and I. Mertig: *"Tailoring TMR Ratios by Ultrathin Cr and Co Interlayers: A First-principles Investigation of Fe/MgO/Fe"* submitted to Physical Review B, preprint at http://arxiv.org/abs/1001.2322 **(see P70ff)**
- J. Henk, P. Zahn, P. Bose and I. Mertig: *"Oscillatory spin polarization in photoelectron spectroscopy from antiferromagnets: Cr films on Fe(110)"* submitted to Elsevier (2010)
- N.F. Hinsche, M. Fechner, P. Bose, S. Ostanin, J. Henk, P. Zahn and I. Mertig: *"Influence of the complex bandstructure to tunneling electroresistance in ferroelectric tunneljunctions: A combined model and ab-initio study"* submitted to Physical Review B (2010)

Chapter 1

Introduction

Since the discovery of the giant magnetoresitance (GMR) effect in the late 1980ies [1, 2] and its subsequent extensive use in read heads of modern hard drives and in magnetic sensors, the new field of spin transport electronics (spintronics) [3–6] became increasingly important. The latter — which is also known as magnetoelectronics — defines a new branch of technological devices which uses the quantum mechanical spin degree-of-freedom in addition to the electron's charge. Due to its associated magnetic moment the electron spin can be manipulated by means of magnetic fields. Its manipulation by spin-orbit coupling, e.g. by the Rashba effect [7], defines an additional field in spintronics.

The successful application of the GMR effect triggered a lot of research activities which focus on potential applications of similar magnetoresistive effects. As a consequence, the tunnel magnetoresistance effect (TMR) — which originally has been reported by Julliere in 1975 [8] — was rediscovered. Defined as $(R^{\mathrm{AP}}-R^{\mathrm{P}})/R^{\mathrm{P}}$ the TMR ratio expresses, in the optimistic definition, the asymmetry between parallel and anti-parallel resistances R in magnetic tunnel junctions (MTJs). The latter typically comprise an insulating tunnel barrier that is sandwiched between two ferromagnetic leads. The two magnetic-configurational dependent resistances, R^{P} and R^{AP}, are measured with respect to the parallel (P) and the anti-parallel (AP) alignment of the lead magnetizations.

The first TMR ratios measured at room temperature have been experimentally obtained with amorphous aluminum oxide tunnel barriers in 1995 [9]. Although the subsequent research of MTJs with these $\mathrm{Al_2O_3}$ barriers led to continuous improvements of the TMR ratios, they never exceeded 100% which would approve them for industrial devices [10]. This drawback has been overcome by the reorientation to epitaxial MTJs which comprise Fe(001) leads and crystalline MgO tunnel barriers (see Fig. 1.1). The first TMR measurements of about 200% [11, 12] made these tunnel junctions immediately attractive for potential applications, such as elements of magnetic random access memories (MRAMs) [13].

As can be seen in Fig. 1.1, the Fe(001)/MgO/Fe(001) MTJs exhibit due to their epitaxial growth conditions ordered geometrical structures. The latter are, because of their underlying translational symmetry, very suited for first-principles electronic transport calculations which base on density functional theory (DFT). In contrast to simple models, such as proposed by Julliere [8]

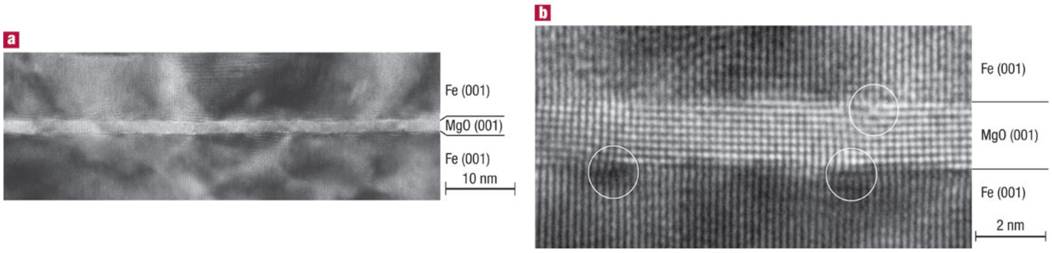

Figure 1.1: Cross-sectional transmission electron microscope (TEM) images of an epitaxial Fe(001)/MgO(001)(1.8 nm)/Fe(001) MTJ. (Reprinted from [10, 11].) (b) is a magnified view into panel (a). The vertical and horizontal directions, respectively, correspond to the MgO[001] (Fe[001]) axis and MgO[100] (Fe[110]) axis.

or Slonczewski [14], these *ab initio* methods allow the evaluation of ballistic transport characteristics in full consideration of the detailed electronic and magnetic structures of the electrodes as well as the specific scattering properties of the tunnel barriers.

Three years before the measurement of large roomtemperature TMR ratios in Fe/MgO/Fe MTJs, two theoretical groups predicted these, independently of each other, by means of first-principles calculations [15, 16]. After the first successful experiments [11, 12] it turned out that the calculated magnetoresistance ratios have been at least one order of magnitude too large. The disparity can be attributed to structural differences between idealized (in theory) and real (in experiment) samples.

Theories which include imperfections at the interfaces, such as disorder [17, 18] or roughness effects [19], were able to close the gap between experiment and theory and highlight the importance of perfect interfaces. In particular it was shown that the incorporation of partially oxidized Fe interface layers, which were found by means of x-ray diffraction analyses [20–22], result in considerable reductions of the calculated TMR ratios [23, 24]. Since the approaches used in these calculations lack either current conservation or coherency [25], one of my PhD projects was to develop a suited method which overcomes these problems. As will be reported on pages 51ff, the supercell approach allows a detailed analysis of the electronic transport for MTJs with substoichiometric FeO_c layers, for various oxygen concentrations c. The implementation in an advanced computer code is based on the Landauer-Büttiker approach for ballistic transport, as formulated within multiple-scattering theory.

Beside the reduction of the TMR ratios by means of substitionally disordered interface structures, it was observed that the embedding of both nonmagnetic [26] or magnetic [27] interlayers can be used to enhance the magnetoresistance ratios in Fe/MgO/Fe MTJs. Motivated by these findings I performed first-principles calculations to study the effects of layer-wise antiferromagnetic (LAFM) Mn, LAFM Cr and magnetic Co interlayers on the spin-dependent electronic transport. Besides their importance with respect to technological implications, these investigations also corroborate the importance of interfaces for an accurate description of spin-dependent transport. The corresponding results and discussions can be found on pages 57ff and 62ff.

The theoretical investigations reported in this thesis corroborate that for an accurate description of ballistic transport in MTJs it is essential to treat even details — for example magnetic moments and atomic positions at interfaces, correctly. Only if these ingredients are accounted for reliably (that is from first principles), experiments can be understood in detail. On the other hand, *ab initio* calculations provide a means to design MTJs with given properties, as in computational materials science.

Chapter 2

Theoretical Background

All results which are presented in this work have been achieved in the framework of multiple-scattering theory [28–32] by means of *ab-initio* calculations. The corresponding theoretical background which is necessary to perform and analyze the computed results will be briefly outlined in this chapter. Regarding the electronic structure as well as the electronic transport the discussion can be largely separated into two conceptual blocks.

The first block dealing with the electronic structure ground state properties comprises a summary of the basics of density functional theory (DFT) and the elements of the layer-Korringa-Kohn-Rostoker (LKKR) method.

Within the second block the ballistic and coherent transport by means of Landauer-Büttiker theory [33, 34] is considered. In detail, its implementation within the LKKR formalism and its extension to the treatment of disordered interface layers are discussed.

2.1 Density functional theory (DFT)

Consider the Schrödinger equation [35] of a many-electron ensemble present in a piece of solid or within a large molecule. The corresponding Hamiltonian of the separated electron problem in the Born-Oppenheimer [36] approximation has the form

$$\hat{\boldsymbol{H}}|\Psi\rangle = \left(\hat{\boldsymbol{T}} + \hat{\boldsymbol{U}} + \hat{\boldsymbol{V}}_{\text{ext}}\right)|\Psi\rangle = \hat{\boldsymbol{F}}|\Psi\rangle + \hat{\boldsymbol{V}}_{\text{ext}}|\Psi\rangle \tag{2.1}$$

and describes by means of the kinetic operator $\hat{\boldsymbol{T}}$, and the mutual Coulomb repulsion $\hat{\boldsymbol{U}}$, the motion of N electrons in an external potential $\hat{\boldsymbol{V}}_{\text{ext}}$. While the latter is specific for any studied system, the operator $\hat{\boldsymbol{F}}$ is universal.

Since electrons are fermions the many-electron wave function $|\Psi\rangle$ is totally anti-symmetric with respect to an exchange of two of the N spatial electron coordinate vectors $\boldsymbol{r}_1, \ldots, \boldsymbol{r}_N$. Due to the large number of particles in a solid ($N \gtrsim 10^{23}$) or within huge molecules the interaction of electrons with respect to each other cannot be exactly treated. Consequently, approximations which reduce the complexity of the problem are needed.

One of the most successful approaches is density functional theory [37]. The key idea of the theory is the mapping of the many-particle problem onto an effective, non-interacting single-particle problem. Instead of looking for the many-electron wave function $|\Psi\rangle$ which depends on $3N$ spatial coordinates, one asks for a spatially dependent electron density distribution $n(\boldsymbol{r})$. In particular, a variational principle with respect to electron density functionals is used to determine ground state properties of many-electron ensembles. This treatment became feasible after the formulation and proof of two basic theorems which were firstly discussed by Hohenberg and Kohn [38].

The Hohenberg-Kohn theorems

Hohenberg-Kohn 1 *The ground state electron density* $n_0(\boldsymbol{r})$ *of a many-electron system in the presence of an external potential* $\hat{\boldsymbol{V}}_{\text{ext}}$ *uniquely determines that external potential.*

This statement implies that each ground-state wave function in (2.1) is a unique functional of the ground-state electron density, $|\Psi_0\rangle = |\Psi[n_0]\rangle$. Consequently, each ground-state expectation value of an observable $\hat{\boldsymbol{o}}$ is also a functional of n_0,

$$\boldsymbol{o}[n_0] = \langle\Psi[n_0]|\hat{\boldsymbol{o}}|\Psi[n_0]\rangle. \tag{2.2}$$

This is in particular valid for $\hat{\boldsymbol{H}}$ and its particular contributions $\hat{\boldsymbol{T}}, \hat{\boldsymbol{U}}$, and $\hat{\boldsymbol{V}}_{\text{ext}}$ in (2.1).

Under the condition that the ground-state energy is non-degenerate, the total energy can be calculated as $E_0 = E[n_0] = \langle\Psi_0|\hat{\boldsymbol{H}}|\Psi_0\rangle$ and the second theorem holds.

Hohenberg-Kohn 2 *The functional for the ground-state energy* E_0 *is minimized by the ground-state electron density* n_0.

This theorem allows to determine the ground state properties, such as geometric and magnetic structure, by minimizing the total energy.

The Kohn-Sham equations

A concrete computational scheme of these generally valid theorems was provided by Kohn and Sham shortly after their formulation [39]. The intention of their proposed approach was to develop a concept similar to the self-consistent Hartree scheme. It turned out that the new method, which transforms the many-electron Schrödinger equation (2.1) into N effective single-particle equations, was in its formulation as exact as the Hartree approximation, but in its physical significance went far beyond the latter without enhancing the difficulty of calculations. A short conceptual overview of this approach is presented in the following.

According to (2.2) one has to operate with functional expressions of $F[n] = \langle\Psi[n]|\hat{\boldsymbol{F}}|\Psi[n]\rangle$ and $V_{\text{ext}}[n] = \langle\Psi[n]|\hat{\boldsymbol{V}}_{\text{ext}}|\Psi[n]\rangle$. A functional representation for the system-dependent external potential reads

$$\mathrm{V}_{\text{ext}}[n] = \int n(\boldsymbol{r})V_{\text{ext}}(\boldsymbol{r})d^3\boldsymbol{r}. \tag{2.3}$$

Following [39] the universal functional can be rewritten as $F[n] = T_s[n] + U_H[n] + E_{xc}[n]$. Its individual contributions represent the kinetic energy $T_s[n]$ of a non-interacting electron gas of density $n(\boldsymbol{r})$, the classical Coulomb interaction term $U_H[n]$ as it is known from the Hartree approximation,

$$U_H[n] = \frac{1}{2}\int d\boldsymbol{r}\, n(\boldsymbol{r}) \int d\boldsymbol{r}' \frac{n(\boldsymbol{r}')}{|\boldsymbol{r}-\boldsymbol{r}'|}, \tag{2.4}$$

and the remainder $E_{xc}[n]$. The latter functional is usually referred to as the exchange and correlation energy, since it is presumed that it comprises all remaining many-electron interactions.

By choosing the functionals in such a manner, the Schrödinger equation (2.1) becomes separable into N single-particle equations. Through the introduction of an orthonormal single-particle basis $\{|\phi_i\rangle\}$ the electron density can be defined by means of the first N occupied states,

$$n(\boldsymbol{r}) = \sum_i^N |\langle\boldsymbol{r}|\phi_i\rangle|^2. \tag{2.5}$$

The energy variation ${}^{\delta E[n]}/_{\delta n}$ according to the second Hohenberg-Kohn theorem leads, together with the incorporation of the particle number conservation by means of a Lagrange multiplier μ, to a set of N Schrödinger-type equations,

$$\{\hat{\boldsymbol{T}}_s + \mathrm{V}_{\text{eff}}(\boldsymbol{r})\}\,|\phi_i\rangle = \varepsilon_i|\phi_i\rangle. \tag{2.6}$$

These equations are called the Kohn-Sham equations (KSEs) and describe the motion of non-interacting particles within an effective potential $\mathrm{V}_{\text{eff}}(\boldsymbol{r}) = \mathrm{V}_{\text{ext}}(\boldsymbol{r}) + U_H(\boldsymbol{r}) + \mathrm{V}_{\text{xc}}(\boldsymbol{r})$ with the unknown exchange-correlation potential $\mathrm{V}_{\text{xc}}(\boldsymbol{r}) = {}^{\delta E_{xc}}/_{\delta n}$.

Since $\mathrm{V}_{\text{eff}}(\boldsymbol{r})$ depends on $n(\boldsymbol{r})$, and vice versa, the KSEs have to be solved self-consistently. Usually one starts with an appropriate guess for $n(\boldsymbol{r})$, then calculates the corresponding $\mathrm{V}_{\text{eff}}(\boldsymbol{r})$ and solves the Kohn-Sham equations for all $|\phi_i\rangle$. From the latter one computes a new density and starts again. This cycle is repeated until convergence is reached.

Generalization to magnetic systems

Up to now all considerations have been done with respect to non-magnetic materials and with no external magnetic field present. In order to study the motion of electrons in magnetic solids in particular the 3d ferromagnets Ni, Co, and Fe, the above described DFT has to be extended to a spin-density-functional theory [40, 41]. This generalization requires, besides the knowledge of $n(\boldsymbol{r})$, the determination of another ground-state variable, namely the magnetization density $\boldsymbol{m}(\boldsymbol{r})$.

Assuming that the external magnetic potential only couples to the spin degrees of freedom [42, 43], one has to regard in a non-relativistic theory a set of KSEs for two-component spinors $\phi_i = (\phi_i^{\uparrow}, \phi_i^{\downarrow})$, which have the form of Pauli equations [44].

This treatment leads to an additional contribution of the external potential (2.3),

$$\mathrm{V}_{\mathrm{ext}}[n, \boldsymbol{m}] = \int \left[n(\boldsymbol{r}) V_{\mathrm{ext}}(\boldsymbol{r}) - \boldsymbol{B}(\boldsymbol{r}) \boldsymbol{m}(\boldsymbol{r}) \right] d\boldsymbol{r} \tag{2.7}$$

which is a functional of $n(\boldsymbol{r})$ and $\boldsymbol{m}(\boldsymbol{r})$. The second term describes the coupling of a magnetic field to the electron spins,

$$-\sum_i \langle \phi_i | \mu_0 \boldsymbol{B} \hat{\boldsymbol{\sigma}} | \phi_i \rangle = -\sum_n \sum_i B_n \mu_0 \langle \phi_i | \hat{\sigma}_n | \phi_i \rangle = -\sum_n B_n m_n, \tag{2.8}$$

where the m_n with n ={x,y,z} represent the expectation values of the spin-operators. These are the 2 × 2 Pauli matrices $\sigma_x = \hbar/2 \left(\begin{smallmatrix} 0 & 1 \\ 1 & 0 \end{smallmatrix}\right)$, $\sigma_y = \hbar/2 \left(\begin{smallmatrix} 0 & -\mathrm{i} \\ \mathrm{i} & 0 \end{smallmatrix}\right)$ and $\sigma_z = \hbar/2 \left(\begin{smallmatrix} 1 & 0 \\ 0 & -1 \end{smallmatrix}\right)$.

It can be shown that the theorems of Hohenberg and Kohn are valid in a generalized manner [45]. The ground-state is then a functional of n and $\boldsymbol{m}$, and the total energy $E_0 = E[n_0, \boldsymbol{m}_0]$ is minimized by the ground-state densities.

Typically it is assumed that the magnetic field $\boldsymbol{B}(\boldsymbol{r})$ points only along one direction. By choosing B_z as non-vanishing component, only the z-projections of the spin-dependent densities $n = n^{\uparrow} + n^{\downarrow}$ and $m = n^{\uparrow} - n^{\downarrow}$ have to be regarded. Hence, for each spin projection one set of KSEs has to be solved self-consistently:

$$\left\{ \hat{\boldsymbol{T}}_s + \mathrm{V}_{\mathrm{eff}}^{\tau}(\boldsymbol{r}) \right\} |\phi_i^{\tau}\rangle = \varepsilon_i^{\tau} |\phi_i^{\tau}\rangle, \qquad \tau = \uparrow, \downarrow \text{ or } +1, -1. \tag{2.9}$$

Usually a spin-averaged exchange-correlation potential $\mathrm{V}_{\mathrm{xc}}[n^{\uparrow}, n^{\downarrow}] = \delta E_{xc}[n,m]/\delta n$ and a magnetic exchange potential $\mathrm{B}_{\mathrm{xc}}[n^{\uparrow}, n^{\downarrow}] = \delta E_{xc}[n,m]/\delta m$ are introduced. Both are used to define and to compute iteratively the spin-dependent, effective, single-particle potentials: $\mathrm{V}_{\mathrm{eff}}^{\tau}(\boldsymbol{r}) = \mathrm{V}_{\mathrm{ext}}[n] + U_H[n] + \mathrm{V}_{\mathrm{xc}}[n, m] + \tau \left\{ B_z(\boldsymbol{r}) + \mathrm{B}_{\mathrm{xc}}[n, m] \right\}$.

Due to the assumption of coupling exclusively between the external magnetic field and the electron spins (2.8), orbital magnetism is not included within the spin-density-functional theory.

This can be described within the current-density-functional theory (CDFT) [46].

Local approximations to the exchange-correlation functional

The above formulations of the Kohn-Sham equations are exact. But due to the lack of knowledge regarding the universal exchange-correlation functionals one has to rely on approximations. One of the most widely used approaches is the local-density approximation (LDA) [47] which assumes slowly varying densities. Hence, the exchange-correlation energy $\varepsilon_{xc}^{\text{hom}}$ of a non-interacting, homogeneous electron gas with a density n is used,

$$E_{xc}[n] = \int \varepsilon_{xc}^{\text{hom}}(n) n(\boldsymbol{r}) d\boldsymbol{r}. \tag{2.10}$$

While the exchange contribution of a homogeneous electron gas is analytically calculated, the correlation part has to be computed numerically and parametrized [40,48,49].

The local-spin-density approximation (LSDA) is a straightforward generalization of the LDA to treat spin-polarized and magnetic systems,

$$E_{xc}[n^{\uparrow}, n^{\downarrow}] = \int \varepsilon_{xc}^{\text{hom}}(n^{\uparrow}, n^{\downarrow}) n(\boldsymbol{r}) d\boldsymbol{r}. \tag{2.11}$$

Approaches that go beyond L(S)DA are, for instance, the generalized gradient approximation (GGA), which is still local but also takes into account the gradient of the density [50],

$$E_{xc}[n^{\uparrow}, n^{\downarrow}] = \int d\boldsymbol{r}\, \varepsilon_{xc}^{\text{hom}}(n^{\uparrow}, n^{\downarrow}, \nabla n^{\uparrow}, \nabla n^{\downarrow}) n(\boldsymbol{r}). \tag{2.12}$$

The self-interaction correction (SIC) [51,52] is applied for strongly correlated systems.

2.2 Electronic transport

2.2.1 Conductance viewed as transmission

In the following, a formalism based on Landauer's theory for the electronic transport in nanoscale devices will be briefly discussed. The main focus will be put on systems that exhibit lateral confinements which are caused by macroscopic constrictions. Such systems are typically characterized through quasi one-dimensional transport directions with laterally quantized traveling electronic states.

The main principle of the Landauer approach is the assumption that the system in question is

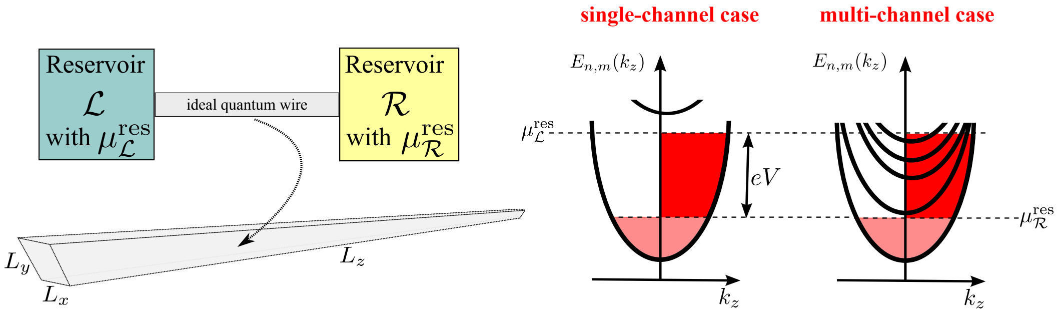

Figure 2.1: Schematics of a quasi one-dimensional quantum wire described by a rectangular waveguide. The latter connects two reservoirs with well-defined distinct electrochemical potentials $\mu_{\mathscr{L}}^{\text{res}}$ and $\mu_{\mathscr{L}}^{\text{res}}$. It is assumed that due to a lateral constriction of the wire ($L_x, L_y \ll L_z$) quantized sub-bands $E = E_{n,m} + k_z^2/(2m^*)$ are present. Currents in the wire are driven by those sub-bands (channels) which lie in the bias voltage window eV. Depending on the number of contributing sub-bands one distinguishes between the single- and multi-channel case.

coupled to large reservoirs where all inelastic processes take place. It is further presumed that the characteristic length scale, L_z, in the transport direction is always much smaller than the elastic mean free path ℓ_{e^-} and the phase coherence length ℓ_ψ of the respective electronic states. Hence, the electronic transport can always be regarded in the ballistic regime ($L_z \ll \ell_{e^-}$), and in the phase-coherent limit ($L_z \ll \ell_\psi$).

Consequently, the coherent transport in the Landauer framework can be formulated as a quantum mechanical scattering problem where the associated conductance can be expressed in terms of transmission probabilities [34].

In particular it is assumed that the ballistic and coherent transport proceeds within ideal quantum wires, which behave as waveguides for the traveling electronic states and connect the system's scattering obstacle with the reservoirs. Thus, before the explanation of Landauer's theory, which expresses the conductance in terms of the scattering properties, the pure electronic transport within a perfect one-dimensional quantum channel will be preliminary discussed.

2.2.1.1 Conductance of a one-dimensional channel

I consider (Fig. 2.1) a quantum wire which connects two reservoirs with electrochemical potentials $\mu_{\mathscr{L}}^{\text{res}}$ and $\mu_{\mathscr{R}}^{\text{res}}$. Due to lateral confinement perpendicular to the z-direction the wire exhibits a quasi one-dimensional geometry. Assuming, without loss of generality, that $\mu_{\mathscr{L}}^{\text{res}} > \mu_{\mathscr{R}}^{\text{res}}$, an electron current will flow from reservoir $\mathscr{L}$ towards $\mathscr{R}$.

With L_x and L_y on the nanoscale, but an extended elongation L_z in the z direction, the energies and eigenstates of such a wire would be given by [53, 54]

$$E = E_{n,m} + E(k_z) = \frac{\hbar^2\pi^2}{2m^*}\left(\frac{n^2}{L_x^2} + \frac{m^2}{L_y^2}\right) + \frac{\hbar^2 k_z^2}{2m^*}, \qquad n, m \in \mathbb{N}, \tag{2.13a}$$

$$\Psi(x, y, z) = \Psi_{n,m}(x, y) \exp(\mathrm{i}k_z z)/L_z. \tag{2.13b}$$

Where n and m are quantum numbers marking eigenstates within the x-y plane, and the wave numbers k_z define the propagation direction along the z direction.

The representations (2.13) form a continuum of laterally quantized one-dimensional states. Corresponding dispersion relations start at specific energies $E_{n,m}$ and are called sub-bands, modes, or channels, depending on the context.

Presuming reflectionless wire-reservoir interfaces it is further postulated that incident electrons will be, independent of their energy or quantum phase, completely absorbed and thermalized by the reservoirs. The latter ensures also a continuous outgoing flow of electrons with energies below the chemical potentials $\mu_{\mathscr{L}}^{\mathrm{res}}$ and $\mu_{\mathscr{R}}^{\mathrm{res}}$.

A net current which is carried by electronic states with energies below $\mu_{\mathscr{R}}^{\mathrm{res}}$ is zero. As indicated in Fig. 2.1, this fact can be explained with the balance of left ($k_z < 0$) and right ($k_z > 0$) traveling occupied states where the corresponding currents are compensating each other. Consequently, only electrons whose energies lie between $\mu_{\mathscr{L}}^{\mathrm{res}}$ and $\mu_{\mathscr{R}}^{\mathrm{res}}$ contribute to the total current I.

The current $dI_{n,m}$, which is characterized by a sub-band (n, m), is defined through the number of contributing electrons $dN_{n,m}$ with an energy E between $E'_{n,m}(k_z)$ and $E'_{n,m}(k_z) + dE$, the corresponding group velocity $v_{n,m}^{g}(E)$ and the charge e,

$$dI_{n,m} = e\, v_{n,m}^{g}(E)\, dN_{n,m}. \tag{2.14}$$

With the help of the definition of the one-dimensional density of states ${}^{dN}\!/_{dE} = {}^{1}\!/_{\pi\hbar v^g}$ the group velocity cancels out,

$$dI_{n,m} = \frac{2e}{h} dE. \tag{2.15}$$

Please note that the expression for the current is independent of the density of states or the group velocity. Consequently, each sub-band or channel provides the same current. The total current thus reads

$$I_{n,m} = \frac{2e}{h} \int_{\mu_{\mathscr{R}}^{\mathrm{res}}}^{\mu_{\mathscr{L}}^{\mathrm{res}}} dE = \frac{2e}{h}(\mu_{\mathscr{L}}^{\mathrm{res}} - \mu_{\mathscr{R}}^{\mathrm{res}}). \tag{2.16}$$

The potential difference between both reservoirs is given by $eV = \mu_{\mathscr{L}}^{\mathrm{res}} - \mu_{\mathscr{R}}^{\mathrm{res}}$.

In the following it is assumed that total currents are calculated within the regime of linear response. For this purpose one presumes that there is a linear relationship between infinitely small currents and infinitely small applied voltages ($V \to 0$). Under these conditions one can define according to Ohm's law the conductance via

$$\Gamma = R^{-1} = \frac{I}{V}. \tag{2.17}$$

Consequently, the conductance contribution of a single sub-band or single-channel (see Fig. 2.1) is given by

$$\Gamma_0 = \frac{2e^2}{h} \approx (12.9\mathrm{k}\Omega)^{-1}. \tag{2.18}$$

The conductance quantum Γ_0 is associated with non-magnetic systems which exhibit spin-degeneracy. In magnetic systems where the spin-degeneracy is lifted one has to consider each spin channel $\tau = \uparrow, \downarrow$ separately and thus obtains $\Gamma_0^\tau = e^2/h \approx (25.8\mathrm{k}\Omega)^{-1}$.

With $M(M^\tau)$ being the number of channels at the Fermi energy, the conductance in the multi-channel case (see Fig. 2.1) is given by the expression $\Gamma = M\Gamma_0$ ($\Gamma^\tau = M^\tau \Gamma_0^\tau$).

It may look surprising that an ideal quantum wire without any present scatterers shows a finite resistance. But Imry [55] pointed out that the non-vanishing resistance arises at the interfaces between reservoirs and wire. This contact resistance is unavoidable in two-terminal configurations. A four-terminal measurement, where the potential drop is comprised within the wire itself instead of the reservoirs exhibits zero resistance [56]. A direct observation of this quantized contact resistance was first measured for semi-conductor point contacts in GaAs heterostructures [57].

2.2.1.2 The Landauer formula and Büttiker's generalization

As illustrated in Fig. 2.2, a nanoscale conductor modeled in the Landauer picture [34, 54, 58] is regarded as two reservoirs connected via ideal quantum wires, with a constriction $\mathscr{S}$ between them. $\mathscr{S}$ is regarded as a multi-channel scatterer, meaning that a unit current in channel i is reflected into channel j with probability R_{ij} ($i, j \in \mathscr{L}$) and transmitted into j with probability T_{ij} ($i \in \mathscr{L}, j \in \mathscr{R}$). Due to current conservation it holds that $\sum_j^{N_\mathscr{R}} T_{ij} + \sum_j^{N_\mathscr{L}} R_{ij} = 1$. With respect to the number of contributing channels within the left-hand side (lhs) and the right-hand side (rhs), wire indices run from 1 to $N_\mathscr{L}$ and $N_\mathscr{R}$, respectively. A current comprising all transmitted channels i into channel j on the rhs is given according to (2.16) by

$$I_j = \Gamma_0 \left[\sum_i^{N_\mathscr{L}} T_{ij} \right] (\mu_\mathscr{L}^{\mathrm{res}} - \mu_\mathscr{R}^{\mathrm{res}}) = \Gamma_0 \left[1 - \sum_i^{N_\mathscr{L}} R_{ij} \right] (\mu_\mathscr{L}^{\mathrm{res}} - \mu_\mathscr{R}^{\mathrm{res}}). \tag{2.19}$$

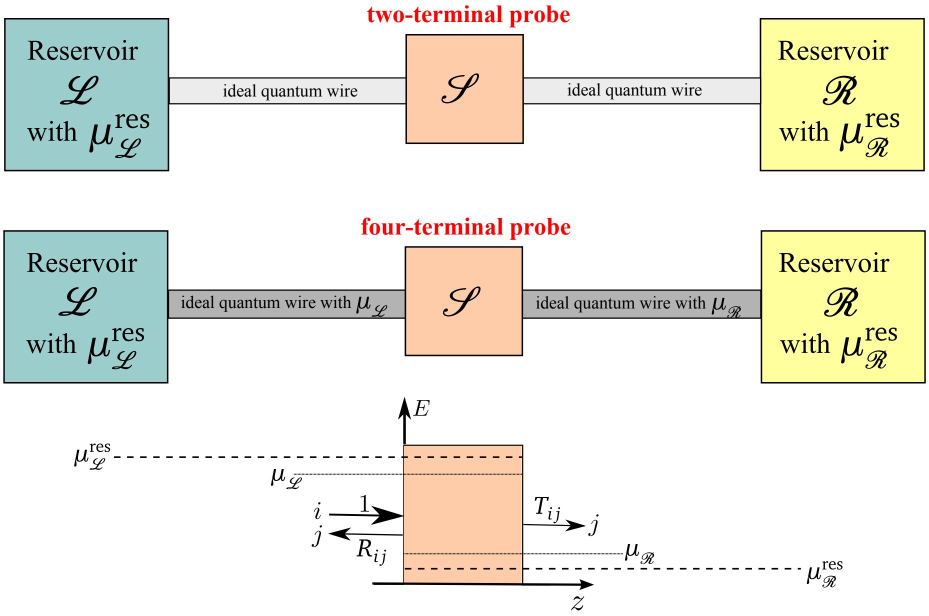
two-terminal probe
Reservoir $\mathscr{L}$ with $\mu_{\mathscr{L}}^{\text{res}}$
ideal quantum wire
$\mathscr{S}$
ideal quantum wire
Reservoir $\mathscr{R}$ with $\mu_{\mathscr{R}}^{\text{res}}$
four-terminal probe
Reservoir $\mathscr{L}$ with $\mu_{\mathscr{L}}^{\text{res}}$
ideal quantum wire with $\mu_{\mathscr{L}}$
$\mathscr{S}$
ideal quantum wire with $\mu_{\mathscr{R}}$
Reservoir $\mathscr{R}$ with $\mu_{\mathscr{R}}^{\text{res}}$
E
$\mu_{\mathscr{L}}^{\text{res}}$
$\mu_{\mathscr{L}}$
i
1
j
R_{ij}
T_{ij}
j
$\mu_{\mathscr{R}}$
$\mu_{\mathscr{R}}^{\text{res}}$
z

Figure 2.2: Conceptual scheme of a conducting nanosystem within the Landauer picture. A scatterer $\mathscr{S}$ is connected via ideal quantum wires with two reservoirs. These are characterized through different electrochemical potentials $\mu_{\mathscr{L}}^{\text{res}}$ and $\mu_{\mathscr{R}}^{\text{res}}$, respectively, in which $\mu_{\mathscr{L}}^{\text{res}} > \mu_{\mathscr{R}}^{\text{res}}$. Depending on the region of the voltage drop in the system (between reservoirs with $V = \mu_{\mathscr{L}}^{\text{res}} - \mu_{\mathscr{R}}^{\text{res}}$ or between ideal wires with $V = \mu_{\mathscr{L}} - \mu_{\mathscr{R}}$) one distinguishes principally between two-terminal and four-terminal arrangements. $\mathscr{S}$ is regarded as a multi-channel scatterer for incident lateral quantized electronic states.

The latter relation represents the current conservation. With the help of the short hand notations

$$\sum_{i}^{N_{\mathscr{L}}} T_{ij} = T_j \quad (\text{with}\, j \in \mathscr{R}) \qquad \text{and} \qquad \sum_{i}^{N_{\mathscr{L}}} R_{ij} = R_j \quad (\text{with}\, j \in \mathscr{L}) \tag{2.20}$$

one can find an expression for the total current in the form

$$I_{\text{tot}} = \sum_j I_j = \Gamma_0(\mu_{\mathscr{L}}^{\text{res}} - \mu_{\mathscr{R}}^{\text{res}}) \sum_j^{N_{\mathscr{R}}} T_j = \Gamma_0(\mu_{\mathscr{L}}^{\text{res}} - \mu_{\mathscr{R}}^{\text{res}}) \sum_j^{N_{\mathscr{L}}} \big(1 - R_j\big)\,. \tag{2.21}$$

Analogously to (2.17) the conductance is calculated as $\Gamma = I_{\text{tot}}/V$.

Depending on where the voltage drop occurs, there are two main conceptual pictures of a Landauer conductor discussed in the literature (see Fig. 2.2), that of a two-terminal, and that of a four-terminal probe, respectively. Both are considered due to their experimental realization regarding a simultaneous measurement of currents and applied voltages within conductors on the nanoscale.

In a two-terminal measurement the voltage and current are tapped at the same leads. This causes an additional contact resistance that influences the voltage measuring itself. The voltage drop is therefore associated with the difference of the electrochemical potentials in the reservoirs $V = \mu^{\text{res}}_{\mathscr{L}} - \mu^{\text{res}}_{\mathscr{R}}$ and one achieves for the two-terminal conductance

$$\Gamma_{2-\text{term}} = \frac{1}{e}\frac{I_{\text{tot}}}{\mu^{\text{res}}_{\mathscr{L}} - \mu^{\text{res}}_{\mathscr{R}}} = \Gamma_0 \sum_j^{N_{\mathscr{R}}} T_j = \Gamma_0 \sum_j^{N_{\mathscr{R}}} \sum_i^{N_{\mathscr{L}}} T_{ij}. \tag{2.22}$$

This representation, where the conductance is calculated in terms of transmission probabilities, is referred to as the Landauer formula in the literature. The corresponding two-terminal resistance

$$\Gamma^{-1}_{2-\text{term}} = \frac{1}{\Gamma_0}\left(1 + \frac{1 - \sum_j^{N_{\mathscr{R}}} T_j}{\sum_j^{N_{\mathscr{R}}} T_j}\right) = \frac{1}{\Gamma_0} + \frac{1}{\Gamma_0}\frac{\sum_j^{N_{\mathscr{L}}} R_j}{\sum_j^{N_{\mathscr{R}}} T_j} \tag{2.23}$$

comprises contributions that stem from scattering and a part that represents the quantized contact resistance. As discussed above, this contact resistance is the reason for the presence of a non-vanishing, finite resistance in a perfectly conducting quantum wire with $T_j = 1$ for all present channels j [59].

In a four-terminal probe this contact resistance is avoided through a separation into pairs of current-carrying and voltage-sensing electrodes which allow a non-invasive, simultaneous measuring of current and voltages. To incorporate this setup one introduces an additional voltage drop within the ideal wires, which must be smaller than that for the two-terminal device $eV = \mu_{\mathscr{L}} - \mu_{\mathscr{R}} < \mu^{\text{res}}_{\mathscr{L}} - \mu^{\text{res}}_{\mathscr{R}}$. In order to determine $\mu_{\mathscr{L}}$ and $\mu_{\mathscr{R}}$ one assumes that transmitted and reflected currents around $\mathscr{S}$ cause a reduction in carrier density on the lhs and a pile-up of charge on the rhs [33, 54]. This charge rearrangement can be approximated by an average density in both ideal leads which can be characterized by different chemical potentials $\mu_{\mathscr{L}}$ and $\mu_{\mathscr{R}}$ as shown in Fig. 2.2. By comparing the densities on both sides of the barrier one finds expressions for $\mu_{\mathscr{L}}$ and $\mu_{\mathscr{R}}$. The four-terminal conductance in the multi-channel case is then computed as

$$\Gamma_{4-\text{term}} = \Gamma_0 \frac{2\sum_j^{N_{\mathscr{R}}} T_j}{1 + \frac{1}{g_{\mathscr{L}}}\sum_j^{N_{\mathscr{L}}} R_j v^{-1}_{\mathscr{L},j} - \frac{1}{g_{\mathscr{R}}}\sum_j^{N_{\mathscr{R}}} T_j v^{-1}_{\mathscr{R},j}}, \tag{2.24a}$$

where $v_{\mathscr{L},j}$ and $v_{\mathscr{R},j}$ are the group velocities on the lhs and rhs respectively, and

$$g_{\mathscr{L}} = \sum_j^{N_{\mathscr{L}}} v^{-1}_{\mathscr{L},j} \quad \text{and} \quad g_{\mathscr{R}} = \sum_j^{N_{\mathscr{R}}} v^{-1}_{\mathscr{R},j}. \tag{2.24b}$$

The approach which ends up with formula (2.24) is often referred to as the Landauer-Büttiker theory [33].

An identical expression of the four-terminal conductance (2.24a) can be derived within the Kubo-formalism [60]. A detailed discussion regarding the equivalence of both approaches can be found in [61].

In the work [62] it is shown that the Landauer approach is valid in a more general context. For example, there is no need to assume that: *(i)* a current on the nanoscale flows only if there is a density mismatch between carrier reservoirs, held at different chemical potentials; *(ii)* coherent elastic scattering is the exclusive transmission mechanism mediating the conductance; *(iii)* inelastic scattering in an open conductor is a remote effect deep in the reservoirs, of no physical consequence for transport; and *(iv)* the quantized conductance requires linear response in a degenerate channel.

In the limit of very small transmission probabilities ($T_i \ll 1$) the two- and four-terminal conductances become equivalent. This limiting case is typically present for tunneling phenomena. As will be discussed later (see 2.2.4), laterally quantized Bloch states in planar tunnel junctions are mainly of interest. The corresponding channels are hereby identified and characterized by the two-dimensional in-plane wave vector $\boldsymbol{k}_{\parallel}$, and the wave vector pointing in the transport direction $k_z\boldsymbol{e}_z$. In the framework of linear response, current and conductance at the Fermi level E_F are given for an infinitely small bias voltage by [63]

$$\Gamma(E_F) = \lim_{V\to 0}\frac{I}{V} = \Gamma_0 \int\limits_{\text{2BZ}} T(E_F, \boldsymbol{k}_{\parallel})d\boldsymbol{k}_{\parallel} = \Gamma_0 \int\limits_{\text{2BZ}} \Big[\sum_{k_z k_z'} T_{k_z k_z'}(E_F, \boldsymbol{k}_{\parallel})\Big] d\boldsymbol{k}_{\parallel}, \tag{2.25}$$

The integration has to be performed over the two-dimensional Brillouin zone (2BZ). The wave numbers k_z and k_z' play the role of band indices which characterize conducting channels (cf. i and j in the previous considerations).

In order to calculate current-voltage characteristics for finite bias voltages one calculates the conductances at the bias shifted energies $E' = E_F - V'$, as formulated in the linear response regime (2.25) and integrated over the bias-energy window $(E_F, E_F - V)$

$$\Gamma(V) = \frac{\Gamma_0}{V}\int\limits_{E_F - V}^{E_F} dE' \int\limits_{\text{2BZ}} T(E', \boldsymbol{k}_{\parallel})d\boldsymbol{k}_{\parallel} = \frac{1}{V}\int\limits_{E_F - V}^{E_F} \Gamma(E')dE'. \tag{2.26}$$

The associated current can then be expressed as $I(V) = \Gamma(V)V$.

In magnetic systems spin-dependent conductances $G^{\tau\tau'}$ or currents $I^{\tau\tau'}$ are present with spin indices $\tau, \tau' = (\uparrow, \downarrow)$. The computation of these is identical to those formulated in (2.25) and (2.26) but with the transmission probabilities replaced by those that connect a spin-channel τ with τ'. In magnetic tunnel junctions both spin-dependent quantities define the tunnel magnetoresistance ratio

$$\delta = \frac{\Gamma^{\mathrm{P}} - \Gamma^{\mathrm{AP}}}{\Gamma^{\mathrm{AP}}} = \frac{(\Gamma^{\uparrow\uparrow} + \Gamma^{\downarrow\downarrow}) - (\Gamma^{\uparrow\downarrow} + \Gamma^{\downarrow\uparrow})}{(\Gamma^{\uparrow\downarrow} + \Gamma^{\downarrow\uparrow})} \tag{2.27}$$

with respect to parallel (P) or anti-parallel (AP) magnetizations of the leads.

2.2.2 Multiple-scattering theory

2.2.2.1 The Green's function method

Approved methods to solve the Kohn-Sham equations $(\hat{\boldsymbol{H}}_{KS} - \varepsilon_i)|\phi_i\rangle = 0$ (2.6) or (2.9) are schemes like e.g. the **linear combination of atomic orbitals** (LCAO), the **augmented plane wave** (APW) method or the **linear muffin-tin orbital** (LMTO) method. These procedures differ with respect to their choice of the single-particle basis $\{|\phi_i\rangle\}$.

Another established approach which does not primarily calculate wave-functions is the **Green's function** (GF) method [31,32,64]. With the help of the resolvent of $\hat{\boldsymbol{H}}_{KS}$,

$$\hat{\boldsymbol{G}}(z) = (z - \hat{\boldsymbol{H}}_{KS})^{-1}, \qquad (z - \hat{\boldsymbol{H}}_{KS})\hat{\boldsymbol{G}}(z) = 1, \qquad z \in \mathbb{C}, \tag{2.28}$$

one derives an equivalent formulation of the Kohn-Sham equations. The Green's operator $\hat{\boldsymbol{G}}$ and $\hat{\boldsymbol{H}}_{KS}$ have the same set of eigenfunctions $\{|\phi_i\rangle\}$.

Side-limits of $\hat{\boldsymbol{G}}$ have to be regarded since the Kohn-Sham energies ε_i are real. Hence, in coordinate representation an expression for the advanced and retarded GFs reads

$$G^{\pm}(\boldsymbol{r}, \boldsymbol{r}'; \varepsilon) = \lim_{\eta \to \pm 0} \langle \boldsymbol{r} | (z - \hat{\boldsymbol{H}}_{KS})^{-1} | \boldsymbol{r}' \rangle \qquad \text{with} \quad z = \varepsilon \pm \mathrm{i}\eta. \tag{2.29}$$

The Green's function provides all necessary information in order to calculate the electronic properties of a solid system. The determination of the former is the central task within the **Korringa-Kohn-Rostoker** (KKR) method [65, 66]. In the following an overview of the basic concepts is shortly presented.

An important ability of the Green's function with respect to a self-consistent treatment is the calculation of the charge density by means of its imaginary part,

$$n(\boldsymbol{r}) = \mp \frac{1}{\pi} \int_{-\infty}^{E_F} d\varepsilon \left[\mathrm{Im} G^{\pm}(\boldsymbol{r}, \boldsymbol{r}; \varepsilon) \right]. \tag{2.30}$$

A self-consistent scheme based on the GF technique has to run iteratively between the computation of n and G until the self-consistency of the regarded effective potentials is reached.

Usually it is assumed that these effective potentials can be decomposed as [32]:

$$\mathrm{V}_{\mathrm{eff}}(\boldsymbol{r}) = \sum_i \mathrm{V}^i_{\mathrm{eff}}(\boldsymbol{r}_i), \qquad \boldsymbol{r}_i = \boldsymbol{r} - \boldsymbol{R}_i, \tag{2.31}$$

where the $\mathrm{V}^i_{\mathrm{eff}}(\boldsymbol{r}_i)$ are located at positions $\boldsymbol{R}_i$ such that the domains of any arbitrary pair of potentials $\mathrm{V}^i_{\mathrm{eff}}$ and $\mathrm{V}^j_{\mathrm{eff}}$ are disjoint. Within an infinite, translationally invariant crystal, the positions $\boldsymbol{R}_i$ are provided by the real space lattice.

The application of (2.31) is simplified by means of spherically symmetric potentials

$$\mathrm{V}^i_{\text{eff}}(\boldsymbol{r}_i) = \begin{cases} V^i_{\text{eff}}(r_i) & |\boldsymbol{r}_i| = r_i \leq R^i_s, \\ \text{constant} & \text{otherwise.} \end{cases} \tag{2.32}$$

Furthermore, with $\lim_{r_i \to 0} r_i^2 V^i_{\text{eff}}(r_i) = 0, \forall i$ it is presumed that all effective potentials exhibit a regular behavior.

Depending on the size of the sphere radii R^i_s two approximations are distinguished and mainly used in KKR electronic structure calculations. Within the **muffin-tin** (MT) approximation the space is filled with muffin-tin spheres which are separated by an interstitial region with a constant potential. The radius R^i_s is correspondingly referred to as the muffin-tin radius for the ith sphere. In the **atomic-sphere approximation** (ASA) it is assumed that the volume of the regarded solid is filled with overlapping spheres which leave lesser space for an interstitial region. Consequently the ASA radii for the ith sphere are greater than their muffin-tin counterparts. In contrast to interstitial regions of the MT concept, the ASA spheres provide the advantage to maintain spherical symmetry for the computation of the Greens function in (2.30) but induce the problem how to treat the overlap regions.

$\hat{\boldsymbol{G}}$ is usually calculated with respect to a known reference system with GF $\hat{\boldsymbol{G}}_0$. The relation between both is given by the Dyson equation

$$\hat{\boldsymbol{G}} = \hat{\boldsymbol{G}}_0 + \hat{\boldsymbol{G}}_0 \hat{V} \hat{\boldsymbol{G}} = \hat{\boldsymbol{G}}_0 + \hat{\boldsymbol{G}}_0 \hat{T} \hat{\boldsymbol{G}}_0, \tag{2.33}$$

with $\hat{V}$ characterizing the potential difference of both systems. Commonly, constant potentials within the MT or ASA spheres are chosen as reference systems. In the screened-KKR method [67,68] these are for instance repulsive potentials of constant positive height. Consequently, the GFs decay rapidly in real space and allow a numerically efficient treatment by sparse matrices.

The scattering operator $\hat{T} = \hat{V}(1 + \hat{\boldsymbol{G}}_0)\hat{T}$ is introduced such that instead of $\hat{\boldsymbol{G}}$ only the reference system appears on the right side of (2.33). Correspondingly, the reformulated problem requires the computation of $\hat{T}$.

The latter comprehends all scattering properties of present atoms within a regarded solid system. Each atom forms a scattering center on its position and is characterized by an effective potential $\mathrm{V}^i_{\text{eff}}(\boldsymbol{r}_i)$. The argument is defined relative to the center of the nearest atom, i.e., $\boldsymbol{r}_i = \boldsymbol{r} - \boldsymbol{R}_i$ (where $\boldsymbol{R}_i$ is the center of atom i) if $\boldsymbol{r}$ is closest to $\boldsymbol{R}_i$. All scattering properties of such an individual scatterer i are attributed by the single-site scattering operator $\hat{t}^i = \mathrm{V}^i_{\text{eff}}(\boldsymbol{r}_i)(1 + \hat{\boldsymbol{G}}_0)\hat{t}^i$. Possibilities to determine the corresponding matrix elements in an angular momentum representation are outlined in section 2.2.2.2.

Accordingly, $\hat{T}$ is often defined in terms of scattering path operators (SPOs) [69]. These comprise all propagation paths of an electron moving from a scattering center located at $\boldsymbol{R}_i$ via all other present scatterers to the final one at site $\boldsymbol{R}_j$,

$$\hat{T} = \sum_{ij} \hat{\tau}^{ij} \qquad \text{with} \quad \hat{\tau}^{ij} = \hat{t}^i \delta_{ij} + \hat{t}^i \hat{\boldsymbol{G}}_0 \sum_{k \neq i} \hat{\tau}^{kj} = \hat{t}^i \delta_{ij} + \sum_{k \neq j} \hat{\tau}^{ik} \hat{\boldsymbol{G}}_0 \hat{t}^j. \tag{2.34}$$

By means of the angular momentum representation of $\hat{\tau}^{ij}$ and with help of the regular (Z) and irregular ($\tilde{J}$) scattering solutions of the Kohn-Sham equations, evaluated for spherically symmetric site potentials, the Greens function is determined as [70]

$$G(\boldsymbol{r}_n, \boldsymbol{r}'_m; \varepsilon) = \sum_{LL'} Z^n_L(\boldsymbol{r}_n, \varepsilon) \hat{\tau}^{nm}_{LL'} Z^m_L(\boldsymbol{r}'_m, \varepsilon) - \delta_{nm} \sum_L Z^n_L(\boldsymbol{r}_<, \varepsilon) \tilde{J}^n_L(\boldsymbol{r}_>, \varepsilon), \tag{2.35}$$

where $\boldsymbol{r}_<(\boldsymbol{r}_>)$ represents the smaller (greater) vector of $\boldsymbol{r}_n$ or $\boldsymbol{r}'_n$.

Alternatively, one can define the GF by [71]

$$G(\boldsymbol{r}_n, \boldsymbol{r}'_m; \varepsilon) = -\mathrm{i}\alpha \sum_{LL'} J^n_L(\boldsymbol{r}_n, \varepsilon) \hat{U}^{nm}_{LL'} J^m_L(\boldsymbol{r}'_m, \varepsilon) - \delta_{nm} \sum_L J^n_L(\boldsymbol{r}_<, \varepsilon) H^n_L(\boldsymbol{r}_>, \varepsilon), \tag{2.36}$$

where the regular and irregular scattering solutions fulfill $J \to j + \mathrm{i}\alpha h t$ and $H \to h$, respectively ($\alpha = \sqrt{2\varepsilon}$). The use of these asymptotics as well as the explanation of the concepts of j and h are presented in the subsequent section.

For the interpretation of electronic structure calculations the Bloch spectral function [70]

$$A_i(\boldsymbol{k}, \varepsilon) = -\frac{1}{\pi} \mathrm{Im} \left[\mathrm{Tr} G^+_i(\boldsymbol{k}; \varepsilon) \right] \tag{2.37}$$

is used as a tool to analyze electronic transport results with respect to a site $\boldsymbol{R}_i$ and a wave-vector $\boldsymbol{k}$. $G^+_i(\boldsymbol{k}; \varepsilon)$ is the $\boldsymbol{k}$ projected site-diagonal Green function of that site. The trace involves an integration over the MT or ASA sphere and summation over spin-angular quantum numbers.

2.2.2.2 Multiple scattering contributions at a single site

In the following it is assumed that all spherically symmetric potentials $\mathrm{V}^i_{\mathrm{eff}}(\boldsymbol{r}_i)$ centered on sites $\boldsymbol{R}_i$ (2.32) have been determined self-consistently.

According to multiple-scattering theory [72], the wave function for an electron moving in these on-site potentials, $\Psi(\boldsymbol{r})$, can be written as the sum of an wave incoming on the ith site, $\Psi^{\mathrm{in}}(\boldsymbol{r}_i)$, and the wave outgoing from that site, $\Psi^{\mathrm{out}}(\boldsymbol{r}_i)$,

$$\Psi(\boldsymbol{r}) = \Psi^{\mathrm{in}}(\boldsymbol{r}_i) + \Psi^{\mathrm{out}}(\boldsymbol{r}_i). \tag{2.38}$$

Furthermore, the incoming wave with energy ϵ on site i is regarded as a superposition of all waves outgoing from the other sites,

$$\Psi^{\text{in}}(\boldsymbol{r}_i) = \sum_{n \neq i} \Psi^{\text{out}}(\boldsymbol{r}_n). \tag{2.39}$$

In the neighborhood of the ith scatterer, with $r_i > R_s^i$, expressions for $\Psi^{\text{in}}(\boldsymbol{r}_i)$ and $\Psi^{\text{out}}(\boldsymbol{r}_i)$ can be written as linear combinations of scattering solutions for the spherically symmetric single-site potentials,

$$\Psi^{\text{in}}(\boldsymbol{r}_i) = \sum_L a_L^i \, j_l(\alpha r_i) Y_L(\hat{\boldsymbol{r}}_i), \qquad \text{with} \quad \alpha = \sqrt{2\epsilon}, \quad \text{and} \quad L = (l, m), \tag{2.40a}$$

$$\Psi^{\text{out}}(\boldsymbol{r}_i) = \sum_L b_L^i \, h_l^+(\alpha r_i) Y_L(\hat{\boldsymbol{r}}_i). \tag{2.40b}$$

$j_l(\alpha r_i)$ and $h_l^+(\alpha r_i)$ are spherical Bessel or Hankel functions, respectively, while $Y_L(\hat{\boldsymbol{r}}_i)$ are spherical harmonics.

The Hankel functions are singular at the origin, but in the framework of scattering theory [29, 73] one can find a set of coefficients $t_{L'L}^i$ such that

$$\Psi_L^i(\epsilon, \boldsymbol{r}_i) = j_l(\alpha r_i) Y_L(\hat{\boldsymbol{r}}_i) - \mathrm{i}\alpha \sum_{L'} h_{l'}^+(\alpha r_i) Y_{L'}(\hat{\boldsymbol{r}}_i) t_{L'L}^i(\epsilon) \tag{2.41}$$

is regular at $\boldsymbol{r}_i = 0$. These $t_{L'L}^i$ are the elements of the single-site t-matrix in the angular momentum representation and describe the scattering due to $V_{\text{eff}}^i(r_i)$. Please note that the single-site t-matrix becomes for spherically symmetric potentials diagonal in L. The corresponding matrix elements can be obtained either by wave-function matching of $\Psi^{\text{in}}(\boldsymbol{r}_i)$ and $\Psi^{\text{out}}(\boldsymbol{r}_i)$ with regular solutions of the radial Schrödinger equation at R_s^i [32] or by exploiting the Wronskians [64].

It is possible to expand the total wave function in terms of the regular wave functions

$$\Psi(E, \boldsymbol{r}) = \sum_L c_L^i \, \Psi_L^i(E, \boldsymbol{r}_i). \tag{2.42}$$

A comparison with (2.40) inserted into (2.38) reveals on the one hand that $c_L^i = a_L^i$, and on the other hand a relation between the expansion coefficients of the incoming (a_L^i) and outgoing (b_L^i) wave functions, $b_L^i = -\mathrm{i}\alpha \sum_{L'} t_{LL'}^i a_{L'}^i$. Hence, a wave outgoing from a potential sphere $\mathrm{V}_{\text{eff}}^i(\boldsymbol{r}_i)$ can be, for $r_i > R_s^i$, expressed in terms of amplitudes of $\Psi^{\text{in}}(\boldsymbol{r}_i)$ and the respective t-matrix elements of that site. Thus, the total wave function reads

$$\Psi = \sum_L a_L^i \, j_l(\alpha r_i) Y_L(\hat{\boldsymbol{r}}_i) - \mathrm{i}\alpha \sum_L h_l^+(\alpha r_i) Y_L(\hat{\boldsymbol{r}}_i) \sum_{L'} t_{LL'}^i a_{L'}^i. \tag{2.43}$$

After considering the single-site scattering **the scattering at a layer** is briefly regarded next. For this purpose it is assumed that the spherically symmetric potentials are arranged on a two-dimensional, translationally invariant lattice. Hence, the incoming wave function at a reference site i can be decomposed into an intralayer contribution (il) and parts which stem from outside the layer (ol), $\Psi^{\mathrm{in}}(\boldsymbol{r}_i) = \Psi^{\mathrm{in}}_{\mathrm{il}}(\boldsymbol{r}_i) + \Psi^{\mathrm{in}}_{\mathrm{ol}}(\boldsymbol{r}_i)$. According to (2.39) $\Psi^{\mathrm{in}}_{\mathrm{il}}(\boldsymbol{r}_i)$ can be superimposed by all outgoing wave functions from the other sites of the layer, which leads to

$$\Psi^{\mathrm{in}}_{\mathrm{il}}(\boldsymbol{r}_i) = \sum_{j \neq i} \sum_{L} h_l^{+}(\alpha r_j) Y_L(\boldsymbol{r}_j) b_L^j = \sum_L j_l^{+}(\alpha r_i) Y_L(\boldsymbol{r}_i) a^i_{\mathrm{il},L} \tag{2.44a}$$

with the corresponding intralayer amplitudes

$$a^i_{\mathrm{il},L} = \sum_{L''} a^i_{L''} \sum_{j \neq i} e^{\mathrm{i}\boldsymbol{k}_{\|}\boldsymbol{R}_{ij}} \sum_{L'} t^i_{L'L''} G_{L'L}(\boldsymbol{R}_{ij}) = \sum_{L''} a^i_{L''} X_{L''L}. \tag{2.44b}$$

In order to derive the latter, Bloch's theorem [74] was applied to the amplitudes $b_L^j = \exp(\mathrm{i}\boldsymbol{k}_{\|}\boldsymbol{R}_{ij}) b_L^i$. Further, with help of the layer structure constants $G_{L'L}(\boldsymbol{R}_{ij})$ the Hankel functions on site $\boldsymbol{R}_j$ are expressed in terms of Bessel functions at site $\boldsymbol{R}_i$ [29, 73].

Corresponding to (2.44) the intralayer amplitudes are substitutable by those of $\Psi^{\mathrm{in}}(\boldsymbol{r}_i)$ and elements of the multiple-scattering matrix X. Thus, the amplitudes of $\Psi^{\mathrm{in}}(\boldsymbol{r}_i)$ can vice versa be written in a matrix notation as $a^i = a^i_{\mathrm{ol}} + a^i_{\mathrm{il}} = a^i_{\mathrm{ol}} + a^i X = a^i_{\mathrm{ol}}(1 - X)^{-1}$.

Hence, an angular-momentum representation of the total-wave function is calculated on basis of the same expansion coefficients for the sum of superimposed incident and layer-scattered solutions,

$$\Psi = \sum_L a^i_{\mathrm{ol},L}\, j_l(\alpha r_i) Y_L(\hat{\boldsymbol{r}}_i) + \sum_L h_l^{+}(\alpha r_i) Y_L(\hat{\boldsymbol{r}}_i) \sum_{L'L''} a^i_{\mathrm{ol},L''} t_{LL'} (1 - X)^{-1}_{L''L'}. \tag{2.45}$$

Within the layer-KKR formalism it is used that all incoming and scattered wave functions in (2.43) and particularly in (2.45) represent plane waves.

2.2.3 Scattering from layers

2.2.3.1 Scattering by a single layer

The below described elements of the LKKR method [31, 75–77] are applicable for crystalline materials that exhibit two-dimensional lattice periodicity, typically in planes parallel to an interface or a surface. Within this theory one considers the cumulative processes of reflections from, and transmissions through, these individual atomic planes. Divided into intra- and interlayer scatterings, the electron scattering processes in the whole system are treated in two separated steps.

Intralayer multiple scattering processes take place within each layer of atoms (with one or several atoms per unitcell). They are treated in an angular momentum representation (non-relativistically: $\tau, L = (\ell, m)$) as used for the description of single-site scattering processes [32, 64]. This method corresponds to a two-dimensional version of the KKR Green's function method.

Interlayer multiple scattering processes take place between all layers and are formulated in a plane wave (PW) representation.

In the following, only the case of one site per layer unit cell will be addressed. The wave fields incident on a layer (Ψ_{inc}) and outgoing from a layer (Ψ_{out}),

$$\Psi_{\text{inc}}(\boldsymbol{k}_{\|}, \boldsymbol{r}) = \sum_{g\tau} \left[u^{+}_{g\tau} \exp(i\boldsymbol{k}^{+}_{g\tau} \cdot \boldsymbol{r}) + u^{-}_{g\tau} \exp(i\boldsymbol{k}^{-}_{g\tau} \cdot \boldsymbol{r}) \right] \chi^{\tau}, \tag{2.46a}$$

$$\Psi_{\text{out}}(\boldsymbol{k}_{\|}, \boldsymbol{r}) = \sum_{g\tau} \left[v^{+}_{g\tau} \exp(i\boldsymbol{k}^{+}_{g\tau} \cdot \boldsymbol{r}) + v^{-}_{g\tau} \exp(i\boldsymbol{k}^{-}_{g\tau} \cdot \boldsymbol{r}) \right] \chi^{\tau}. \tag{2.46b}$$

are expressed in terms of an energy-dependent PW basis. The $+(-)$ sign refers to plane waves propagating or decaying in the $+z$ $(-z)$ direction. Pauli spinors χ^{τ}, with $\tau = (\uparrow \equiv +1, \downarrow \equiv -1)$, are quantized along the z axis, $\sigma_z \chi^{\tau} = \tau \chi^{\tau}$. All plane waves are characterized by 2-dimensional reciprocal lattice vectors $\boldsymbol{g}$ which define individual wave vectors $\boldsymbol{k}^{\pm}_{g}$ via

$$\boldsymbol{k}^{\pm}_{g} = \begin{pmatrix} \boldsymbol{k}_{\|} + \boldsymbol{g} \\ k^{\pm}_{g,z} \end{pmatrix}, \tag{2.47a}$$

and

$$k^{\pm}_{g,z} = \begin{cases} \pm\sqrt{2E - (\boldsymbol{k}_{\|} + \boldsymbol{g})^2}, & 2E > (\boldsymbol{k}_{\|} + \boldsymbol{g})^2, \\ \pm\mathrm{i}\sqrt{(\boldsymbol{k}_{\|} + \boldsymbol{g})^2 - 2E}, & 2E < (\boldsymbol{k}_{\|} + \boldsymbol{g})^2. \end{cases} \tag{2.47b}$$

Increasing $|\boldsymbol{g}|$ cause increasing imaginary components of $k^{\pm}_{g,z}$ with the result that the corresponding PWs, evaluated at an adjacent layer, become increasingly less important. This attenuation allows a truncation of the plane-wave basis, with typically 30 - 50 vectors [76,77]. Hence, a set of N_g wave vectors—which is the same for both spin projections τ—is used for the construction of the PW fields. For a given $\boldsymbol{k}_\|$ these sets are defined by all those $\boldsymbol{g}$ vectors which obey $(\boldsymbol{k}_\| + \boldsymbol{g})^2 < 2E_{\text{max}}$. In particular, this means that all N_g in-plane components of $\boldsymbol{k}_g^\pm$ lie within a fixed energy radius $\sqrt{2E_{\text{max}}}$ (see Fig. 2.3). The energy $E_{\text{max}} \geq \frac{1}{2}(\boldsymbol{k}_\| + \boldsymbol{g})^2$ has to be chosen such that PWs with maximal $\boldsymbol{g}$-vectors decay rapidly enough and do practically not appear at adjacent layers.

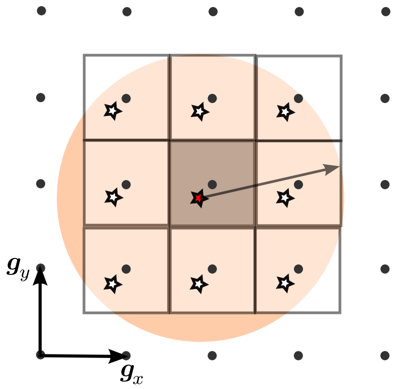

Figure 2.3: Schematic representation of a two-dimensional reciprocal lattice and its Brillouin zones (BZs). The red star marks a $\boldsymbol{k}_\|$-vector within the 1. BZ. The white stars form a set of N_g wave vectors $\boldsymbol{k}_{g\|} = \{\boldsymbol{k}_\| + \boldsymbol{g}\}$ which lie within a given energy radius $\sqrt{2E_{\text{max}}}$ such that $E_{\text{max}} \geq \frac{1}{2}(\boldsymbol{k}_\| + \boldsymbol{g})^2$. The set of vectors which belongs to $\boldsymbol{k}_{g\|}$ is often referred to as "beam" set.

Writing the coefficients $u_{g\tau}^\pm$ and $v_{g\tau}^\pm$ as column vectors, the connection between these is defined in terms of the scattering matrix M of the layer (see Fig. 2.4),

$$\begin{pmatrix} \boldsymbol{v}^+ \\ \boldsymbol{v}^- \end{pmatrix} = \begin{pmatrix} M^{++} & M^{+-} \\ M^{-+} & M^{--} \end{pmatrix} \begin{pmatrix} \boldsymbol{u}^+ \\ \boldsymbol{u}^- \end{pmatrix} . \tag{2.48}$$

The majority of scattering events do not affect the electron spin. The main sources of spin-flip processes in magnetic metals are the spin-orbit coupling and magnon scattering. The spin-orbit coupling in 3d metals is weak. The density of magnons increases with temperature, from near zero to a relatively low value at room temperature because the Curie temperature of the most commonly used 3d materials like Fe, Co, Ni and their alloys is well above room temperature [78].

As a consequence, it may be considered that spin-up and spin-down electrons conduct in parallel currents $(I_\uparrow, I_\downarrow)$ which do not mix. This model, in which the total current is given by the sum of both separate contributions, is known as Mott's two-current model [79]. Since the DFT operates at zero temperature and spin-orbit coupling will not be addressed in the following, this two-current model represents the framework in all following considerations.

Consequently, the matrices $M^{\pm\pm}$ have dimension $2N_g \times 2N_g$ and are diagonal superblock matri-

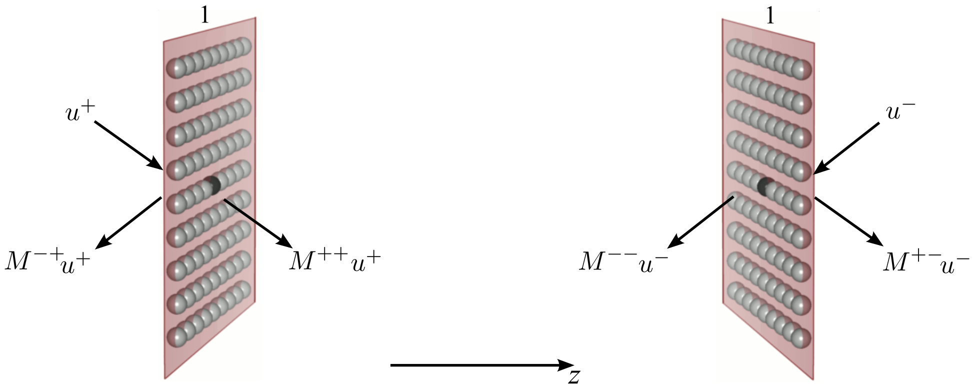

Figure 2.4: Schematic view of scattering by a single layer, i.e., a two-dimensional periodic arrangement of scatterers (gray spheres). The scattering properties of the entire layer are characterized in terms of the four plane wave scattering matrices $M^{\pm\pm}$. The reference scatterer is represented by a dark gray sphere. Incoming plane waves $u^{\pm}_{g\tau}$ that are scattered into outgoing ones ($v^{\pm}_{g\tau}$) are labeled with respect to the propagation direction ($\pm z$).

ces, where each block represents the spin conserving scattering properties (2.48) corresponding to one spin type

$$M^{\pm\pm} = \begin{pmatrix} M^{\pm\pm}_{\uparrow} & 0 \\ 0 & M^{\pm\pm}_{\downarrow} \end{pmatrix}. \tag{2.49}$$

The layer matrices $M^{\pm\pm}_{\tau}$ which describe the reflection ($M^{-+}_{\tau}, M^{+-}_{\tau}$) and transmission ($M^{++}_{\tau}, M^{--}_{\tau}$) of the plane waves are given by

$$M^{-+}_{\tau} = \Gamma^{-}_{g\tau L} t(1-X)^{-1}\Gamma^{+}_{Lg\tau}, \qquad M^{++}_{\tau} = 1 + \Gamma^{+}_{g\tau L} t(1-X)^{-1}\Gamma^{+}_{Lg\tau}, \tag{2.50a}$$

$$M^{+-}_{\tau} = \Gamma^{+}_{g\tau L} t(1-X)^{-1}\Gamma^{-}_{Lg\tau}, \qquad M^{--}_{\tau} = 1 + \Gamma^{-}_{g\tau L} t(1-X)^{-1}\Gamma^{-}_{Lg\tau}, \tag{2.50b}$$

where $\Gamma^{\pm}_{Lg\tau}$ projects according to (2.45) a plane wave onto the angular-momentum basis and $\Gamma^{\pm}_{g\tau L}$ projects it back onto plane waves [76]. As discussed in section 2.2.2.2 the multiple-scattering matrix X is computed in the angular-momentum representation at a reference site of the layer (see Fig. 2.4).

2.2.3.2 Scattering of multiple layers

In order to calculate the scattering properties of an arbitrary stack of layers, one starts with the M-matrix of a double layer, i.e. a stack of two adjacent layers. The M-matrix of the entire stack can be calculated by a consecutive application of the following computational scheme which is referred to as **layer doubling method**.

The procedure starts with a stack consisting of two layers, labeled 1 and 2, which need not be

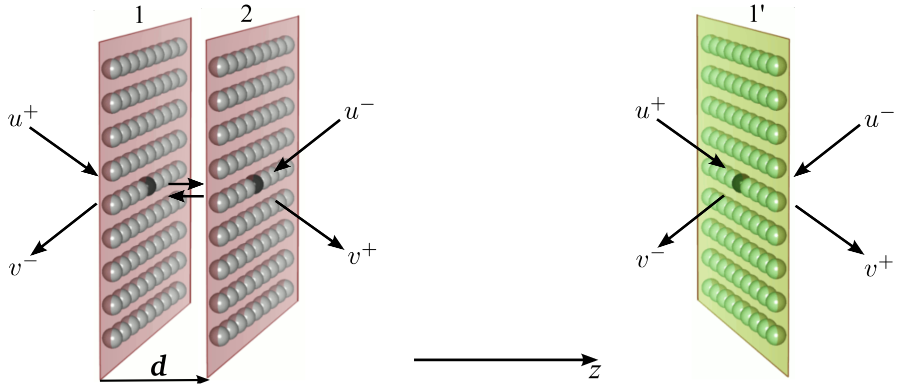

Figure 2.5: Schematic representation of scattering by a stack of two layers (1 and 2, left). The scattering properties can be cast into an effective scatterer (1', right).

identical (see Fig. 2.5). The result is the M-matrix of this stack, labeled 1',

$$\begin{pmatrix} \boldsymbol{v}^+ \\ \boldsymbol{v}^- \end{pmatrix} = \begin{pmatrix} M_{1'}^{++} & M_{1'}^{+-} \\ M_{1'}^{-+} & M_{1'}^{--} \end{pmatrix} \begin{pmatrix} \boldsymbol{u}^+ \\ \boldsymbol{u}^- \end{pmatrix}. \tag{2.51}$$

Summing up all multiple-scattering events which are due to reflection at each layer, one obtains for the amplitudes of the plane waves

$$\begin{aligned} \boldsymbol{v}^+ &= M_2^{++}P^+(1 - M_1^{+-}P^-M_2^{-+}P^+)^{-1}M_1^{++}\boldsymbol{u}^+ \\ &\quad + \left[M_2^{+-} + M_2^{++}P^+M_1^{+-}P^-(1 - M_2^{-+}P^+M_1^{+-}P^-)^{-1}M_2^{--}\right]\boldsymbol{u}^-, \end{aligned} \tag{2.52a}$$

$$\begin{aligned} \boldsymbol{v}^- &= \left[M_1^{-+} + M_1^{--}P^-M_2^{-+}P^+(1 - M_1^{+-}P^-M_2^{-+}P^+)^{-1}M_1^{++}\right]\boldsymbol{u}^+ \\ &\quad + M_1^{--}P^-(1 - M_2^{-+}P^+M_1^{+-}P^-)^{-1}M_2^{--}\boldsymbol{u}^-, \end{aligned} \tag{2.52b}$$

using the geometric series $1 + x + x^2 + x^3 + \ldots = (1 - x)^{-1}$. The elements of the diagonal matrices $P^\pm$ are defined by the propagators

$$P^\pm_{g\tau,g'\tau'} = \exp(\mathrm{i}\boldsymbol{k}_g^\pm \cdot \boldsymbol{d})\delta_{gg'}\delta_{\tau\tau'}, \tag{2.53}$$

where $\boldsymbol{d}$ is the translation vector from layer 1 to layer 2.

By reading from right to left, the achieved expressions can be understood in the following way. The term $M_2^{++}P^+(1 - M_1^{+-}P^-M_2^{-+}P^+)^{-1}M_1^{++}\boldsymbol{u}^+$ describes for instance the transmission of an incoming PW ($\boldsymbol{u}^+$) through layer 1 (M_1^{++}), all forward and backward propagations by means of PW propagators ($P^\pm$), and their multiple backward scatterings into the opposite directions at the layers 2 (M_2^{-+}) and 1 (M_1^{+-}), finishing by a transmission through layer 2 (M_2^{++}) into an outgoing PW ($\boldsymbol{v}^+$).

For convenience matrices $N^{\pm\pm}$ are introduced, i.e., $M^{\pm\pm}$-matrices enhanced by plane-wave

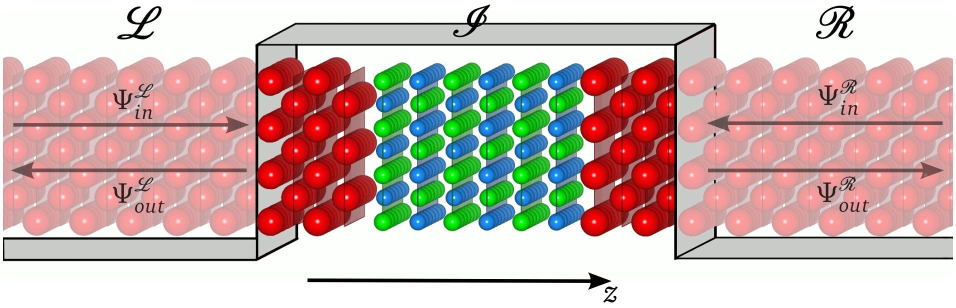
$\mathscr{L}$
$\mathscr{I}$
$\mathscr{R}$
$\Psi^{\mathscr{L}}_{in}$
$\Psi^{\mathscr{L}}_{out}$
$\Psi^{\mathscr{R}}_{in}$
$\Psi^{\mathscr{R}}_{out}$
z

Figure 2.6: Schematic side-view of the principle scattering regions for the electronic transport by using the example of an Fe/MgO/Fe tunnel contact. A semi-infinite lead $\mathscr{L}$ or $\mathscr{R}$ is characterized by identical layers, equal layer distances $\boldsymbol{d}_z$ and the same layer scattering matrices $M^{\pm\pm}_{\mathscr{L}}$ and $M^{\pm\pm}_{\mathscr{R}}$. The interface region $\mathscr{I}$ consists of layers with different scattering properties and with various layer distances. By a sequent application of the layer doubling method, sketched in Fig. 2.5, one obtains an effective interface scattering matrix $N_{\mathscr{I}}$, which forms a quasi 1-dimensional scattering barrier for all incoming and outgoing wave functions in $\mathscr{L}$ and $\mathscr{R}$.

propagators $P^{\pm}$: $N^{++} = P^{+}M^{++}, N^{+-} = P^{+}M^{+-}P^{-}, N^{-+} = M^{-+}$, and $N^{--} = M^{--}P^{-}$, which yields [71]

$$N^{++}_{1'} = N^{++}_{2}(1 - N^{+-}_{1}N^{-+}_{2})^{-1}N^{++}_{1}, \tag{2.54a}$$

$$N^{+-}_{1'} = N^{+-}_{2} + N^{++}_{2}N^{+-}_{1}(1 - N^{-+}_{2}N^{+-}_{1})^{-1}N^{--}_{2}, \tag{2.54b}$$

$$N^{-+}_{1'} = N^{-+}_{1} + N^{--}_{1}N^{-+}_{2}(1 - N^{+-}_{1}N^{-+}_{2})^{-1}N^{++}_{1}, \tag{2.54c}$$

$$N^{--}_{1'} = N^{--}_{1}(1 - N^{-+}_{2}N^{+-}_{1})^{-1}N^{--}_{2}. \tag{2.54d}$$

2.2.4 Bloch-wave scattering and conductance

Once the scattering properties of all layers are known one can calculate the system's conductance. This is done by partitioning the space, as shown in Fig. 2.6, into three principle scattering regions $\mathscr{L}$, $\mathscr{I}$, and $\mathscr{R}$ with respect to the transport direction z. The semi-infinite leads exhibit bulk-like properties, represented by infinite repetitions of identical layers or stacks of layers. $\mathscr{L}$ or $\mathscr{R}$ might represent different materials.

In between $\mathscr{L}$ or $\mathscr{R}$ lies the scattering region $\mathscr{I}$, comprising all layers that are different from those in $\mathscr{L}$ and $\mathscr{R}$. These layers form together, for instance, the scattering region of e.g. a surface, thin film or interface. Using the layer doubling method (paragraph 2.2.3.2) the scattering properties of all individual layers are merged into single effective matrices $N^{\pm\pm}_{\mathscr{I}}$.

In the following sections it is described how the conductance calculations can be performed in terms of transmission channels within the framework of Landauer-Büttiker theory. For this purpose it will be shown how one achieves a Bloch wave (BW) representation of the PW fields in the semi-infinite leads $\mathscr{L}$ and $\mathscr{R}$. Afterwards it will be discussed how these states can be connected by means of the interface scattering matrices $N^{\pm\pm}$. The latter have to be expressed therefore in terms of BW basis sets that belong to $\mathscr{L}$ and $\mathscr{R}$.

2.2.4.1 The Bloch-wave representation within the leads

The M-matrix of a bulk layer can be used to compute the Bloch states in the leads. For this reason an expression for the BW is constructed via a superposition of incoming $\boldsymbol{u}^+$ and outgoing $\boldsymbol{v}^-$ plane waves of that bulk layer:

$$\psi^\tau(\boldsymbol{r})\chi^\tau = \sum_{g}^{N_g} \left[u_{g\tau}^+ \exp(i\boldsymbol{k}_{g\tau}^+ \cdot \boldsymbol{r}) + v_{g\tau}^- \exp(i\boldsymbol{k}_{g\tau}^- \cdot \boldsymbol{r}) \right] \chi^\tau . \tag{2.55}$$

Note that N_g is the number of reciprocal lattice vectors $\boldsymbol{g}$ defined in (2.47a) and $\psi(\boldsymbol{r})$ is calculated for a fixed energy E and a specified in-plane momentum $\boldsymbol{k}_\parallel$. Labeling further that bulk layer with 1 and its identical neighbor layer in distance $\boldsymbol{d}$ with 2, one can find a condition for the Bloch coefficients due to application of Floquet's theorem $\psi(\boldsymbol{r}+\boldsymbol{d}) = \lambda\psi(\boldsymbol{r})$ [80]. As illustrated in Fig. 2.7 one finds that incoming $u_{g\tau}^+$ and outgoing $v_{g\tau}^-$ PWs on the left-hand side of layer 1, are the same at layer 2 but multiplied by a factor λ. Thus, the outgoing waves $\lambda u_{g\tau}^+$ and $v_{g\tau}^-$ are related

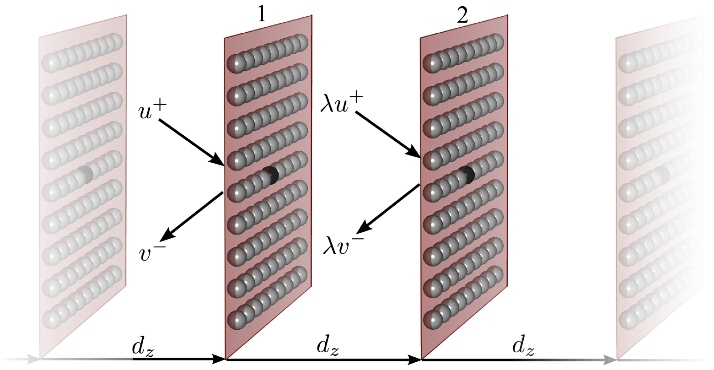

Figure 2.7: Bloch waves in multiple-scattering theory. For identical layers (1 and 2), plane waves on the right $(\lambda\boldsymbol{u}^+, \lambda\boldsymbol{v}^-)$ are multiples of those on the left $(\boldsymbol{u}^+, \boldsymbol{v}^-)$ due to Floquet's theorem.

to the incoming waves $u_{g\tau}^+$ and $\lambda v_{g\tau}^-$ by

$$\lambda u_{g\tau}^+ = N^{++} u_{g\tau}^+ + \lambda N^{+-} v_{g\tau}^-, \tag{2.56a}$$

$$v_{g\tau}^- = N^{-+} u_{g\tau}^+ + \lambda N^{--} v_{g\tau}^- . \tag{2.56b}$$

In matrix notation, the eigenvectors and -values can be obtained from the generalized eigenvalue problem

$$\begin{pmatrix} N^{++} & 0 \\ -N^{-+} & 1 \end{pmatrix} \begin{pmatrix} \boldsymbol{u}^{+} \\ \boldsymbol{v}^{-} \end{pmatrix} = \lambda \underbrace{\begin{pmatrix} 1 & -N^{+-} \\ 0 & N^{--} \end{pmatrix}}_{M_{\mathrm{rhs}}} \begin{pmatrix} \boldsymbol{u}^{+} \\ \boldsymbol{v}^{-} \end{pmatrix}, \tag{2.57}$$

which can be solved by standard numerical program packages. However, by multiplying by the inverse matrix of the right-hand side, $M_{\mathrm{rhs}}^{-1} = \begin{pmatrix} 1 & N^{+-}(N^{--})^{-1} \\ 0 & (N^{--})^{-1} \end{pmatrix}$, the above matrix equation can be transformed into a standard form,

$$\begin{pmatrix} Q^{++} & Q^{+-} \\ Q^{-+} & Q^{--} \end{pmatrix} \begin{pmatrix} \boldsymbol{u}^{+} \\ \boldsymbol{v}^{-} \end{pmatrix} = \lambda \begin{pmatrix} \boldsymbol{u}^{+} \\ \boldsymbol{v}^{-} \end{pmatrix}, \tag{2.58}$$

with the blocks of Q given by

$$Q^{++} = N^{++} - N^{+-}(N^{--})^{-1}N^{-+}, \tag{2.59a}$$

$$Q^{+-} = N^{+-}(N^{--})^{-1}, \tag{2.59b}$$

$$Q^{-+} = -(N^{--})^{-1}N^{-+}, \tag{2.59c}$$

$$Q^{--} = (N^{--})^{-1}. \tag{2.59d}$$

The number of eigenvalues and eigenvectors corresponds to the number of PW coefficients $u^{+}_{g\tau}$ and $v^{-}_{g\tau}$ in (2.55). Thus, the total number of eigenpairs is $4N_g$. With respect to the spin τ there are $2N_g$ components which describe propagating or decaying PWs into $+z$ or $-z$ direction. The eigenvalues λ_n are in general complex and fulfill the conditions of Bloch's theorem [74] if $|\lambda_n| = 1$,

$$\psi_n(\boldsymbol{r}+\boldsymbol{d}) = \lambda\psi_n(\boldsymbol{r}) = e^{\mathrm{i}\boldsymbol{k}_n\cdot\boldsymbol{d}}\psi_n(\boldsymbol{r}), \tag{2.60}$$

which describes the equivalence of propagating BWs in a periodic crystal potential that are spatially separated by lattice vectors $\boldsymbol{d}$. The wave vectors $\boldsymbol{k}_n$ of the BWs are decomposed into components parallel to the layer, $\boldsymbol{k}_{\|}$, and along the propagation direction, $k_{z,n}$. As a feature of the method the bulk bandstructure $k_{z,n}(E, \boldsymbol{k}_{\|})$ is obtained from

$$k_{z,n} = \frac{-\mathrm{i}}{d_z}\left(\ln\lambda_n - \mathrm{i}\boldsymbol{k}_{\|}\cdot\boldsymbol{d}_{\|}\right). \tag{2.61}$$

Eigenfunctions with $|\lambda_n| = 1$ belong to the real band structure, with vanishing imaginary parts of $k_{z,n}$, see Fig. 2.8.

Commonly the wave functions are normalized with respect to their probability density $|\psi_n|^2$ or probability current $\mathrm{Im}[\psi_n^*\nabla\psi_n]$.

In this context appears a problem, because even if the energy is real, the set of eigenvalues $\{\lambda_n\}$

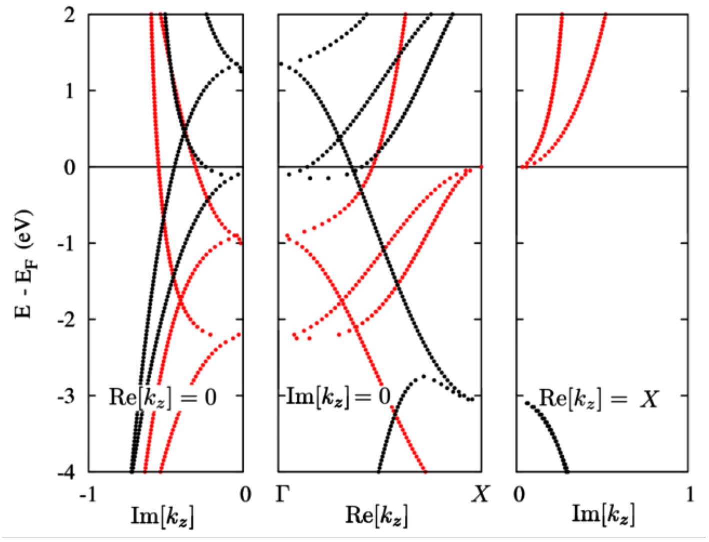

Figure 2.8: Complex Bloch eigenvalues $k_{z,n}(E,\boldsymbol{k}_{\|})$ calculated for bcc Fe(001) at $\boldsymbol{k}_{\|} = 0$. The k_z are decomposed with respect to their spin τ (↑ red, ↓ black) and sorted with regard to their real and imaginary parts. The left, middle and right panel display bands with $\mathrm{Im}[k_z] \neq 0 \,\&\, \mathrm{Re}[k_z] = 0$, $\mathrm{Im}[k_z] = 0 \,\&\, \mathrm{Re}[k_z] \neq 0$, and $\mathrm{Im}[k_z] \neq 0 \,\&\, \mathrm{Re}[k_z] = X (= \pi/a)$. Complex bands with simultaneously non-vanishing real and imaginary parts are not shown.

with non-vanishing imaginary parts of $k_{z,n}$ consists of values with modulus greater or less than 1 ($|\lambda_n| = \exp(\mathrm{Im}[k_{z,n}] \cdot d_z)$). In particular, the norms $|\psi_n|^2$ of the corresponding wave functions are not constant but increase or decrease when propagating across a layer. These solutions cannot be normalized in the bulk because only square-integrable functions ($\mathscr{L}_2$-functions) belong to the Hilbert space.

The problem can be solved in the presence of a surface or interface. Then the normalization can be carried out in the half-space $z > 0$ or $z < 0$. Thus, in addition to propagating Bloch states, solutions with $|\lambda_n| < 1$ ($\mathrm{Im}[k_{z,n}] < 0$) or $|\lambda_n| > 1$ ($\mathrm{Im}[k_{z,n}] > 0$) are allowed. The latter are the evanescent states, i.e., those states with decreasing amplitude when propagating into the interior of the semi-infinite solid. The eigenvalues of these states with $\mathrm{Im}[k_{z,n}] \neq 0$ form the complex bandstructure as a continuation of the real bandstructure, which is shown for example in Fig. 2.8 calculated for a bcc Fe bulk crystal.

The intrinsic symmetry of the eigenvalue problem allows to classify the BWs into two subsets those with identical absolute value of k_z but different sign $\pm k_z$,

$$\psi^{\tau}_{k_z^{\pm}}(\boldsymbol{r})\chi^{\tau} = \sum_{g}^{N_g} \left[u^{+}_{k_z^{\pm},g\tau} \exp\left(i\boldsymbol{k}^{+}_{g\tau} \cdot \boldsymbol{r}\right) + v^{-}_{k_z^{\pm},g\tau} \exp\left(i\boldsymbol{k}^{-}_{g\tau} \cdot \boldsymbol{r}\right) \right] \chi^{\tau}. \tag{2.62}$$

Since E is a periodic function of k_z, i.e. $E(k_z^{+}) = E(-k_z^{+}) = E(k_z^{-})$, it follows that for a given value of $\boldsymbol{k}_{\|}$ there will be exactly as many propagating states with positive v_z as with negative. Hence, in addition to the eigenvalues, it is essential to compute the z component of the group velocity v_z so that the direction of travel of each BW can be determined, and consequently whether the state belongs to the subset of left or right traveling Bloch waves.

It turns out that this information can be extracted from the eigenvalues $k_z(E, \boldsymbol{k}_{\|})$ without need to resort to numerical differentiation [81]. v_z is found by noting that $E(k_z)$ is an analytic function of the wave vector $\boldsymbol{k}_n$. Thus, if a tiny imaginary part Im$[E]$ is added to the energy, as is standard in KKR [64], the k_z will also have an imaginary part. The Cauchy-Riemann equations then give

$$v_z = \hbar^{-1}\frac{\partial \mathrm{Re}[E]}{\partial \mathrm{Re}[k_z]} = \hbar^{-1}\frac{\partial \mathrm{Im}[E]}{\partial \mathrm{Im}[k_z]} \approx \hbar^{-1}\frac{\mathrm{Im}[E]}{\mathrm{Im}[k_z]}. \tag{2.63}$$

The presence of a tiny imaginary part does not alter the real part of k_z, hence both v_z and k_z can be found simultaneously.

If all BWs in (2.62) are representable as multiples of a row eigenvector $(u^{+}_{k_z^{\pm},g_1\tau} \cdots \; v^{-}_{k_z^{\pm},g_1\tau} \cdots)$ with the $2N_g$-component column vector $(\exp(i\boldsymbol{k}^{+}_{g_1\tau} \cdot \boldsymbol{r}), \ldots, \exp(i\boldsymbol{k}^{-}_{g_1\tau} \cdot \boldsymbol{r}), \ldots)$ one finds an expansion of the PWs in terms of BWs

$$\exp(i\boldsymbol{k}^{\pm}_{g\tau} \cdot \boldsymbol{r})\chi^{\tau} = \sum_{\boldsymbol{k}_z^{+}} \mu^{\pm}_{g\tau,\boldsymbol{k}_z^{+}} \psi^{\tau}_{\boldsymbol{k}_z^{+}}(\boldsymbol{r}) + \sum_{\boldsymbol{k}_z^{-}} \mu^{\pm}_{g\tau,\boldsymbol{k}_z^{-}} \psi^{\tau}_{\boldsymbol{k}_z^{-}}(\boldsymbol{r}). \tag{2.64}$$

The expansion coefficients $\mu^{\pm}_{g\tau,\boldsymbol{k}_z^{\pm}}$ are calculated from the inverse eigenvector matrix. Please note that the inverted matrix comprises all eigenvector solutions $\boldsymbol{u}^{+}$ and $\boldsymbol{v}^{-}$ in (2.58), i.e. all propagating plus evanescent state solutions; and that an incoming (outgoing) PW in (2.64) is composed by a superposition of both, incident and outgoing BWs.

2.2.4.2 The interface scattering matrix in terms of Bloch waves

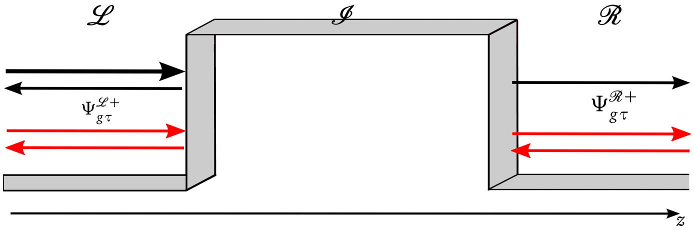

Figure 2.9: Sketch of the scattering situation at the interface region. Black arrows represent incident plane waves in $\mathscr{L}$ and their forward and backward scattered parts into all outgoing PWs in $\mathscr{L}$ and $\mathscr{R}$. The corresponding total wave functions in $\mathscr{L}$ ($\Psi^{\mathscr{L}+}_{g\tau}$) and $\mathscr{R}$ ($\Psi^{\mathscr{R}+}_{g\tau}$) are expressed in terms of the Bloch-wave bases. The latter comprise incoming *and* outgoing BWs (illustrated by the red arrows).

The following procedure was originally introduced and discussed by MacLaren et al. [81]. After computing the effective scattering matrix $N_{\mathscr{I}}$ in terms of a plane-wave basis, and after finding BW representations for the present PWs within the leads, one has to determine subsequently a transformation of $N_{\mathscr{I}}$ into this new basis set. The new scattering matrix

$$T_{\mathscr{I}} = \begin{pmatrix} T^{++} & T^{+-} \\ T^{-+} & T^{--} \end{pmatrix} \tag{2.65}$$

describes the scattering of all incoming into all outgoing BWs in both, $\mathscr{L}$ and $\mathscr{R}$.

For this purpose one considers the previously solved problem for incoming plane-wave fields that are scattered at the interface barrier and replaces each single PW with help of the Bloch-wave basis (2.64). Correspondingly, one achieves for an incident PW in $\mathscr{L}$, see Fig. 2.9, an expression for the basis transformation of the total wave function

$$\Psi^{\mathscr{L}+}_{\boldsymbol{g}\tau} = \exp\left(i\boldsymbol{k}^{+}_{\boldsymbol{g}\tau}\cdot\boldsymbol{r}\right) + \sum_{\boldsymbol{g}'} N^{+-}_{\mathscr{I},\boldsymbol{g}\tau\boldsymbol{g}'\tau}\exp\left(i\boldsymbol{k}^{-}_{\boldsymbol{g}'\tau}\cdot\boldsymbol{r}\right), \tag{2.66a}$$

$$\begin{aligned} &= \sum_{\boldsymbol{k}_z^{+}}\left(\mu^{\mathscr{L}+}_{\boldsymbol{g}\tau,\boldsymbol{k}_z^{+}} + \sum_{\boldsymbol{g}'} N^{+-}_{\mathscr{I},\boldsymbol{g}\tau\boldsymbol{g}'\tau}\,\mu^{\mathscr{L}-}_{\boldsymbol{g}'\tau,\boldsymbol{k}_z^{+}}\right)\psi^{\mathscr{L}\tau}_{\boldsymbol{k}_z^{+}} \\ &\quad + \sum_{\boldsymbol{k}_z^{-}}\left(\mu^{\mathscr{L}+}_{\boldsymbol{g}\tau,\boldsymbol{k}_z^{-}} + \sum_{\boldsymbol{g}'} N^{+-}_{\mathscr{I},\boldsymbol{g}\tau\boldsymbol{g}'\tau}\,\mu^{\mathscr{L}-}_{\boldsymbol{g}'\tau,\boldsymbol{k}_z^{-}}\right)\psi^{\mathscr{L}\tau}_{\boldsymbol{k}_z^{-}}, \end{aligned} \tag{2.66b}$$

$$= \sum_{\boldsymbol{k}_z^{+}} A^{\mathscr{L}+}_{\boldsymbol{g}\tau,\boldsymbol{k}_z^{+}}\,\psi^{\mathscr{L}\tau}_{\boldsymbol{k}_z^{+}} + \sum_{\boldsymbol{k}_z^{-}} A^{\mathscr{L}+}_{\boldsymbol{g}\tau,\boldsymbol{k}_z^{-}}\,\psi^{\mathscr{L}\tau}_{\boldsymbol{k}_z^{-}}, \tag{2.66c}$$

with the Bloch amplitudes

$$A^{\mathscr{L}+}_{\boldsymbol{g}\tau,\boldsymbol{k}_z^{\pm}} = \mu^{\mathscr{L}+}_{\boldsymbol{g}\tau,\boldsymbol{k}_z^{\pm}} + \sum_{\boldsymbol{g}'} N^{+-}_{\mathscr{I},\boldsymbol{g}\tau\boldsymbol{g}'\tau}\,\mu^{\mathscr{L}-}_{\boldsymbol{g}'\tau,\boldsymbol{k}_z^{\pm}} \tag{2.66d}$$

Analogous expressions hold for the corresponding total wave function in $\mathscr{R}$,

$$\Psi^{\mathscr{R}+}_{\boldsymbol{g}\tau} = \sum_{\mathbf{k}_z^{+}} A^{\mathscr{R}+}_{\boldsymbol{g}\tau,\mathbf{k}_z^{+}}\,\psi^{\mathscr{R}\tau}_{\mathbf{k}_z^{+}} + \sum_{\mathbf{k}_z^{-}} A^{\mathscr{R}+}_{\boldsymbol{g}'\tau,\mathbf{k}_z^{-}}\,\psi^{\mathscr{R}\tau}_{\mathbf{k}_z^{-}}, \tag{2.67a}$$

and

$$A^{\mathscr{R}+}_{\boldsymbol{g}\tau,\mathbf{k}_z^{\pm}} = \sum_{\boldsymbol{g}'} N^{++}_{\mathscr{I},\boldsymbol{g}\tau\boldsymbol{g}'\tau}\,\mu^{\mathscr{R}+}_{\boldsymbol{g}'\tau,\mathbf{k}_z^{\pm}}. \tag{2.67b}$$

The notations $\boldsymbol{k}_z^{\pm}$ (italic) and $\mathbf{k}_z^{\pm}$ (non-italic) are introduced to distinguish the Bloch-wave basis sets found in $\mathscr{L}$ and $\mathscr{R}$. The whole process of interface scattering is now enclosed within the

Bloch coefficients (2.66d) and (2.67b). Then the amplitudes of outgoing Bloch waves on the left hand side $A^{\mathscr{L}+}_{\boldsymbol{k}_z^-}$ will be the sum of the transmitted BWs from the right hand side $T^{--}A^{\mathscr{R}+}_{\mathbf{k}_z^-}$ and the reflected parts of Bloch waves incident from the left $T^{+-}A^{\mathscr{L}+}_{\boldsymbol{k}_z^+}$. Thus $A^{\mathscr{L}+}_{\boldsymbol{g}\tau,\boldsymbol{k}_z^-}$ is given by

$$A^{\mathscr{L}+}_{\boldsymbol{g}\tau,\boldsymbol{k}_z^-} = \sum_{\tilde{\boldsymbol{k}}_z^+} T^{+-}_{\boldsymbol{k}_z^-\tilde{\boldsymbol{k}}_z^+} A^{\mathscr{L}+}_{\boldsymbol{g}\tau,\tilde{\boldsymbol{k}}_z^+} + \sum_{\tilde{\mathbf{k}}_z^-} T^{--}_{\boldsymbol{k}_z^-\tilde{\mathbf{k}}_z^-} A^{\mathscr{R}+}_{\boldsymbol{g}\tau,\tilde{\mathbf{k}}_z^-}, \tag{2.68a}$$

where $T^{+-}_{\boldsymbol{k}_z^-\tilde{\boldsymbol{k}}_z^+}$ and $T^{--}_{\boldsymbol{k}_z^-\tilde{\mathbf{k}}_z^-}$ are the reflection coefficients for Bloch waves incident from the left, and the transmission coefficients for Bloch waves incident from the right, respectively.

The right-traveling Bloch waves in $\mathscr{R}$ read analogously

$$A^{\mathscr{R}+}_{\boldsymbol{g}\tau,\mathbf{k}_z^+} = \sum_{\tilde{\boldsymbol{k}}_z^+} T^{++}_{\mathbf{k}_z^+\tilde{\boldsymbol{k}}_z^+} A^{\mathscr{L}+}_{\boldsymbol{g}\tau,\tilde{\boldsymbol{k}}_z^+} + \sum_{\tilde{\mathbf{k}}_z^-} T^{-+}_{\mathbf{k}_z^+\tilde{\mathbf{k}}_z^-} A^{\mathscr{R}+}_{\boldsymbol{g}\tau,\tilde{\mathbf{k}}_z^-}. \tag{2.68b}$$

$T^{++}_{\mathbf{k}_z^+\tilde{\boldsymbol{k}}_z^+}$ and $T^{-+}_{\mathbf{k}_z^+\tilde{\mathbf{k}}_z^-}$ are the transmission coefficients for Bloch waves incident from $\mathscr{L}$ towards the interface barrier, and reflection coefficients for Bloch waves incident from $\mathscr{R}$.

A similar calculation for $\Psi^{\mathscr{L}-}_{\boldsymbol{g}\tau}$ and $\Psi^{\mathscr{R}-}_{\boldsymbol{g}\tau}$ can be performed for an incident plane wave from the right. The formulas for the coefficients $A^{\mathscr{L}-}_{\boldsymbol{g}\tau,\boldsymbol{k}_z^\pm}$, $A^{\mathscr{R}-}_{\boldsymbol{g}\tau,\mathbf{k}_z^\pm}$ are easily obtained by swapping the superscripts $\mathscr{L}$ and $\mathscr{R}$ and "+" and "−" on the plane-wave labels in (2.66d) and (2.67b). With

$$A^{\mathscr{L}-}_{\boldsymbol{g}\tau,\boldsymbol{k}_z^-} = \sum_{\tilde{\boldsymbol{k}}_z^+} T^{+-}_{\boldsymbol{k}_z^-\tilde{\boldsymbol{k}}_z^+} A^{\mathscr{L}-}_{\boldsymbol{g}\tau,\tilde{\boldsymbol{k}}_z^+} + \sum_{\tilde{\mathbf{k}}_z^-} T^{--}_{\boldsymbol{k}_z^-\tilde{\mathbf{k}}_z^-} A^{\mathscr{R}-}_{\boldsymbol{g}\tau,\tilde{\mathbf{k}}_z^-}, \tag{2.68c}$$

and

$$A^{\mathscr{R}-}_{\boldsymbol{g}\tau,\mathbf{k}_z^+} = \sum_{\tilde{\boldsymbol{k}}_z^+} T^{++}_{\mathbf{k}_z^+\tilde{\boldsymbol{k}}_z^+} A^{\mathscr{L}-}_{\boldsymbol{g}\tau,\tilde{\boldsymbol{k}}_z^+} + \sum_{\tilde{\mathbf{k}}_z^-} T^{-+}_{\mathbf{k}_z^+\tilde{\mathbf{k}}_z^-} A^{\mathscr{R}-}_{\boldsymbol{g}\tau,\tilde{\mathbf{k}}_z^-}. \tag{2.68d}$$

one finally achieves four equations for the matrix elements of $T_{\mathscr{J}}$ in (2.65). These four matrix equations (2.68a)-(2.68d) can be written in supermatrix form as

$$\begin{pmatrix} A^{\mathscr{R}+}_{\mathbf{k}_z^+} & A^{\mathscr{R}-}_{\mathbf{k}_z^+} \\ A^{\mathscr{L}+}_{\boldsymbol{k}_z^-} & A^{\mathscr{L}-}_{\boldsymbol{k}_z^-} \end{pmatrix} = \begin{pmatrix} T^{++} & T^{+-} \\ T^{-+} & T^{--} \end{pmatrix} \begin{pmatrix} A^{\mathscr{L}+}_{\boldsymbol{k}_z^+} & A^{\mathscr{L}-}_{\boldsymbol{k}_z^+} \\ A^{\mathscr{R}+}_{\mathbf{k}_z^-} & A^{\mathscr{R}-}_{\mathbf{k}_z^-} \end{pmatrix}, \tag{2.69}$$

from which follows the BW-scattering matrix T. This formalism is not equivalent to a simple unitary transformation of $N_{\mathscr{J}}$ since each Bloch state contains plane waves traveling in both directions, or equivalently a single plane wave is composed of Bloch states traveling in both directions.

Note that in the above equations *all* PWs and *all* BWs (decreasing and increasing ones) are used. The dimension of $T^{\pm\pm}$ for each spin-projection is therefore $2N_g \times 2N_g$.

For tunneling only the traveling BWs have to be used. The respective numbers of these are denoted by $N_{\mathscr{L}\pm}$ and $N_{\mathscr{R}\pm}$, according to the leads and the flux along $\pm z$. The "reduced" scattering matrix $T_{\mathscr{I},t}$ which contains only traveling BWs is unitary ($T^{\dagger}_{\mathscr{I},t} T_{\mathscr{I},t} = 1$) if the BWs are normalized to unit current. The dimensions are $N_{\mathscr{L}+} \times N_{\mathscr{R}+}$ (T_t^{++}), $N_{\mathscr{L}+} \times N_{\mathscr{L}-}$ (T_t^{+-}), $N_{\mathscr{R}-} \times N_{\mathscr{R}+}$ (T_t^{-+}), and $N_{\mathscr{R}-} \times N_{\mathscr{L}-}$ (T_t^{--}).

As discussed before in (2.25) the conductance according to Landauer-Büttiker theory is calculated by an integration of transmission probabilities over the two-dimensional Brillouin zone. The individual transmission probability contributions are evaluated by

$$T(E,\boldsymbol{k}_{\parallel}) = \sum_{\boldsymbol{k}_z^+} \sum_{\mathbf{k}_z^+} \left| T^{++}_{t,\mathbf{k}_z^+ \boldsymbol{k}_z^+}(E,\boldsymbol{k}_{\parallel}) \right|^2 = \sum_{\boldsymbol{k}_z^-} \sum_{\mathbf{k}_z^-} \left| T^{--}_{t,\boldsymbol{k}_z^- \mathbf{k}_z^-}(E,\boldsymbol{k}_{\parallel}) \right|^2 . \tag{2.70}$$

The conductance channels are the incoming $(\boldsymbol{k}_z^+, \mathbf{k}_z^-)$ and outgoing $(\mathbf{k}_z^+, \boldsymbol{k}_z^-)$ traveling BWs with group velocities (along z) $v_{\boldsymbol{k}_z^+}$ and $v_{\mathbf{k}_z^+}$, respectively.

2.2.5 Conductance for disordered interfaces

2.2.5.1 The coherent potential approximation

The major object of this PhD-work is the extension of the LKKR code *omni* by a computational scheme to calculate the electronic transport through partially oxidized interface layers — which might occur in planar Fe/MgO/Fe magnetic tunnel junctions (MTJs) [21, 22] — in terms of disorder.

Due to the required lattice periodicity neither a structural nor a topological but a substitutional description of disorder (Fig. 2.10) is accessible within the LKKR method. With this kind of disorder a material is characterized by an underlying regular lattice where different atomic species may be randomly distributed over the lattice sites. That type of disorder, also referred as chemical disorder, is especially known from minerals and salt-like crystals. In the past, substitutional disorder established the basic description for electronic structure calculations [82, 83] of multi-component alloys where the properties of atom species or vacancies are incorporated by their averaged concentrations c.

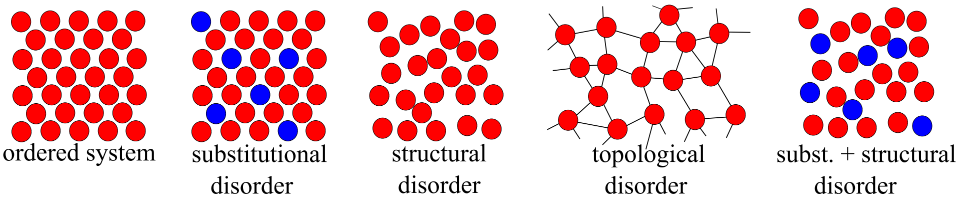

Figure 2.10: Schematics of different types of disorder with respect to an ordered two-dimensional lattice.

The first numerical tractable schemes have been the virtual crystal approximation (VCA) and the averaged t-matrix approximation (ATA). Within the VCA, known atomic site potentials are mixed to hybrid potentials $V_{VCA}(\boldsymbol{r}) = \sum_\alpha c_\alpha V_\alpha(\boldsymbol{r})$ which can be easily used in standard electronic structure methods.

A better incorporation of scattering properties is provided by the ATA which combines concentration weighted single-site t-matrices $t_{ATA}(\varepsilon) = \sum_\alpha c_\alpha t_\alpha(\varepsilon)$. For very diluted alloys the ATA provides relatively accurate results. With increasing concentration the inter-site scattering becomes more and more important, and the accuracy of the ATA decreases rapidly.

One of the most advanced computational schemes at present time is the coherent potential approximation (CPA) [69, 84–86] and its derivatives [87–89]. In this mean field theory the configurationally averaged properties of a disordered system are characterized by means of an effective medium which has to be determined self-consistently. The latter is constructed by demanding that the embedding of an isolated defect atom into the CPA medium should not lead on average to additional scattering (Fig. 2.11). In the single-site approximation (SSA) this leads to the CPA condition for the scattering path operator (2.34) of the effective medium

$\tau^{00}_{\mathrm{CPA}} = \sum_\alpha c_\alpha \tau^{00}_\alpha$ with $\sum_\alpha c_\alpha = 1$. The c_α and τ^{00}_α represent the individual concentrations and SPOs of the atom species α which are embedded as impurities at site 0.

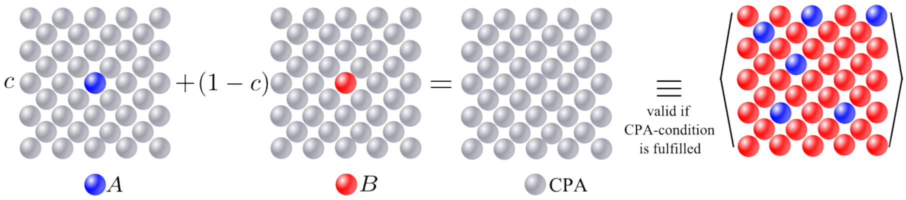

Figure 2.11: Conceptual scheme of the CPA-condition for a substitutionally disordered binary alloy $A_c B_{1-c}$ which is arranged on a two-dimensional lattice.

If the single-site scattering matrices for the atom species α and the k-projected structural Greens function $G(\boldsymbol{k})$ are known for a given energy ε, then a self-consistence cycle for the CPA SPO can be performed within an electronic structure calculation by the following procedure [32, 90].

1. Choose a starting value for the single-site scattering matrix t_{CPA} of the effective medium, for example (ATA): $t_{\mathrm{CPA}} = \sum_\alpha c_\alpha t_\alpha(\varepsilon)$.
2. Compute the effective SPO according to $\tau^{00}_{\mathrm{CPA}} = \dfrac{1}{\Omega} \displaystyle\int \left[t^{-1}_{\mathrm{CPA}} - G(\boldsymbol{k}) \right]^{-1} \mathrm{d}^3 k \,.$
3. Compute the defect-matrices via $D^{00}_\alpha = \left[1 + (t^{-1}_\alpha - t^{-1}_{CPA}) \tau^{00}_{CPA} \right]^{-1} .$
4. Compute the single impurity SPO's within the CPA medium, by $\tau^{00}_\alpha = D^{00}_\alpha \tau^{00}_{\mathrm{CPA}}$.
5. Compute new effective SPO within the SSA $\tilde{\tau}^{00}_{\mathrm{CPA}} = \sum_i c_\alpha \tau^{00}_\alpha$ and check whether $\tilde{\tau}^{00}_{\mathrm{CPA}} = \tau^{00}_{\mathrm{CPA}}$. If yes then stop, else compute based on $\tilde{\tau}^{00}_{\mathrm{CPA}} = D^{00}_{\tilde{t}} \tau^{00}_{\mathrm{CPA}}$ the new single-site scattering matrix $\tilde{t}_{\mathrm{CPA}} = \left\{ \left[\tau^{00}_{\mathrm{CPA}} \left(\tilde{\tau}^{00}_{\mathrm{CPA}} \right)^{-1} - 1 \right] \left(\tilde{\tau}^{00}_{\mathrm{CPA}} \right)^{-1} + t^{-1}_{\mathrm{CPA}} \right\}^{-1}$ and continue with calculating the SPO, step 2.

The CPA within the SSA does not allow to investigate fluctuations around the CPA average nor to account for the influence of atomic short-range order. This limitations can be overcome by a non-local formulation of the coherent potential approximation [91–93] or a locally self-consistent GF approach [94].

An electronic transport theory for bulk-like CPA materials was firstly discussed by Butler [95]. In this work it was pointed out that an important ingredient to maintain current conservation are the vertex corrections (VC). The latter incorporate that Bloch vectors $\boldsymbol{k}$—which are good quantum number in ordered systems—are in the presence of disorder not necessarily conserved anymore. The corresponding contributions are described by the VC.

It turned out that the latter have to be ignored in a CPA transport theory for layer-KKR systems, since the required lattice Fourier transformations are not practicable [96].

2.2.5.2 CPA versus supercell approach

Since a proper treatment of the CPA including the vertex corrections is not adequate to implement into the layer-KKR formalism a supercell approach that allows an equivalently accurate description of the electronic transport through a substitutionally disordered interface, will be discussed in the following.

The idea of this treatment was strongly motivated by the work of Butler and Velev [97, 98] who calculated the ballistic conductances through substitutionally disordered Fe-Cr(100) films. These were calculated on the one hand by means of a layer-adapted CPA and on the other hand with help of a supercell approach. All CPA conductances were calculated self-consistently (numerically time consuming [98]) but without vertex corrections.

Within the numerically much faster supercell method [98] it is possible to decompose the conductances into two contributions, those which stem from $\boldsymbol{k}_{\|}$-conserving (specular) and those who originate from $\boldsymbol{k}_{\|}$-non-conserving (diffuse) scattering processes,

$$\Gamma = \Gamma_{\text{spec}}(\boldsymbol{k}_{\|} \rightarrow \boldsymbol{k}_{\|}) + \Gamma_{\text{diff}}(\boldsymbol{k}_{\|} \rightarrow \boldsymbol{k}'_{\|}). \tag{2.71}$$

As can be seen from the transmission curves in Fig. 2.12 a comparison of the CPA method versus the SC approach reveals important insights:

1. The conductances calculated by means of the CPA without vertex corrections are in good agreement with the specular contributions achieved with the supercell approach.
2. The presence of disorder leads to additional diffusive conductance contributions, which show a broad maximum for a maximal degree of disorder at 50% defect concentration.
3. The thicker the disordered interface becomes, the more important the diffusive conductance contributions are.

The authors conclude that the difference in the total conductance between both methods stems directly from the absence of vertex corrections within the CPA approach. Without these corrections a proper treatment of the diffusive contributions is not possible in the CPA formalism. For this reason I developed and implemented a supercell approach within the layer-KKR formalism which will be described in the next section.

2.2.5.3 The supercell approach within the layer-KKR method

A layer supercell can, as illustrated in Fig. 2.13, be regarded as an in-plane extension of a layer unitcell. The corresponding two-dimensional supercell (SC) lattice vectors are integer multiples

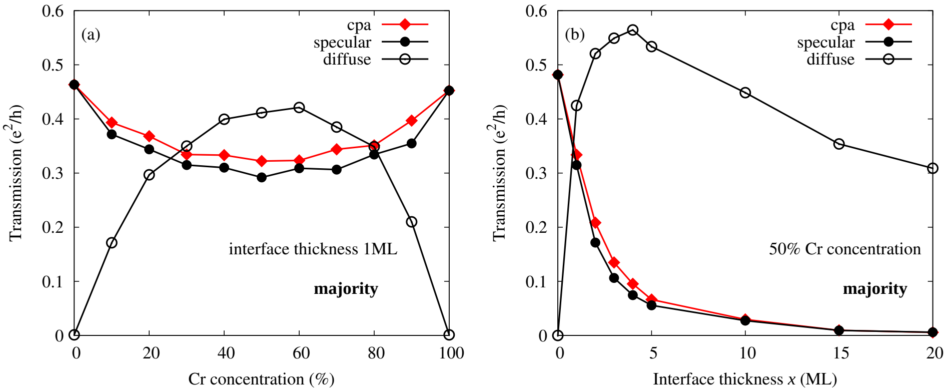

Figure 2.12: Comparison of the layer-adapted CPA and the supercell method for the computation of the electronic transport through substitutionally disordered Fe-Cr(100) interfaces (plotted data are extracted from [98]). Graph (a) shows the majority transmission as a function of the Cr defect concentration and a fixed interface thickness of 1ML. (b) displays the interface thickness dependence of the majority transmission with maximum diffusive contribution for a Cr concentration of 50%.

of their unitcell (UC) counterparts,

$$\begin{pmatrix} a_x^{\mathrm{SC}} \\ a_y^{\mathrm{SC}} \end{pmatrix} = \begin{pmatrix} N a_x^{\mathrm{UC}} \\ M a_y^{\mathrm{UC}} \end{pmatrix} . \tag{2.72}$$

The corresponding first UC Brillouin zone is larger by a factor $N \times M$ in comparison to the SC one. As a direct consequence, the points associated with the SC reciprocal mesh form with

$$\boldsymbol{k}_{\|}^{\mathrm{UC}} + \begin{pmatrix} m_x g_x^{\mathrm{UC}} \\ m_y g_y^{\mathrm{UC}} \end{pmatrix} = \boldsymbol{k}_{\|}^{\mathrm{UC}} + \begin{pmatrix} m_x N g_x^{\mathrm{SC}} \\ m_y M g_y^{\mathrm{SC}} \end{pmatrix} \subset \boldsymbol{k}_{\|}^{\mathrm{SC}} + \begin{pmatrix} m'_x g_x^{\mathrm{SC}} \\ m'_y g_y^{\mathrm{SC}} \end{pmatrix}, \quad m, m' \in \mathbb{N} \tag{2.73}$$

a denser mesh of points than those of the UC mesh. Different $\boldsymbol{k}_{\|}^{\mathrm{UC}}$-vectors within the UC 1.BZ are equivalent to the $\boldsymbol{k}_{\|}^{\mathrm{SC}}$-vectors that lie, with respect to a repeated zone scheme, not only within the SC 1.BZ but also in the neighboring SC BZs (see Fig. 2.13).

All down-folded vectors $\overline{\boldsymbol{k}}_{\|}^{\mathrm{UC}}$ (represented as stars in Fig. 2.13) can be found by shifts of the single $\boldsymbol{k}_{\|}^{\mathrm{SC}}$ by integer multiples of the reciprocal SC lattice vectors $\boldsymbol{g}^{\mathrm{SC}}$. The subset of these umklapp vectors $\{\overline{\boldsymbol{g}}^{\mathrm{SC}}\} \subset \{\boldsymbol{g}^{\mathrm{SC}}\}$ is characterized by

$$\overline{\boldsymbol{g}}^{\mathrm{SC}} \in \{\overline{\boldsymbol{k}}_{\|}^{\mathrm{UC}} = \boldsymbol{k}_{\|}^{\mathrm{SC}} + \overline{\boldsymbol{g}}^{\mathrm{SC}}\}. \tag{2.74a}$$

With respect to (2.73) one can see further that the subset of umklapp vectors $\{\overline{\boldsymbol{g}}^{\mathrm{SC}}\}$ just repre-

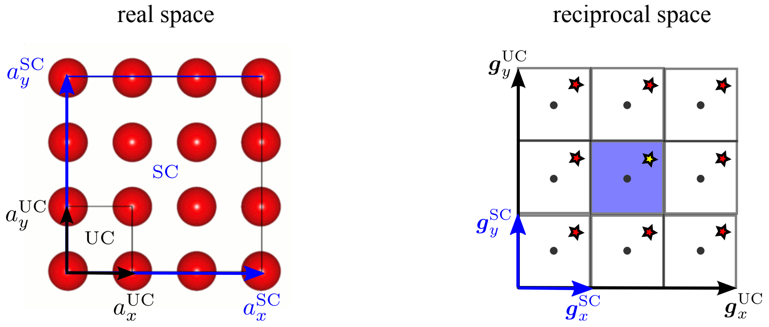
real space

reciprocal space

Figure 2.13: Schematic comparison of a 2-dimensional primitive unitcell (UC) versus a supercell (SC) in real space, and the corresponding Brillouin zones in reciprocal space. The SC is constructed for example here by a 3 × 3 repetition of the UC. The stars illustrate the present down-folding processes of $\boldsymbol{k}_{\parallel}^{\mathrm{UC}}$-vectors. Different $\boldsymbol{k}_{\parallel}^{\mathrm{UC}}$-points within the UC 1.BZ (red and yellow stars) are folded down into a single $\boldsymbol{k}_{\parallel}^{\mathrm{SC}}$-point of the SC 1.BZ (yellow star). All $\overline{\boldsymbol{k}}_{\parallel}^{\mathrm{UC}}$-vectors correspond, with respect to a repeated zone scheme, to equivalent points in neighbored BZs on the more dense SC mesh and can therefore be found by shifts of $\boldsymbol{k}_{\parallel}^{\mathrm{SC}}$ about multiples of the umklapp vectors $\{\overline{\boldsymbol{g}}^{\mathrm{SC}}\} \subset \{\boldsymbol{g}^{\mathrm{SC}}\}$.

sents all those $N \times M$ reciprocal lattice vectors $\boldsymbol{g}^{\mathrm{SC}}$ that obey the relation

$$\begin{pmatrix} m'_x g_x^{\mathrm{SC}} \\ m'_y g_y^{\mathrm{SC}} \end{pmatrix} \leq \begin{pmatrix} g_x^{\mathrm{UC}} \\ g_y^{\mathrm{UC}} \end{pmatrix} \qquad \text{with} \quad 0 \leq m'_x \leq N, \quad \text{and} \quad 0 \leq m'_y \leq M. \tag{2.74b}$$

The PW fields in the UC (SC) frame are characterized, according to (2.47), by sets of reciprocal lattice vectors. The respective sets of in-plane components are shown in Fig. 2.14, and read

$$\boldsymbol{q}^{\mathrm{UC}} = \{\boldsymbol{k}_{\parallel}^{\mathrm{UC}} + \boldsymbol{g}^{\mathrm{UC}}\}, \tag{2.75a}$$

$$\boldsymbol{q}^{\mathrm{SC}} = \{\boldsymbol{k}_{\parallel}^{\mathrm{SC}} + \boldsymbol{g}^{\mathrm{SC}}\}. \tag{2.75b}$$

Due to the denser SC reciprocal mesh (2.73), one finds that the number of elements in $\boldsymbol{q}^{\mathrm{SC}}$ and therefore the number of PWs within the SC basis, is about $N \times M$ larger in comparison to the UC case.

In the following will be all those $\boldsymbol{g}^{\mathrm{UC}}$ vectors in (2.75a) which belong on the one hand to a certain $\overline{\boldsymbol{k}}_{\parallel}^{\mathrm{UC}}$ in (2.74a), and that are on the other hand characterized by the umklapp-vector $\overline{\boldsymbol{g}}^{\mathrm{SC}} = 0$, defined through the set $\{\boldsymbol{g}_0^{\mathrm{UC}}\}$. With help of the latter one can express $\boldsymbol{q}^{\mathrm{SC}}$ in (2.75b) alternatively as a set union,

$$\boldsymbol{q}^{\mathrm{SC}} = \dot{\bigcup}_{\forall \overline{\boldsymbol{g}}^{\mathrm{SC}}} \{\boldsymbol{k}_{\parallel}^{\mathrm{SC}} + \overline{\boldsymbol{g}}^{\mathrm{SC}} + \boldsymbol{g}_0^{\mathrm{UC}}\} = \dot{\bigcup}_{\forall \overline{\boldsymbol{g}}^{\mathrm{SC}}} \{\overline{\boldsymbol{k}}_{\parallel}^{\mathrm{UC}} + \boldsymbol{g}_0^{\mathrm{UC}}\}, \tag{2.76}$$

of disjoint subsets $\boldsymbol{q}^{\mathrm{UC}}$ which are characterized by $\overline{\boldsymbol{k}}_{\parallel}^{\mathrm{UC}}$ that are unambiguously defined via

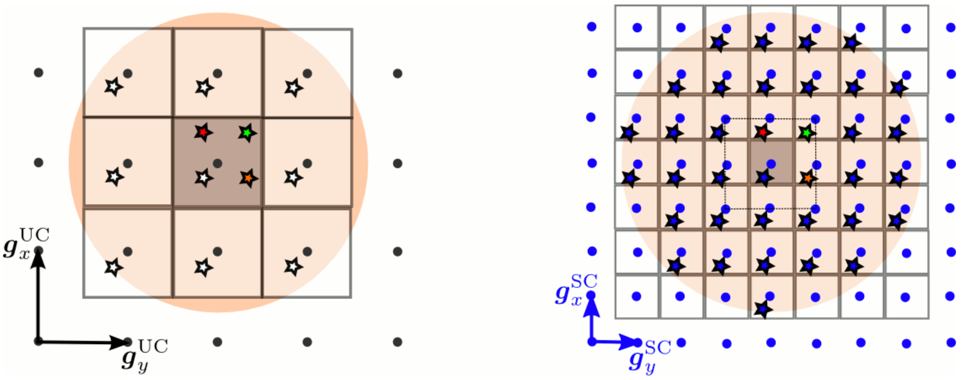
$\boldsymbol{g}_x^{\mathrm{UC}}$
$\boldsymbol{g}_y^{\mathrm{UC}}$
$\boldsymbol{g}_x^{\mathrm{SC}}$
$\boldsymbol{g}_y^{\mathrm{SC}}$

Figure 2.14: Schematic representation of reciprocal lattices for layers based on translations of a 2-dimensional primitive unitcell (UC, left-hand side) or a supercell (SC, right-hand side) constructed for example here by a 2×2 repetition of the UC. The transparent squares correspond to the 1st and neighbored Brillouin zones (1.BZs ≡ gray areas). The white (blue) stars represent sets of reciprocal lattice vectors $\boldsymbol{q}^{\mathrm{UC}}=\{\boldsymbol{k}_\parallel^{\mathrm{UC}}+\boldsymbol{g}^{\mathrm{UC}}\}$ $\left(\boldsymbol{q}^{\mathrm{SC}}=\{\boldsymbol{k}_\parallel^{\mathrm{SC}}+\boldsymbol{g}^{\mathrm{SC}}\}\right)$ which lie within a given energy radius $|\boldsymbol{q}|<\sqrt{2E}$, emphasized by the orange circle, and that are used for the construction of PW fields. The red, green and orange stars mark a subset $\overline{\boldsymbol{q}}^{\mathrm{SC}}\subseteq\boldsymbol{q}^{\mathrm{SC}}$ of vectors which belong in the SC frame to equivalent $\boldsymbol{k}_\parallel^{\mathrm{SC}}$-points in neighbored BZs but represent different $\overline{\boldsymbol{k}}_\parallel^{\mathrm{UC}}$-points within the UC 1.BZ. Considering the different $\overline{\boldsymbol{k}}_\parallel^{\mathrm{UC}}$-points and the $\boldsymbol{k}_\parallel^{\mathrm{SC}}$-vector within the SC 1.BZ, then the subset $\overline{\boldsymbol{q}}^{\mathrm{SC}}$ is characterized by all $\overline{\boldsymbol{g}}^{\mathrm{SC}}\in\{\overline{\boldsymbol{k}}_\parallel^{\mathrm{UC}}=\boldsymbol{k}_\parallel^{\mathrm{SC}}+\overline{\boldsymbol{g}}^{\mathrm{SC}}\}$.

umklapp-vectors in (2.74a).

As illustrated in Fig. 2.15, the mapping is, due to missing points at the boundary, not complete. This problem can be solved by choosing the energy $E_{\mathrm{max}}\geq\frac{1}{2}(\boldsymbol{k}_\parallel+\boldsymbol{g})^2$ large enough so that PWs which belong to missing $\boldsymbol{g}$-vectors decay rapidly and can be safely ignored.

A direct consequence of the decomposition in (2.76) is the possibility to superimpose incoming SC-PW fields (2.46),

$$\begin{aligned}\Psi_{\mathrm{inc}}^{\mathrm{SC}}(\boldsymbol{r},\boldsymbol{k}_\parallel^{\mathrm{SC}})\chi^\tau &= \sum_{\boldsymbol{g}^{\mathrm{SC}}}\left[u_{\boldsymbol{g}^{\mathrm{SC}}\tau}^{+}\exp\left(i\boldsymbol{k}_{\boldsymbol{g}^{\mathrm{SC}}\tau}^{+}\cdot\boldsymbol{r}\right)+u_{\boldsymbol{g}^{\mathrm{SC}}\tau}^{-}\exp\left(i\boldsymbol{k}_{\boldsymbol{g}^{\mathrm{SC}}\tau}^{-}\cdot\boldsymbol{r}\right)\right]\chi^\tau, &\text{(2.77a)}\\ &= \sum_{\overline{\boldsymbol{g}}^{\mathrm{SC}}}\;\sum_{\boldsymbol{g}'=\boldsymbol{g}_0^{\mathrm{UC}}+\overline{\boldsymbol{g}}^{\mathrm{SC}}}\left[u_{\boldsymbol{g}'\tau}^{+}\exp\left(i\boldsymbol{k}_{\boldsymbol{g}'\tau}^{+}\cdot\boldsymbol{r}\right)+u_{\boldsymbol{g}'\tau}^{-}\exp\left(i\boldsymbol{k}_{\boldsymbol{g}'\tau}^{-}\cdot\boldsymbol{r}\right)\right]\chi^\tau,\\ &= \sum_{\overline{\boldsymbol{g}}^{\mathrm{SC}}}\Psi_{\mathrm{inc}}^{\mathrm{SC}}(\boldsymbol{r},\underbrace{\boldsymbol{k}_\parallel^{\mathrm{SC}}+\overline{\boldsymbol{g}}^{\mathrm{SC}}}_{=\overline{\boldsymbol{k}}_\parallel^{\mathrm{UC}}})\chi^\tau, &\text{(2.77b)}\end{aligned}$$

by means of PWs calculated in UC basis sets at different $\overline{\boldsymbol{k}}_\parallel^{\mathrm{UC}}$-points. A similar decomposition can be performed for all present outgoing SC-PW fields.

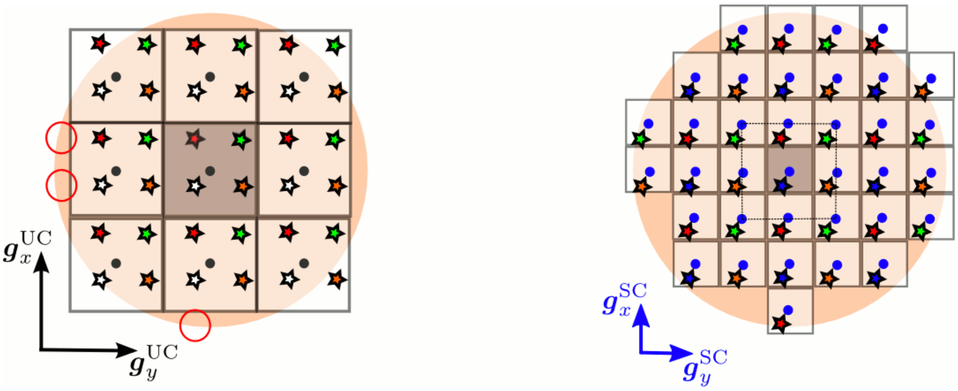
$\boldsymbol{g}_x^{\mathrm{UC}}$
$\boldsymbol{g}_y^{\mathrm{UC}}$
$\boldsymbol{g}_x^{\mathrm{SC}}$
$\boldsymbol{g}_y^{\mathrm{SC}}$

Figure 2.15: The same schematic representation of reciprocal lattices and Brillouin zones as shown in Fig. 2.14. The graphs illustrate a construction of the set of reciprocal lattice vectors $\boldsymbol{q}^{\mathrm{SC}}$ by shifting the set of $\boldsymbol{q}^{\mathrm{UC}}$ about all present $\overline{\boldsymbol{g}}^{\mathrm{SC}}$. The mapping $\boldsymbol{q}^{\mathrm{SC}} = \{\boldsymbol{q}^{\mathrm{UC}} + \overline{\boldsymbol{g}}^{\mathrm{SC}}\}$ is, due to missing points (marked by red circles) at the boundary, not complete.

The corresponding layer scattering matrices

$$M^{\mathrm{SC},\pm\pm} = \begin{pmatrix} M^{\pm\pm}(\overline{\boldsymbol{k}}^{\mathrm{UC}}_{\parallel 1} \to \overline{\boldsymbol{k}}^{\mathrm{UC}}_{\parallel 1}) & \cdots & M^{\pm\pm}(\overline{\boldsymbol{k}}^{\mathrm{UC}}_{\parallel 1} \to \overline{\boldsymbol{k}}^{\mathrm{UC}}_{\parallel N\times M}) \\ \vdots & \ddots & \vdots \\ M^{\pm\pm}(\overline{\boldsymbol{k}}^{\mathrm{UC}}_{\parallel N\times M} \to \overline{\boldsymbol{k}}^{\mathrm{UC}}_{\parallel 1}) & \cdots & M^{\pm\pm}(\overline{\boldsymbol{k}}^{\mathrm{UC}}_{\parallel N\times M} \to \overline{\boldsymbol{k}}^{\mathrm{UC}}_{\parallel N\times M}) \end{pmatrix} \tag{2.78}$$

have block matrix structure. Each matrix block $M^{\pm\pm}(\overline{\boldsymbol{k}}^{\mathrm{UC}}_{\parallel} \to \overline{\boldsymbol{k}}'^{\mathrm{UC}}_{\parallel})$ describes accordingly to (2.48) and (2.77) the scattering of incoming into outgoing PWs which are characterized by either identical or different umklapp vectors (2.74a). This mapping allows a direct classification into specular (diagonal block matrices with $\overline{\boldsymbol{k}}^{\mathrm{UC}}_{\parallel i} \to \overline{\boldsymbol{k}}^{\mathrm{UC}}_{\parallel i}$) and diffuse (off-diagonal block matrices with $\overline{\boldsymbol{k}}^{\mathrm{UC}}_{\parallel i} \to \overline{\boldsymbol{k}}^{\mathrm{UC}}_{\parallel j\neq i}$) scattering processes with respect to the $\overline{\boldsymbol{k}}^{\mathrm{UC}}_{\parallel}$ conservation. The number of diffuse scattering channels is equal to the number of umklapp vectors and so directly related to the size of the layer supercell. The larger the SC the more diffusive scattering contributions can be accounted for.

The electronic transport can be principally calculated as discussed for the Bloch-wave scattering approach in section 2.2.4.2, but with the major drawback that the conductances would be completely specular with respect to the vectors within the SCs 1.BZs. Scattering processes with regard to different $\overline{\boldsymbol{k}}^{\mathrm{UC}}_{\parallel}$ points would be hidden and therefore would not be accessible.

One can solve this problem based on the knowledge that scattering processes caused by equally composed layers have to be absolutely identical in both frames. This situation is always present within the leads $\mathscr{L}$ and $\mathscr{R}$ where SC layers are constructed via $N \times M$ repetitions of simple layer UCs. Since all scattering processes in the UC frame are specular with respect to $\boldsymbol{k}_{\parallel}$, only the diagonal elements of the SC layer scattering matrices $M^{\mathrm{SC},\pm\pm}$ in (2.78) are nonzero. Each block element represents a specular scattering matrix $M^{\pm\pm}(\boldsymbol{k}^{\mathrm{SC}}_{\parallel} + \overline{\boldsymbol{g}}^{\mathrm{SC}} \to \boldsymbol{k}^{\mathrm{SC}}_{\parallel} + \overline{\boldsymbol{g}}^{\mathrm{SC}}) = M^{\pm\pm}(\overline{\boldsymbol{k}}^{\mathrm{UC}}_{\parallel}$

$\rightarrow \overline{\boldsymbol{k}}_{\parallel}^{\mathrm{UC}}$) which is identical to that one calculated at the corresponding $\boldsymbol{k}_{\parallel}$-point within the UC frame (2.50).

Further, the Bloch eigenvalue problem (2.58) formulated within the SC frame,

$$\begin{pmatrix} Q^{\mathrm{SC},++} & Q^{\mathrm{SC},+-} \\ Q^{\mathrm{SC},-+} & Q^{\mathrm{SC},--} \end{pmatrix} \begin{pmatrix} \boldsymbol{u}^{\mathrm{SC},+} \\ \boldsymbol{v}^{\mathrm{SC},-} \end{pmatrix} = \lambda \begin{pmatrix} \boldsymbol{u}^{\mathrm{SC},+} \\ \boldsymbol{v}^{\mathrm{SC},-} \end{pmatrix}, \tag{2.79}$$

leads to $4N_{\boldsymbol{g}}NM$ eigenpairs. Since the Bloch states **have to be identical** in both frames, one can find a bijective mapping to the respective $4N_{\boldsymbol{g}}$ eigensolutions that are found in $N \times M$ UC calculations for the corresponding $\boldsymbol{k}_{\parallel}$-points

$$\left\{\psi^{\mathrm{SC}}\left(\boldsymbol{k}_{\parallel}^{\mathrm{SC}}\right)\right\}_{(4N_{\boldsymbol{g}}NM)} = \dot{\bigcup}_{\forall \overline{\boldsymbol{g}}^{\mathrm{SC}}} \left\{\psi^{\mathrm{UC}}\left(\overline{\boldsymbol{k}}_{\parallel}^{\mathrm{UC}}\right)\right\}_{(4N_{\boldsymbol{g}})}. \tag{2.80}$$

This decomposition allows one to express and label each SC Bloch state in terms of a BW (2.62) that is calculated at $\overline{\boldsymbol{k}}_{\parallel}^{\mathrm{UC}}$ within the UC frame

$$\begin{aligned} \psi^{\mathrm{SC}\tau}_{k_z^{\pm}(\overline{\boldsymbol{g}}^{\mathrm{SC}})} \chi^{\tau} &= \sum_{\boldsymbol{g}'} \left[u^{+}_{k_z^{\pm},\boldsymbol{g}'\tau} \exp(i\boldsymbol{k}^{+}_{\boldsymbol{g}'\tau} \cdot \boldsymbol{r}) + v^{-}_{k_z^{\pm},\boldsymbol{g}'\tau} \exp(i\boldsymbol{k}^{-}_{\boldsymbol{g}'\tau} \cdot \boldsymbol{r}) \right] \chi^{\tau}, & \text{(2.81a)} \\ &= \psi^{\mathrm{UC}\tau}_{k_z^{\pm}} \left(\boldsymbol{k}_{\parallel}^{\mathrm{SC}} + \overline{\boldsymbol{g}}^{\mathrm{SC}} \right) \chi^{\tau} \quad \left(\equiv \psi^{\mathrm{UC}\tau}_{k_z^{\pm}} \left(\overline{\boldsymbol{k}}_{\parallel}^{\mathrm{UC}} \right) \chi^{\tau} \right). & \text{(2.81b)} \end{aligned}$$

The associated PWs basis sets (2.47) are, through

$$\boldsymbol{k}^{\pm}_{\boldsymbol{g}'} = \begin{pmatrix} \overline{\boldsymbol{k}}_{\parallel}^{\mathrm{UC}} + \boldsymbol{g}' \\ \pm\sqrt{2E - \left(\overline{\boldsymbol{k}}_{\parallel}^{\mathrm{UC}} + \boldsymbol{g}'\right)^2} \end{pmatrix} \tag{2.82}$$

and $\boldsymbol{g}' = \boldsymbol{g}_0^{\mathrm{UC}} + \overline{\boldsymbol{g}}^{\mathrm{SC}}$, uniquely defined by means of the specific umklapp vectors.

Another advantage of the partition procedure is the possibility of replacing the numerically very expensive eigenvalue problem (2.79) through $N \times M$ more quickly solvable and less memory demanding ones (2.58), dealing thereby with sizeably smaller matrices.

The scattering situation is changed if layer SCs cannot be constructed by repeated translations of simple layer UCs. That breaking of in-plane UC periodicity can be caused for instance through the presence of defects and leads to additional scattering contributions from the off-diagonal matrix blocks $M^{\pm\pm}(\overline{\boldsymbol{k}}_{\parallel}^{\mathrm{UC}} \rightarrow \overline{\boldsymbol{k}}'^{\mathrm{UC}}_{\parallel})$ in (2.78).

The basic idea of the supercell approach for the description of specular and diffusive electronic transport can be summarized as follows. One separates again the SC system into three principle regions $\mathscr{L}^{\mathrm{SC}}$, $\mathscr{I}^{\mathrm{SC}}$, and $\mathscr{R}^{\mathrm{SC}}$. Disordered SC layers that exhibit broken UC in-plane periodicity are comprised within the interface region $\mathscr{I}^{\mathrm{SC}}$ whose scattering properties are described by the matrices $N^{\mathrm{SC},\pm\pm}$. These are, in contrary to the matrices $M^{\mathrm{SC},\pm\pm}$ in $\mathscr{L}^{\mathrm{SC}}$ and $\mathscr{R}^{\mathrm{SC}}$, fully occupied super block matrices and describe due to the presence of defects both specular (diagonal blocks) and diffusive (off-diagonal blocks) scattering processes.

Analogously to the discussion of the Bloch-wave scattering approach in section 2.2.4.2 one has to now determine expressions of the interface scattering matrices by means of the present Bloch states within the leads $\mathscr{L}^{\mathrm{SC}}$ and $\mathscr{R}^{\mathrm{SC}}$. The latter may differ due to distinct materials. With regard to the UC frame separation in (2.81b) BWs can be distinguished on the one hand by their eigenvalues and on the other hand by their corresponding umklapp vectors $\boldsymbol{k}_z^{\pm}(\overline{\boldsymbol{g}}^{\mathrm{SC}})$ ($\mathscr{L}^{\mathrm{SC}}$: italic) and $\boldsymbol{\mathsf{k}}_z^{\pm}(\overline{\boldsymbol{g}}^{\mathrm{SC}})$ ($\mathscr{R}^{\mathrm{SC}}$: sans-serif), respectively. The conditional matrix equation for the scattering matrix T can be analogously found and solved as discussed for (2.69)

$$\begin{pmatrix} A^{\mathscr{R}+}_{\boldsymbol{\mathsf{k}}_z^{+}(\overline{\boldsymbol{g}}^{\mathrm{SC}})} & A^{\mathscr{R}-}_{\boldsymbol{\mathsf{k}}_z^{+}(\overline{\boldsymbol{g}}^{\mathrm{SC}})} \\ A^{\mathscr{L}+}_{\boldsymbol{k}_z^{-}(\overline{\boldsymbol{g}}^{\mathrm{SC}})} & A^{\mathscr{L}-}_{\boldsymbol{k}_z^{-}(\overline{\boldsymbol{g}}^{\mathrm{SC}})} \end{pmatrix} = \begin{pmatrix} T^{++} & T^{+-} \\ T^{-+} & T^{--} \end{pmatrix} \begin{pmatrix} A^{\mathscr{L}+}_{\boldsymbol{k}_z^{+}(\overline{\boldsymbol{g}}^{\mathrm{SC}})} & A^{\mathscr{L}-}_{\boldsymbol{k}_z^{+}(\overline{\boldsymbol{g}}^{\mathrm{SC}})} \\ A^{\mathscr{R}+}_{\boldsymbol{\mathsf{k}}_z^{-}(\overline{\boldsymbol{g}}^{\mathrm{SC}})} & A^{\mathscr{R}-}_{\boldsymbol{\mathsf{k}}_z^{-}(\overline{\boldsymbol{g}}^{\mathrm{SC}})} \end{pmatrix}. \tag{2.83}$$

Transmitted Bloch waves incident from the left-hand (right-hand) side of the interface barrier are described by the coefficients $T^{++}_{\boldsymbol{\mathsf{k}}_z^{+}(\overline{\boldsymbol{g}}^{\mathrm{SC}})\tilde{\boldsymbol{k}}_z^{+}(\overline{\boldsymbol{g}}'^{\mathrm{SC}})}$ $\left(T^{--}_{\boldsymbol{k}_z^{-}(\overline{\boldsymbol{g}}^{\mathrm{SC}})\tilde{\boldsymbol{\mathsf{k}}}_z^{-}(\overline{\boldsymbol{g}}'^{\mathrm{SC}})}\right)$. In order to find a decomposition of the conductances into specular and diffusive parts with respect to the $\overline{\boldsymbol{k}}_{\parallel}^{\mathrm{UC}}$ conservation one has to separate the transmission probabilities into those contributions which connect propagating Bloch states with equal and distinct umklapp vectors

$$T_{\mathrm{spec}}(E,\boldsymbol{k}_{\parallel}^{\mathrm{SC}}) = \sum_{\boldsymbol{k}_z^{+}(\overline{\boldsymbol{g}}^{\mathrm{SC}})} \sum_{\boldsymbol{\mathsf{k}}_z^{+}(\overline{\boldsymbol{g}}^{\mathrm{SC}})} \left| T^{++}_{t,\boldsymbol{\mathsf{k}}_z^{+}(\overline{\boldsymbol{g}}^{\mathrm{SC}})\boldsymbol{k}_z^{+}(\overline{\boldsymbol{g}}^{\mathrm{SC}})}(E,\boldsymbol{k}_{\parallel}^{\mathrm{SC}}) \right|^2, \tag{2.84a}$$

$$= \sum_{\boldsymbol{\mathsf{k}}_z^{-}(\overline{\boldsymbol{g}}^{\mathrm{SC}})} \sum_{\boldsymbol{k}_z^{-}(\overline{\boldsymbol{g}}^{\mathrm{SC}})} \left| T^{--}_{t,\boldsymbol{k}_z^{-}(\overline{\boldsymbol{g}}^{\mathrm{SC}})\boldsymbol{\mathsf{k}}_z^{-}(\overline{\boldsymbol{g}}^{\mathrm{SC}})}(E,\boldsymbol{k}_{\parallel}^{\mathrm{SC}}) \right|^2, \tag{2.84b}$$

$$T_{\mathrm{diff}}(E,\boldsymbol{k}_{\parallel}^{\mathrm{SC}}) = \sum_{\boldsymbol{k}_z^{+}(\overline{\boldsymbol{g}}^{\mathrm{SC}})} \sum_{\boldsymbol{\mathsf{k}}_z^{+}(\overline{\boldsymbol{g}}'^{\mathrm{SC}})} \left| T^{++}_{t,\boldsymbol{\mathsf{k}}_z^{+}(\overline{\boldsymbol{g}}^{\mathrm{SC}})\boldsymbol{k}_z^{+}(\overline{\boldsymbol{g}}'^{\mathrm{SC}})}(E,\boldsymbol{k}_{\parallel}^{\mathrm{SC}}) \right|^2, \tag{2.84c}$$

$$= \sum_{\boldsymbol{\mathsf{k}}_z^{-}(\overline{\boldsymbol{g}}^{\mathrm{SC}})} \sum_{\boldsymbol{k}_z^{-}(\overline{\boldsymbol{g}}'^{\mathrm{SC}})} \left| T^{--}_{t,\boldsymbol{k}_z^{-}(\overline{\boldsymbol{g}}^{\mathrm{SC}})\boldsymbol{\mathsf{k}}_z^{-}(\overline{\boldsymbol{g}}'^{\mathrm{SC}})}(E,\boldsymbol{k}_{\parallel}^{\mathrm{SC}}) \right|^2. \tag{2.84d}$$

Eventually, the conductance then reads

$$\Gamma(E) = \frac{e^2}{h} \sum_{\boldsymbol{k}_{\parallel}^{\mathrm{SC}}} T_{\mathrm{spec}}(E,\boldsymbol{k}_{\parallel}^{\mathrm{SC}}) + \frac{e^2}{h} \sum_{\boldsymbol{k}_{\parallel}^{\mathrm{SC}}} T_{\mathrm{diff}}(E,\boldsymbol{k}_{\parallel}^{\mathrm{SC}}), \tag{2.85a}$$

$$= \Gamma_{\mathrm{spec}}(E) + \Gamma_{\mathrm{diff}}(E). \tag{2.85b}$$

Chapter 3

Selected Results and Discussion

In the following I give an overview about the research activities of my PhD work. A common aspect of the presented first-principles investigations is the question how the spin-dependent electronic transport in planar magnetic tunnel junctions (MTJs) is influenced by structural and magnetic changes of the interface structures.

In particular, I focused on the effect of partially oxidized Fe interface layers in Fe/MgO/Fe MTJs. Their influence on the tunnel magnetoresistance ratio as a function for different oxygen concentrations was modeled by means of substitutional disorder (►**1**).

Furthermore, I studied the specific changes of the conductances and TMR ratios with the thickness of inserted magnetic interlayers. The thickness dependencies were regarded for ultrathin films of layer-wise anti-ferromagnetic Mn (►**2**) and Cr (►**3**,►**4**) as well as for ferromagnetic Co (►**3**,►**4**).

The discussion of these results is given by means of the selected articles:

► **1 (see P51ff)** P. Bose, A. Ernst, I. Mertig and J. Henk: *"Large reduction of the magnetoresistance in Fe/MgO/Fe tunnel junctions due to small oxygen concentrations at a single FeO interface layer: A first-principles study"* Physical Review B **78**, 092403 (2008),

► **2 (see P57ff)** P. Bose, J. Henk and I. Mertig: *"Oscillatory tunneling magnetoresistance caused by antiferromagnetic Mn layers"* Physical Review B **75**, 100402(R) (2007),

► **3 (see P62ff)** P. Bose, P. Zahn, J. Henk and I. Mertig: *"Tailoring TMR Ratios by Ultrathin Magnetic Interlayers: A First-principles Investigation of Fe/MgO/Fe"* in Novel Materials and Devices for Spintronics, edited by O.G. Heinonen, S. Sanvito, V.A. Dediu, N. Rizzo (Mater. Res. Soc. Symp. Proc. Volume **1183**, Warrendale, PA, 2009), 1183-FF07-02,

► **4 (see P70ff)** P. Bose, P. Zahn, J. Henk and I. Mertig: *"Tailoring TMR Ratios by Ultrathin Cr*

and Co Interlayers: A First-principles Investigation of Fe/MgO/Fe”
submitted to Physical Review B, preprint at http://arxiv.org/abs/1001.2322 .

In front of each article there will be a short introduction to the respective project as well as a brief recapitulation of the main results. Specific details of each investigated structure are presented with the help of schematic illustrations.

3.1 Fe(001)/FeO/MgO/Fe(001)

One means to close the gap between theoretical predicted [15, 16] and experimental measured [11, 12] TMR ratios in Fe/MgO/Fe MTJs was found by taking into account the formation of a partially oxidized FeO_c interface layer in real samples [20]. The geometric structure in my investigations, which is shown in Fig. 3.1, uses atomic positions which have been determined by x-ray diffraction analysis [22]. To study the specific effects of different oxygen concentrations on the electronic transport, one has to include a proper description of the substoichiometric FeO_c layers. Usually these are modeled by introducing substitutional disorder into the system.

The intention of my work was to overcome the disadvantages which appeared in previously reported first-principles investigations. The latter used either the coherent potential approximation without vertex corrections [23] (see P39ff) or incoherently superimposed conductances for different MTJs [24]. These approaches lack either current conservation or coherency [25], both of them are treated properly in the above presented supercell approach (see Fig. 3.2 and P41ff).

It is found that the tunnel magnetoresistance reacts very sensitively on the presence of substoichiometric FeO_c layers. Already small oxygen concentration (less than 5%) reduce the TMR ratios considerably about 80% - in comparison to those obtained in ideal Fe/MgO/Fe MTJs.

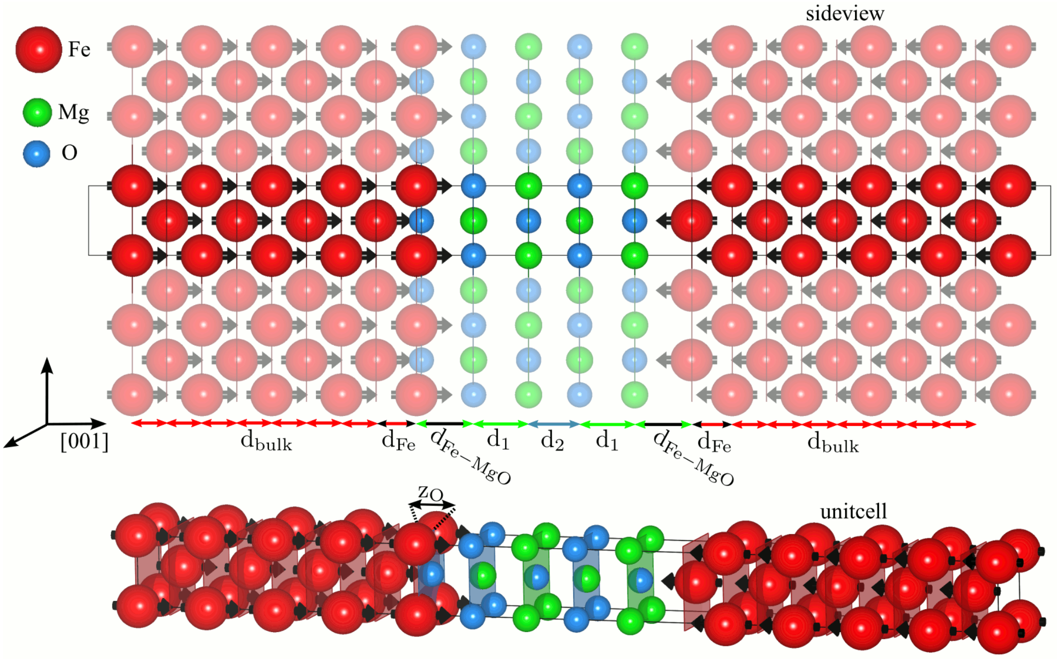

Figure 3.1: Schematic of the structural setup of an Fe(001)/FeO/4MgO/Fe(001) magnetic tunnel junction (MTJ) with layer distances $d_{bulk} = 1.43Å$, $d_{Fe} = 1.66Å$, $d_{Fe-MgO} = 2.35Å$, $d_1 = 2.26Å$, $d_2 = 2.10Å$, and $z_O = 0.20Å$. The latter characterizes a shift between the Fe and O planes within the FeO layer at the interface. Black arrows at the Fe sites emphasize the local magnetic directions. The MTJ is shown here for an anti-parallel magnetic configuration.

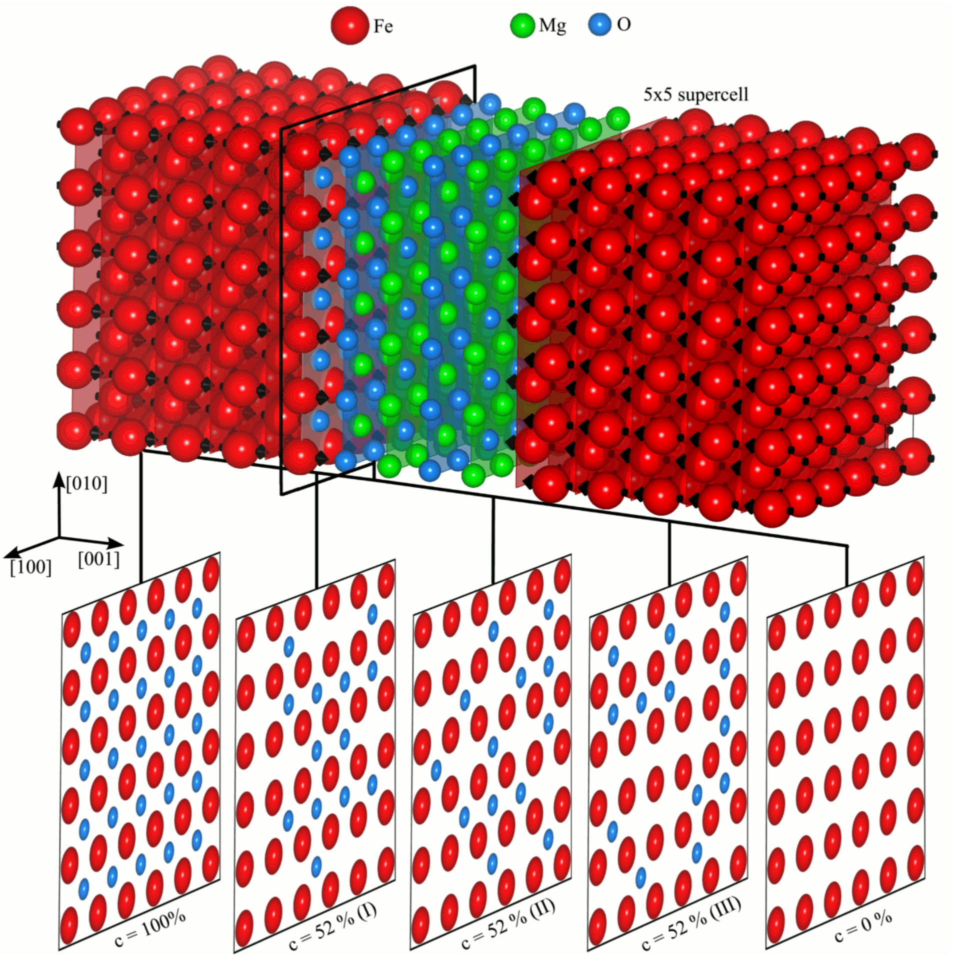

Figure 3.2: Pictorial representation of a partially oxidized Fe interface layer within an Fe(001)/FeO$_c$/4MgO /Fe(001) magnetic tunnel junction (MTJ). The partial oxygen occupancy is modeled by means of substitutional disorder within a layer supercell (SC) structure. The latter is constructed here by means of a 5 × 5 repetition of the layer unit cell structure in Fig. 3.1. Consequently, there are 25 O sites within the FeO$_c$ layer which could either be occupied or unoccupied. A variation of the oxygen concentration c can be performed from $c = 0\%$ (0 oxygen atoms) to $c = 100\%$ (25 oxygen atoms) in 4% steps ($^1/_{25}$ steps). The limiting cases $c = 0\%$ and $c = 100\%$ as well as three topologically different disorder configurations for $c = 52\%$ exemplify these variations.

PHYSICAL REVIEW B **78**, 092403 (2008)

Large reduction of the magnetoresistance in Fe/MgO/Fe tunnel junctions due to small oxygen concentrations at a single FeO interface layer: A first-principles study

P. Bose,[1,*] A. Ernst,[2] I. Mertig,[1] and J. Henk[2]
[1]*FB Physik, FG Theoretische Physik, Martin-Luther-Universität Halle-Wittenberg, D-06099 Halle (Saale), Germany*
[2]*Max-Planck-Institut für Mikrostrukturphysik, Weinberg 2, D-06120 Halle (Saale), Germany*

(Received 20 August 2008; published 11 September 2008)

The tunneling magnetoresistance (TMR) of Fe/MgO/Fe junctions is strongly diminished by small O concentrations in a single partially oxidized FeO interface layer, as is found by first-principles transport calculations. By modeling the electronic transport through the disordered FeO layer within a supercell approach, the effect is traced back to a significant reduction of specular contributions to the conductances of the parallel configuration of the lead magnetizations. These findings bring theoretical TMR ratios closer to their experimental counterparts and highlight the importance of ordered interfaces for large TMR ratios.

DOI: 10.1103/PhysRevB.78.092403 PACS number(s): 75.47.Jn, 75.70.Cn, 85.75.−d

In magnetoelectronics, a field of research with increasing importance,[1,2] one focus is put on spin-dependent ballistic transport in magnetic tunnel junctions (MTJs, a trilayer of ferromagnetic electrodes separated by an insulating barrier). The conductances for the parallel (G_P) and the antiparallel (G_{AP}) configuration of the electrode magnetizations define the tunnel magnetoresistance (TMR) quantified here as the "optimistic" TMR ratio

$$\delta \equiv \frac{G_P - G_{AP}}{G_{AP}}. \quad (1)$$

For applications, magnetoelectronic devices with TMR ratios larger than 100% at room temperature are demanded. Up to now, this objective could not be reached by MTJs with amorphous barriers, e.g., Al_2O_3.[3–5] More promising are epitaxial MTJs which are expected to provide sufficiently high TMR ratios. Indeed, transport calculations for Fe/MgO/Fe, in which perfect crystallinity, epitaxy, and stoichiometry are assumed, predict TMR ratios that exceed thousand percent.[6]

Although experimental TMR ratios for Fe/MgO/Fe have increased over the years,[7,8] there still appears disagreement with regard to theoretical and experimental values: Experimental TMR ratios are at least one order of magnitude smaller than their theoretical counterparts. One explanation to come into question is that transport calculations mainly rely on ordered samples, hence considering *specular* transport processes in the commonly applied Landauer-Büttiker theory. Instead, *diffusive* transport could play a significant role, as is supported by x-ray surface diffraction experiments, which evidence a disordered (substoichiometric) FeO layer at the Fe/MgO interface.[9,10] Theory substantiates a significant effect of FeO interface layers on the TMR ratio as compared to MTJs without FeO layer.[11] However, these calculations were performed for ordered (stoichiometric) FeO layers. Further, photoelectron spectroscopy experiments establish that off stoichiometry in MgO films on Fe(001) affects the electronic structure at the Fe/MgO interface.[12] Please note that interface properties essentially determine the transport properties.[13,14]

In this Brief Report we report on first-principles transport calculations which provide evidence for an explanation of the aforementioned disagreement of theoretical and experimental TMR ratios by means of a *substoichiometric* FeO interface layer. Both specular and diffusive transport processes are taken into account within a supercell approach. A striking result is that even small O concentrations (less than 5%) reduce the TMR ratio sizably and consequently improve the agreement with experiment significantly.

The effect of disorder in Fe/MgO/Fe MTJs has already been investigated theoretically by superposing incoherently conductances for different MTJs (Ref. 15) and by the coherent-potential approximation without vertex corrections.[16] These approaches lack either coherency or current conservation,[17] both of which are treated properly in a supercell approach. A reduction of the TMR was also found for MTJs with intermixing of Fe and MgO (Ref. 18) as well as with O vacancies in the MgO spacer.[19,20]

First-principles electronic-structure calculations, within the framework of multiple-scattering theory [spin-polarized-Korringa-Kohn-Rostoker (KKR) and layer-KKR methods[21]], provided self-consistent potentials of Fe/MgO/Fe(001) MTJs. The charge density was normalized by Lloyd's formula[22] using a maximum angular momentum of $l_{max}=3$. For the junctions with FeO layers, stoichiometry is assumed (oxygen concentration $c=100\%$), thus allowing the use of a two-dimensional 1×1 unit cell (UC). The atomic positions, in particular those of interstitial oxygen at the interface, were taken from experiment.[23] The self-consistent potentials serve as input for the transport calculations, an approach which proved to be successful.[23]

For treating the substoichiometric junctions properly, ballistic electronic transport was calculated for large supercells (SCs). It turned out that 5×5 SCs, containing 50 sites/layer, provide a reasonable description of the disordered systems within acceptable computer requirements. Instead of computing the SC potentials self-consistently (a very demanding task) these were constructed from the UC potentials. The O potentials in the FeO_c layer were taken from the completely oxidized UC system, whereas the other potentials were computed within the virtual-crystal approximation (concentration-weighted superposition of the potentials of the nonoxidized UC system with those of the completely oxidized UC system).

©2008 The American Physical Society

TABLE I. Optimistic TMR ratios for selected O concentrations c in $Fe/FeO_c/(MgO)_4/Fe$ junctions.

O concentration	Theory	Experiment
0%	520%,[a] 400%,[b] 330%[c]	50%[d]
100%	−50%,[b] −23%,[e] −10% [c]	

[a] References 6 and 29.

[b] Reference 11.

[c] This work.

[d] Reference 8 for 6 ML MgO.

[e] Reference 23.

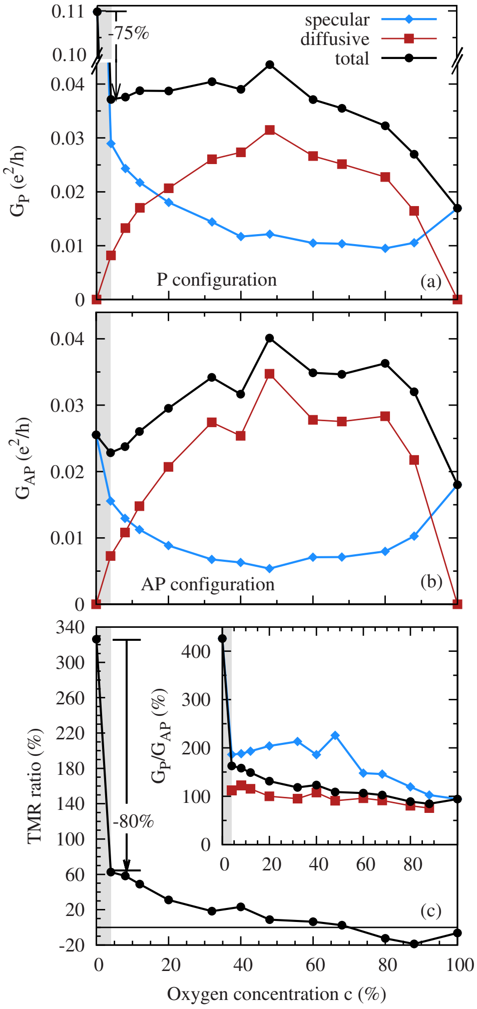

FIG. 1. (Color online) Transport properties of $Fe/FeO_c/(MgO)_4/Fe$ junctions at zero-bias voltage versus oxygen concentration c in the FeO layer. (a) and (b) Conductances G for the (a) parallel P and (b) antiparallel AP configuration. The conductances (black; filled circles) are decomposed into specular (blue; diamonds) and diffusive (red; squares) contributions. (c) Optimistic tunnel magnetoresistance and conductance ratios (inset). The gray areas at low concentrations highlight the region of the sizable drop in G_P and in the TMR ratio [indicated by the vertical arrows in (a) and (c); note the broken ordinate in (a)].

Considering here zero-bias voltage, the conductance

$$G^{SC}(E_F) = \frac{e^2}{h}\int_{2BZ^{SC}} \sum_{\alpha\beta} T_{\alpha\to\beta}(E_F;\boldsymbol{k}^{SC})(dk^{SC})^2 \qquad (2)$$

at the Fermi energy E_F is calculated according to Landauer-Büttiker theory[24] using an S-matrix scheme within layer KKR.[25] The probability $T_{\alpha\to\beta}$ for the incoming Bloch state α at $(E_F;\boldsymbol{k}^{SC})$ being transmitted into the outgoing Bloch state β is integrated over the two-dimensional Brillouin zone (2BZ) of the SC system. An equidistant mesh of 225 wave vectors reproduced TMR ratios of the ordered UC systems (O concentration c=0% and 100%) with sufficient accuracy. The latter was computed with an adaptive integration scheme.[26] Results were conveniently analyzed by means of transmittance maps which display $\Sigma_{\alpha\beta}T_{\alpha\to\beta}(E_F;\boldsymbol{k}^{SC})$ versus $\boldsymbol{k}^{SC}$.

Due to the two-dimensional translational invariance in the leads, w.r.t. the UC, each Bloch state is characterized by a wave vector $\boldsymbol{k}^{UC}=\boldsymbol{k}^{SC}+\boldsymbol{g}^{SC}$, i.e., related to $\boldsymbol{k}^{SC}$ by an *umklapp* with a reciprocal-lattice vector $\boldsymbol{g}^{SC}$ of the SC system. Hence, all tunneling processes $\alpha \to \beta$ can be distinguished as specular or diffusive with respect to the conservation of $\boldsymbol{k}^{UC}$,

$$\boldsymbol{k}^{UC} - \boldsymbol{g}^{SC} = \boldsymbol{k}^{SC} \to \boldsymbol{k}^{SC} = \begin{cases} \boldsymbol{k}^{UC} - \boldsymbol{g}^{SC} & \text{specular} \\ \boldsymbol{k}^{UC'} - \boldsymbol{g}^{SC'} & \text{diffusive} \end{cases} \qquad (3)$$

($\boldsymbol{k}^{SC}$ is conserved). Accordingly, the conductance G^{SC} is decomposed into a specular and a diffusive contribution,

$$G^{SC} = G^{UC}_{spec} + G^{UC}_{diff}. \qquad (4)$$

This partitioning requires computation of the Bloch states at all $\boldsymbol{k}^{UC}=\boldsymbol{k}^{SC}+\boldsymbol{g}^{SC}$ in the UC system and their transformation into the SC basis with bookkeeping of $\boldsymbol{g}^{SC}$.

Because the computation time increases drastically with system size, we focus here on $Fe/FeO_c/(MgO)_4/Fe$ junctions with MgO spacers of four-monolayer (ML) thickness. For each selected O concentration c, a single random configuration was set up in the 5×5 SCs, although one has to average over all topologically inequivalent configurations. This restriction is justified by the rather large supercell and by the small conductance variations with configuration (about 1%) reported earlier.[27,28]

Our SC approach captures the essential features of the ordered sample, as is evident from the agreement with theoretical TMR ratios reported elsewhere (Table I). Differences may be attributed to details in the self-consistent electronic-structure calculations, to the Brillouin-zone integration, and to the geometry of the interfaces. Attention should be paid to the experimental TMR ratio for c=0% (Ref. 8), which is about one order of magnitude smaller than the theoretical values.

The conductances are expected to depend smoothly on O

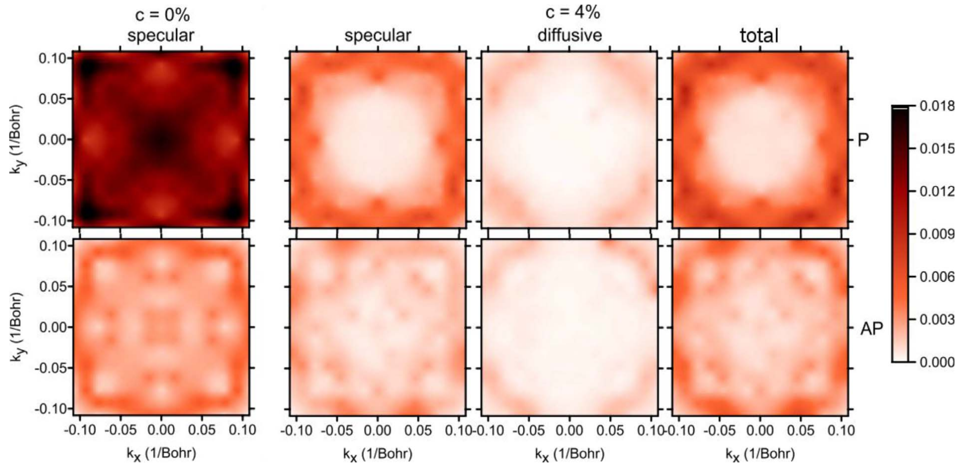

FIG. 2. (Color online) Transmittances $T(E_F;\boldsymbol{k}^{SC})$ versus $\boldsymbol{k}^{SC}=(k_x,k_y)$ for oxygen concentrations $c=0\%$ (left) and 4% (right) in $Fe/FeO_c/(MgO)_4/Fe$ junctions depicted as color (gray) scale in the 2BZ of the 5×5 SC systems. The total transmittances for $c=4\%$ are decomposed into a specular and a diffusive contribution. For $c=0\%$ there are only specular tunnel processes. The data are interpolated to achieve a smooth color gradient.

concentration c. Indeed, G_P and G_{AP} [circles in Fig. 1(a) and 1(b)] show broad maxima around $c=50\%$ which can be attributed to the diffusive contribution (squares). The specular contributions (diamonds) display broad minima at about $c=80\%$ (P) and 50% (AP), respectively. Similar dependences were found for Fe-Cr[100] and Co-Cu[100] systems.[27]

An eye-catching feature is the drop of G_P at small c (gray area). The total conductance decreases by 75% upon increasing c from 0% to 4%, which is mediated by the specular contribution. Note that a concentration of 4% is equivalent to a single O atom in the 5×5 SC. This finding suggests that even small degrees of disorder at the Fe/MgO interfaces reduce G_P sizably. G_{AP} also drops for small c but moderately. Here, the decrease in G_{spec} is almost canceled by the increase in G_{diff}.

The similar shapes of G_P and G_{AP} result in an almost linear c dependence of the TMR ratio in a large range of concentrations [Fig. 1(c)]. Likewise the conductance ratios G_P/G_{AP} depend smoothly on c (inset). The drop of G_P at small concentrations leads to a reduction of the TMR ratio from about 330% for $c=0\%$ to about 60% for $c=4\%$ (gray area) which is attributed to the decrease in the specular contribution to G_P [diamonds in the inset of Fig. 1(c)]. Hence, we are confronted with a large TMR reduction by small degrees of disorder, a finding that considerably improves the agreement of theoretical with experimental TMR ratios (Table I).

The spin-dependent ballistic transport in Fe/MgO/Fe junctions is governed by symmetry selection and proceeds notably by resonant tunneling.[30–32] Thus, large TMR ratios are obtained if interface resonances at identical $(E,\boldsymbol{k})$ at either interfaces of the junction are present, e.g., in symmetric MTJs (here $c=0\%$). Wave vector conservation is less likely in junctions with disorder at one interface. Hence, the diffusive (specular) conductance increases (decreases) with c up to a maximum (minimum). An analogous argument holds for $c=100\%$ and decreasing concentration.

The above explanation is corroborated by inspection of transmittance maps. The P transmittance for $c=0\%$ shows maxima in the center and in the corners [$\boldsymbol{k}\approx(\pm0.09,\pm0.09)$ Bohr^{-1}] of the 2BZ (left in Fig. 2). The AP transmittance is comparably small in the entire 2BZ, with an exception of the corners. This effect can be understood by means of the orbital composition of the electronic states. Δ_1-like states (*sp* orbitals) are located at the 2BZ center and decay least across the MgO spacer in comparison to Δ_2- or Δ_5-like states (*d* orbitals).[29,33,34]

As compared to $c=0\%$, the specular P-transmittance map for $c=4\%$ shows a broad minimum at the 2BZ center (right in Fig. 2). This feature, in conjunction with the much less pronounced contributions at the corners, results in the sizable conductance drop of 75%. On the contrary, the specular AP-transmittance maps for $c=0\%$ and 4% compare well. The maps of the diffusive P and AP contributions look very similar too. These findings corroborate that resonant tunneling is less likely for $c>0\%$.

As a "rule of thumb," the relative contribution of the 2BZ center to the conductance increases with MgO spacer thickness.[29,33] Hence, we expect that small oxygen concentrations strongly reduce theoretically predicted TMR ratios also for thicker MgO spacers, thereby improving the agreement with experiment in general (cf. Table I).

In summary, the present transport calculations reveal that oxygen concentrations at the interface of a few percent reduce the tunnel magnetoresistance of Fe/MgO/Fe junctions sizably. Our findings suggest that the disagreement between theoretical and experimental TMR ratios is due to substoichiometric FeO layers with small oxygen concentrations or, reworded, large TMR ratios require perfectly ordered interfaces. Because small degrees of imperfections at the interfaces of real samples can hardly by excluded, systematic studies of the disorder in MTJs (Ref. 12) are encouraged.

This work is supported by the *Sonderforschungsbereich* 762, “Functionality of Oxidic Interfaces.” P.B. is a member of the International Max Planck Research School for Science and Technology of Nanostructures.

---

*peter.bose@physik.uni-halle.de

[1] G. A. Prinz, Science **282**, 1660 (1998).

[2] S. A. Wolf, A. Y. Chtchelkanova, and D. M. Treger, IBM J. Res. Dev. **50**, 101 (2006).

[3] T. Miyazaki and N. Tezuka, J. Magn. Magn. Mater. **139**, L231 (1995).

[4] J. S. Moodera, L. R. Kinder, T. M. Wong, and R. Meservey, Phys. Rev. Lett. **74**, 3273 (1995).

[5] D. Wang, C. Nordman, J. M. Daughton, Z. Qian, and J. Fink, IEEE Trans. Magn. **40**, 2269 (2004).

[6] J. Mathon and A. Umerski, Phys. Rev. B **63**, 220403(R) (2001).

[7] S. S. P. Parkin, C. Kaiser, A. Panchula, P. M. Rice, B. Hughes, M. Samant, and S.-H. Yang, Nat. Mater. **3**, 862 (2004).

[8] S. Yuasa, T. Nagahama, A. Fukushima, Y. Suzuki, and K. Ando, Nat. Mater. **3**, 868 (2004).

[9] H. L. Meyerheim, R. Popescu, J. Kirschner, N. Jedrecy, M. Sauvage-Simkin, B. Heinrich, and R. Pinchaux, Phys. Rev. Lett. **87**, 076102 (2001).

[10] H. L. Meyerheim, R. Popescu, N. Jedrecy, M. Vedpathak, M. Sauvage-Simkin, R. Pinchaux, B. Heinrich, and J. Kirschner, Phys. Rev. B **65**, 144433 (2002).

[11] C. Heiliger, P. Zahn, B. Y. Yavorsky, and I. Mertig, Phys. Rev. B **72**, 180406(R) (2005).

[12] M. Müller, F. Matthes, and C. M. Schneider, Europhys. Lett. **80**, 17007 (2007).

[13] P. X. Xu, V. M. Karpan, K. Xia, M. Zwierzycki, I. Marushchenko, and P. J. Kelly, Phys. Rev. B **73**, 180402(R) (2006).

[14] E. Y. Tsymbal, K. D. Belashchenko, J. P. Velev, S. S. Jaswal, M. van Schilfgaarde, I. I. Oleynik, and D. A. Stewart, Prog. Mater. Sci. **52**, 401 (2006).

[15] C. Heiliger, P. Zahn, and I. Mertig, J. Magn. Magn. Mater. **316**, 478 (2007).

[16] X.-G. Zhang, W. H. Butler, and A. Bandyopadhyay, Phys. Rev. B **68**, 092402 (2003).

[17] K. Carva, I. Turek, J. Kudrnovský, and O. Bengone, Phys. Rev. B **73**, 144421 (2006).

[18] J. Mathon and A. Umerski, Phys. Rev. B **74**, 140404(R) (2006).

[19] J. P. Velev, K. D. Belashchenko, S. S. Jaswal, and E. Y. Tsymbal, Appl. Phys. Lett. **90**, 072502 (2007).

[20] H. Itoh, J. Ozeki, and J. Inoue, J. Magn. Magn. Mater. **303**, e205 (2006).

[21] *Electron Scattering in Solid Matter*, edited by J. Zabloudil, R. Hammerling, L. Szunyogh, and P. Weinberger (Springer, Berlin, 2005).

[22] R. Zeller, J. Phys.: Condens. Matter **20**, 035220 (2008).

[23] C. Tusche, H. L. Meyerheim, N. Jedrecy, G. Renaud, A. Ernst, J. Henk, P. Bruno, and J. Kirschner, Phys. Rev. Lett. **95**, 176101 (2005).

[24] Y. Imry and R. Landauer, Rev. Mod. Phys. **71**, S306 (1999).

[25] J. M. MacLaren, X.-G. Zhang, W. H. Butler, and X. Wang, Phys. Rev. B **59**, 5470 (1999).

[26] J. Henk, Phys. Rev. B **64**, 035412 (2001).

[27] J. Velev and W. H. Butler, Phys. Rev. B **69**, 024404 (2004).

[28] J. Velev and W. H. Butler, J. Appl. Phys. **97**, 10C517 (2005).

[29] W. H. Butler, X.-G. Zhang, T. C. Schulthess, and J. M. MacLaren, Phys. Rev. B **63**, 054416 (2001).

[30] O. Wunnicke, N. Papanikolaou, R. Zeller, P. H. Dederichs, V. Drchal, and J. Kudrnovský, Phys. Rev. B **65**, 064425 (2002).

[31] K. D. Belashchenko, J. Velev, and E. Y. Tsymbal, Phys. Rev. B **72**, 140404(R) (2005).

[32] J. P. Velev, K. D. Belashchenko, and E. Y. Tsymbal, Phys. Rev. Lett. **96**, 119601 (2006).

[33] C. Heiliger, P. Zahn, and I. Mertig, Mater. Today **9**, 46 (2006).

[34] S. Yuasa and D. D. Djayaprawira, J. Phys. D **40**, R337 (2007).

3.2 Fe(001)/x(Mn)/Vacuum/Fe(001)

This part of the PhD work comprises *ab-initio* investigations of the principle effect of layer-wise antiferromagnetic (LAFM) interlayers on the electronic transport in magnetic tunnel junctions. The project was motivated by the experimental observation of a 2 ML oscillation in the TMR ratios as a function of the Cr thickness d_{Cr} in Fe(001)/d_{Cr}(Cr)/$\mathrm{Al_2O_3}$/FeCo(001) MTJs [99].

Since $\mathrm{Al_2O_3}$ tunnel barriers are – due their amorphous structure and therefore, the missing in-plane translational symmetry – difficult to treat within the layer-KKR method, we resorted to another setup (see Fig. 3.3). In detail, we used the self-consistent potentials and structural information of an afore reported first-principles investigation of LAFM Mn films on an Fe substrate [100] to study the electronic transport properties in Fe(001)/x(Mn)/Vac/Fe(001) MTJs. Vacuum as tunnel barrier provides the advantage to clearly extract the pure effect of the LAFM Mn on the tunneling Bloch states. In particular, it does not incorporate symmetry selection processes which are a significant attribute of crystalline barriers [101, 102].

The calculated I-V-characteristics reveal, as observed in the experiment, 2 ML oscillations of the TMR ratio as a function of the number of Mn monolayers x. The even-odd modulations can be explained by means of a spin-filter effect whose origin is traced back to the electronic states within the Mn layers at the vacuum interface.

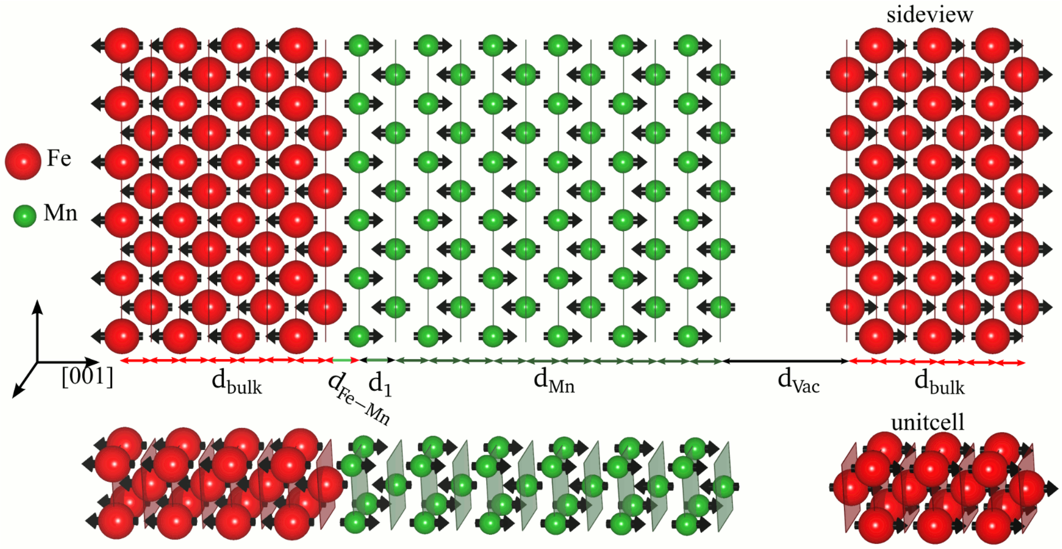

Figure 3.3: Schematic of the structural setup of an Fe(001)/12Mn/Vacuum/Fe(001) magnetic tunnel junction (MTJ) with layer distances $\mathrm{d_{bulk}} = 1.43$Å, $\mathrm{d_{Fe-Mn}} = 1.65$Å, $\mathrm{d_1} = 1.80$Å, $\mathrm{d_{Mn}} = 1.69$Å, and $\mathrm{d_{Vac}} = 6.24$Å. Black arrows at the Fe and Mn sites emphasize the local magnetic directions. The MTJ is shown here for an anti-parallel magnetic configuration. The Mn film grows layer-wise antiferromagnetically on the Fe substrate.

PHYSICAL REVIEW B **75**, 100402(R) (2007)

Oscillatory tunneling magnetoresistance caused by antiferromagnetic Mn layers

P. Bose,[1] I. Mertig,[1] and J. Henk[2]
[1]*Martin-Luther-Universität Halle-Wittenberg, FB Physik, FG Theoretische Physik, D-06099 Halle (Saale), Germany*
[2]*Max-Planck-Institut für Mikrostrukturphysik, Weinberg 2, D-06120 Halle (Saale), Germany*

(Received 23 November 2006; revised manuscript received 23 January 2007; published 22 March 2007)

The ballistic magnetoresistance of tunnel junctions that comprise Mn films is found to exhibit oscillations with increasing Mn-film thickness, as is investigated by means of first-principles electronic-structure and transport calculations. The period of two monolayers is directly related to the layer-wise antiferromagnetic structure of the Mn films, in particular to the alternating magnetization at the interfaces. These findings substantiate unequivocally the effect of the electronic and magnetic structure of interfaces on the conductance of tunnel junctions.

DOI: 10.1103/PhysRevB.75.100402 PACS number(s): 75.47.Jn, 75.70.Ak, 85.75.−d

Magnetoelectronic devices are typically composed of several parts, therefore comprising necessarily interfaces. With increasing miniaturization, structural, electronic, and magnetic properties of these interfaces become more and more important and are believed to determine essentially transport properties of spintronics devices.

In an experiment, interface structures can hardly be modified in a fully controlled manner. Typically, a series of samples needs to be fabricated under various preparation conditions, the transport properties of which are obtained subsequently. Although preparation techniques have made significant progress in the recent past, well-defined (on an atomic scale) interface structures are difficult to produce. Thus, experimentally achieved findings involve often a statistical (configurational) average.

As an example, we address Fe/MgO/Fe magnetic tunnel junctions (MTJs) that are among the in-depth investigated systems of magnetoelectronics.[1,2] In early theoretical investigations, it was assumed that MgO continues epitaxially the bcc lattice of the Fe(001) electrodes (e.g., Refs. 3 and 4). However, recent experimental investigations of the Fe/MgO interface structure revealed a partially occupied FeO layer that was found to change the theoretical tunnel magnetoresistance (TMR) drastically, with respect to that of the "ideal" structure.[5–8]

One particular issue that is not well understood to date is the influence of the magnetic structure of an interface on the TMR, in particular the effect of antiferromagnetic order. A crucial point is that the magnetic and the geometric structure are not as independent as requested, as is for example the case for Fe/MgO interfaces. As a consequence, one needs well-specified samples to extricate interface effects from transport data.

In this paper, we propose to consider layerwise antiferromagnetically (LAFM) ordered films for investigating the magnetic structure of interfaces and its effect on the ballistic TMR of planar tunnel junctions. Layerwise antiferromagnetic structures are found in epitaxial Cr and Mn films on Fe(001).[9–11]

In a recent study, the TMR of Fe/Cr(x)/Al$_2$O$_3$/FeCo tunnel junctions was investigated both experimentally and theoretically.[12] The most striking result is an oscillatory TMR with a period of two monolayers (ML) that was explained by means of the Cr band structure at $\vec{k}_{\parallel}=0$. However, due to the amorphous Al$_2$O$_3$ tunnel barrier and the polycrystalline FeCo electrode, the transport is likely to be diffusive ($\vec{k}_{\parallel}$ not conserved) and not specular ($\vec{k}_{\parallel}$ conserved). To obtain ballistic transport, we deliberately replaced Al$_2$O$_3$ and FeCo by vacuum and Fe, respectively. Consequently, one is not restricted to band-structure calculations but state-of-the-art methods for computing ballistic transport of MTJs can be applied as well.

The intention of the present work is to identify unequivocally the effects of a LAFM film (Mn) between a tunnel barrier (vacuum) and an electrode (Fe) on the TMR (Fig. 1). The two major magnetic configurations parallel (P) and antiparallel (AP) are defined in terms of the Fe-electrode magnetizations. As was shown recently by first-principles electronic-structure calculations,[13] Mn couples LAFM with respect to the Fe(001) substrate, provided the Mn film is sufficiently thick (>7 ML). These findings are consistent with experimental observations.[14] That Mn films on Fe(001) serve well for our purposes was also shown in a recent investigation by means of spin-resolved scanning tunneling

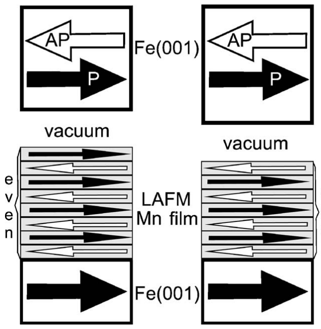

FIG. 1. Fe(001)/Mn(x)/vacuum/Fe(001) tunnel junctions for an even (left) and an odd (right) number x of Mn layers (schematic). The local magnetizations (horizontal arrows) are aligned layer-wise antiferromagnetically (LAFM) within the Mn films. The magnetic configurations P (parallel, as indicated in the top electrode) and AP (antiparallel) are defined with respect to the Fe-electrode magnetizations, with that of the bottom electrode fixed.

©2007 The American Physical Society

microscopy.[15,16] In that work, the LAFM structure was directly proven.

Consequently, we focus in this work on MTJs with Mn film thickness x ranging from 7 to 12 ML. The main difference of MTJs with an even and an odd x is the orientation of the magnetization in the Mn top layer. For even (odd) x, the latter is parallel (antiparallel) to both Fe-electrode magnetizations in the P configuration. Thus, one could expect an even-odd effect in the TMR, provided the influence of the Mn top layer is large enough.

In summary, the present theoretical *ab initio* investigation addresses the following questions: How large is the TMR, in particular is it as small as in STM experiments and in model calculations?[16] How does the TMR depend on the thickness of the Mn film? And is there an even-odd effect that is related to the respective Mn top-layer magnetization?

In a first step, *ab initio* electronic-structure calculations were performed within the framework of the local spin density approximation to density functional theory. The self-consistent potentials serve as input for the transport calculations. Both electronic-structure and transport properties were obtained with a spin-polarized layer-KKR computer code.

The computations for planar Fe(001)/Mn(x)/vacuum/Fe(001) MTJs, $x=7,\ldots,12$ ML, follow closely those for Fe(001)/Mn(x)/vacuum reported in Ref. 13. The number of vacuum layers was fixed to 3 ML (corresponding to 5.7 Å electrode separation). Thus, electronic states localized at different electrodes do not interact significantly.

The tunnel current $I(V)$ of a MTJ is calculated within Landauer-Büttiker theory.[17,18] In order to treat a nonzero bias voltage V, the potentials in one electrode were shifted rigidly by eV.[19,20] A linear voltage drop within the vacuum region is assumed.[21] This non-self-consistent treatment is corroborated by self-consistent results for Fe/FeO/MgO/Fe MTJs.[22]

The tunnel current $I(V)$ and the conductance $G(V)$,

$$I(V) = G(V)V = \frac{e^2}{h}\int_{\mu_T}^{\mu_B} T(E,V)dE, \tag{1}$$

are expressed as integral of the transmittances $T(E,V)$ in the "energy window of tunneling" given by the chemical potentials of the bottom (B) and the top (T) electrode, $eV=\mu_B-\mu_T$. $T(E,V)$ is obtained by integrating the wavevector-resolved transmittances $T(E,V;\vec{k}_\parallel)$ over the two-dimensional Brillouin zone (2BZ) (Ref. 18)

$$T(E,V) = \int_{2\mathrm{BZ}} T(E,V;\vec{k}_\parallel)dk^2. \tag{2}$$

$T(E,V;\vec{k}_\parallel)$ is the sum of the transmission probabilities of all incoming (in $\mathcal{B}$) and outgoing (in $\mathcal{T}$) Bloch states of the leads. For the 2BZ integration an adaptive-mesh algorithm was used.[23] The tunnel magnetoresistance $\delta(V)$ is defined as the asymmetry of the tunnel currents for the parallel and antiparallel magnetic configurations of the Fe electrodes (Fig. 1), $\delta(V)=[I_P(V)-I_{AP}(V)]/[I_P(V)+I_{AP}(V)]$.

To investigate interface effects on the conductance of a MTJ, it is highly desirable that only properties of a single interface layer change while those of the remaining layers do not. For Fe(001)/Mn(x)/vacuum, this was shown by first-principles calculations to be the case to a good approximation,[13] provided the number of Mn layers x is large enough ($x \geqslant 7$ ML). If so, the main difference of thick Mn films with an even and an odd number of Mn layers is the opposite alignment of the top-layer magnetizations (Fig. 1).

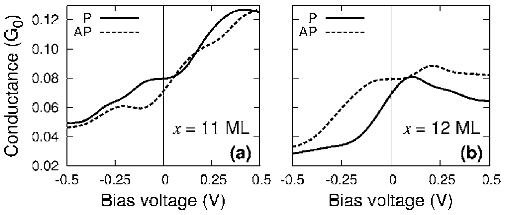

FIG. 2. Conductances of Fe/Mn(x)/vacuum/Fe magnetic tunnel junctions for $x=11$ ML (a) and $x=12$ ML (b) of Mn for parallel (P, solid) and antiparallel (AP, dashed) magnetic configurations versus bias voltage. $G_0=e^2/h$ is the quantum of conductance.

For the bias dependence of the conductances with $x=11$ ML [Fig. 2(a)], one finds $G_P(V) > G_{AP}(V)$ almost in the entire range of voltages. Increasing x by 1 ML reverses the order to $G_P(V) < G_{AP}(V)$. Note further that $G_P(V)$ and $G_{AP}(V)$ exhibit a rather similar bias dependence for both x, indicating a small TMR $\delta(V)$ (in absolute value). The variation upon increasing x indicates that there are still differences in the electronic structure of the Mn films, although x is rather large.

These findings suggest that the Mn top layer acts mainly as a spin filter which suppresses the transmission of electrons of one spin orientation with respect to that of the other (for oxidized Co surface, see Ref. 24). It essentially determines the order of the conductances $G_P(V)$ and $G_{AP}(V)$. Consequently, the TMR $\delta(V)$ changes sign as a function of the Mn-film thickness (Fig. 3). This even-odd effect shows up clearly for negative bias voltages V (i.e., for tunneling into the bottom electrode). For an even x, $\delta(V)$ is negative (blue) whereas for odd x, it is positive (red). For positive V, the thickness dependence is more complicated but also shows 2-ML oscillations.

The TMR of the paradigm of MTJs, Fe(001)/MgO(x)/Fe(001), approaches 1 with increasing MgO thickness (see, e.g., Ref. 5). For Fe/Mn(x)/vacuum/Fe, however, the TMR is comparatively small, with a maximum of about 0.3. On average, $|\delta(V)|$ is even smaller. In particular, it shows no unequivocal trend (i.e., decrease or increase) upon increasing x, as is explained by the fact that a Mn film is conducting (in contrast to an insulating MgO film). These findings agree nicely with experimental data and with those of a model calculation.[16]

Recapitulating at this point, the TMR of Fe/Mn(x)/vacuum/Fe MTJs shows an even-odd effect, prominently at negative bias voltages [Fig. 3(a)]. The tunnel magnetoresistance agrees nicely with the experimental one for Fe/Cr(x)/Al$_2$O$_3$/FeCo MTJs, which also exhibit a 2-ML period in particular voltage ranges.[12] These findings suggest that the oscillations are explained by the same mechanism,

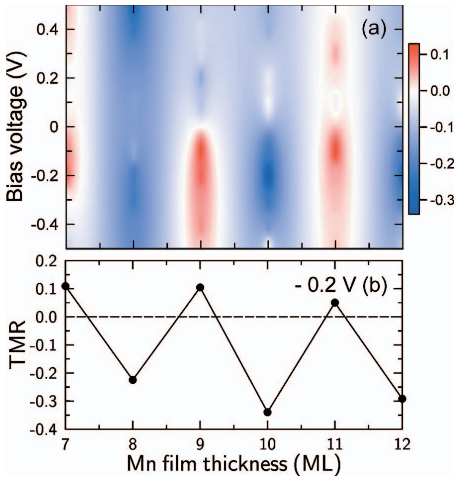

FIG. 3. (Color) (a) Tunnel magnetoresistance (TMR) in Fe/Mn(x)/vacuum/Fe magnetic tunnel junctions versus number x of Mn layers (abscissa) and bias voltage (ordinate), depicted as color scale (right). Data are interpolated to obtain a smooth color gradient. (b) TMR versus x at −0.2 V bias voltage.

irrespectively of the transport being specular or diffusive.

The TMR oscillations cannot be explained by the electronic structure of a MTJ at a single $\vec{k}_\parallel$. Electronic states in the entire 2BZ can contribute to the transmittance [Eq. (2)], although typically a few small regions in reciprocal space outweigh by far the contribution of the remainder. First evidence for the 2-ML oscillations being related to the Mn top layer is provided by the observation that the $\vec{k}_\parallel$-resolved zero-bias transmittance $T(E,V;\vec{k}_\parallel)$ for P (AP) and $x=11$ ML agrees well with that for AP (P) and $x=12$ ML (not shown). Further support is given by comparing the layer-, spin-, and angular-momentum-resolved Bloch spectral densities (SD) with $T(E,V;\vec{k}_\parallel)$, being aware that there is no one-to-one correspondence of these quantities.

Figure 4 shows that structures in the transmittances (top row) have counterparts in the *sp* spectral densities of the surface layer of the Fe top electrode (c), (d) and of the Mn top layer (e), (f). We would like to draw the reader's attention to the selected features, as indicated in black. For the other layers, there is no such clear correspondence, as is evident, for instance, for the Mn layer at the Fe/Mn interface of the bottom electrode (g), (h) and for an Fe bulk layer (i), (j). Thus, these layers play a minor role concerning the electronic transport. From this finding, one may conclude that layers close to the tunnel barrier govern the transport properties. Please note that the change of the potential is largest at these layers.[31]

The *d*-state spectral densities do not fit well to the transmittances, which implies that these states contribute much less to the conductance than *sp* states, regardless of their much larger SD. This observation is consistent with the

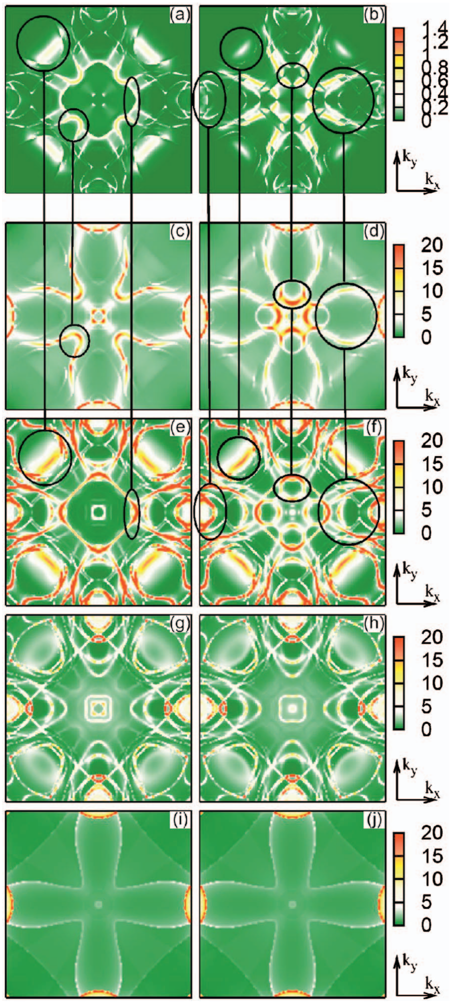

FIG. 4. (Color) Transport properties of a Fe/Mn(11)/vacuum/Fe tunnel junctions in P (left column) and AP (right column) configuration. Top row: transmittances $T(E,V;\vec{k}_\parallel)$ in the 2BZ at zero bias, shown as color scale (right). Bottom rows: spectral densities (SDs) at the Fermi level for *sp* electronic states (color scales in states/Hartree) for the surface layer of the top Fe electrode (c), (d), the Mn top layer (e), (f), the Mn layer at the Mn/Fe interface of the bottom electrode (g), (h), and of an Fe bulk layer (i), (j). Selected features are indicated in black.

Slonczewski model.[25] Also spectral densities decomposed with respect to point-group representations at the 2BZ center[12] do not agree well with the transmittances.

A conducting spacer can give rise to quantum-well states which may determine the transport properties considerably, as was shown for thin Cu(001) films in a MTJ.[26,27] The oscillations in the TMR as a function of Cu thickness have a period that is given by the nesting vectors of the constant-energy surface. In contrast to Cu, with its highly conducting *sp* states at the Fermi level, Mn quantum-well states do not show up in the transport properties.[30,32] Therefore, they cannot be responsible for the 2-ML oscillations.

Spin-polarized surface states would increase the transmission in one spin channel, thereby reducing or increasing the TMR. Consequently, they would affect the amplitude of the TMR oscillation but not its 2-ML period. Surface states were indeed found in experiments on Mn/Fe(001).[14,16] However, the most prominent one, at +0.8 eV relative to the Fermi level,[13] is not within the range of bias voltages considered here.

In a recent theoretical investigation, the tunneling anisotropic magnetoresistance in Fe(001)/vacuum/Cu(001) was attributed mainly to a minority-spin surface resonance in Fe(001).[28] For the Fermi energy, it shows up close to the 2BZ center.[29] In that system, the Cu electrode provides conducting channels in the entire 2BZ, in contrast to a Mn/Fe electrode. Consequently, these surface resonances—showing up in our calculations at the top electrode [e.g., the square-shaped structure at the center of Fig. 4(c)]—have little effect on the TMR studied in this paper.

The electronic and magnetic structure of layers close to the tunnel barrier determine essentially the transport properties in MTJs, for instance, the TMR. This conclusion is obtained by first-principles calculations for Fe(001)/Mn(x)/vacuum/Fe(001) MTJs, $x=7,\ldots,12$ ML. The LAFM order in the Mn films results in TMR oscillations with a period of 2 ML (even-odd effect), as is explained by the alternating orientation of the top-layer magnetization upon increasing x by 1 ML. These theoretical results suggest to investigate experimentally similar systems, e.g., by spin-resolved STM.

The LAFM order of conducting spacers and the associated even-odd effect in the TMR provides an additional degree of freedom for spin-dependent transport in MTJs, especially in connection with advanced preparation techniques. Hence, the presented results might be important for technological applications.

---

*Electronic address: peter.bose@physik.uni-halle.de

[1] J. Faure-Vincent, C. Tiusan, E. Jouguelet, F. Canet, M. Sajieddine, C. Bellouard, E. Popova, M. Hehn, F. Montaigne, and A. Schuhl, Appl. Phys. Lett. **82**, 4507 (2003).

[2] S. Yuasa, T. Nagahama, A. Fukushima, Y. Suzuki, and K. Ando, Nat. Mater. **3**, 868 (2004).

[3] W. H. Butler, X.-G. Zhang, T. C. Schulthess, and J. M. MacLaren, Phys. Rev. B **63**, 054416 (2001).

[4] J. Mathon and A. Umerski, Phys. Rev. B **63**, 220403(R) (2001).

[5] C. Tusche, H. L. Meyerheim, N. Jedrecy, G. Renaud, A. Ernst, J. Henk, P. Bruno, and J. Kirschner, Phys. Rev. Lett. **95**, 176101 (2005).

[6] J. P. Velev, K. D. Belashchenko, and E. Y. Tsymbal, Phys. Rev. Lett. **96**, 119601 (2006).

[7] C. Tusche, H. L. Meyerheim, N. Jedrecy, G. Renaud, A. Ernst, J. Henk, P. Bruno, and J. Kirschner, Phys. Rev. Lett. **96**, 119602 (2006).

[8] X.-G. Zhang, W. H. Butler, and A. Bandyopadhyay, Phys. Rev. B **68**, 092402 (2003).

[9] S. Andrieu, M. Finazzi, P. Bauer, H. Fischer, P. Lefevre, A. Traverse, K. Hricovini, G. Krill, and M. Piecuch, Phys. Rev. B **57**, 1985 (1998).

[10] E. C. Passamani, B. Croonenborghs, B. Degroote, and A. Vantomme, Phys. Rev. B **67**, 174424 (2003).

[11] C. L. Gao, Ph.D. thesis, Martin-Luther-Universität Halle-Wittenberg, Halle, Germany, 2006.

[12] T. Nagahama, S. Yuasa, E. Tamura, and Y. Suzuki, Phys. Rev. Lett. **95**, 086602 (2005).

[13] A. Ernst, J. Henk, and R. K. Thapa, J. Phys.: Condens. Matter **17**, 3269 (2005).

[14] T. K. Yamada, M. M. J. Bischoff, G. M. M. Heijnen, T. Mizoguchi, and H. van Kempen, Phys. Rev. Lett. **90**, 056803 (2003).

[15] U. Schlickum, Ph.D. thesis, Martin-Luther-Universität Halle-Wittenberg, Germany, 2005.

[16] U. Schlickum, C. L. Gao, W. Wulfhekel, J. Henk, P. Bruno, and J. Kirschner, Phys. Rev. B **74**, 054409 (2006).

[17] Y. Imry and R. Landauer, Rev. Mod. Phys. **71**, S306 (1999).

[18] J. M. MacLaren, X.-G. Zhang, W. H. Butler, and X. Wang, Phys. Rev. B **59**, 5470 (1999).

[19] J. Henk and P. Bruno, Phys. Rev. B **68**, 174430 (2003).

[20] H. F. Ding, W. Wulfhekel, J. Henk, P. Bruno, and J. Kirschner, Phys. Rev. Lett. **90**, 116603 (2003).

[21] C. Heiliger, P. Zahn, B. Y. Yavorsky, and I. Mertig, Phys. Rev. B **72**, 180406(R) (2005).

[22] C. Zhang, X.-G. Zhang, P. S. Krstić, H.-P. Cheng, W. H. Butler, and J. M. MacLaren, Phys. Rev. B **69**, 134406 (2004).

[23] J. Henk, Phys. Rev. B **64**, 035412 (2001).

[24] K. D. Belashchenko, E. Y. Tsymbal, M. van Schilfgaarde, D. A. Stewart, I. I. Oleinik, and S. S. Jaswal, Phys. Rev. B **69**, 174408 (2004).

[25] J. C. Slonczewski, Phys. Rev. B **39**, 6995 (1989).

[26] S. Yuasa, T. Nagahama, and Y. Suzuki, Science **297**, 234 (2002).

[27] H. Itoh, J. Inoue, A. Umerski, and J. Mathon, Phys. Rev. B **68**, 174421 (2003).

[28] A. N. Chantis, K. D. Belashchenko, E. Y. Tsymbal, and M. van Schilfgaarde, Phys. Rev. Lett. **98**, 046601 (2007).

[29] J. A. Stroscio, D. T. Pierce, A. Davies, R. J. Celotta, and M. Weinert, Phys. Rev. Lett. **75**, 2960 (1995).

[30] P. H. Dederichs, P. Mavropoulos, O. Wunnicke, N. Papanikolaou, V. Bellini, R. Zeller, V. Drchal, and J. Kudrnovský, J. Magn. Magn. Mater. **240**, 108 (2002).

[31] For Fe/MgO/Fe junctions these are obviously the layers at the Fe/MgO interfaces.

[32] Resonant tunneling would show up as so-called hot spots in the transmittance (Ref. 30).

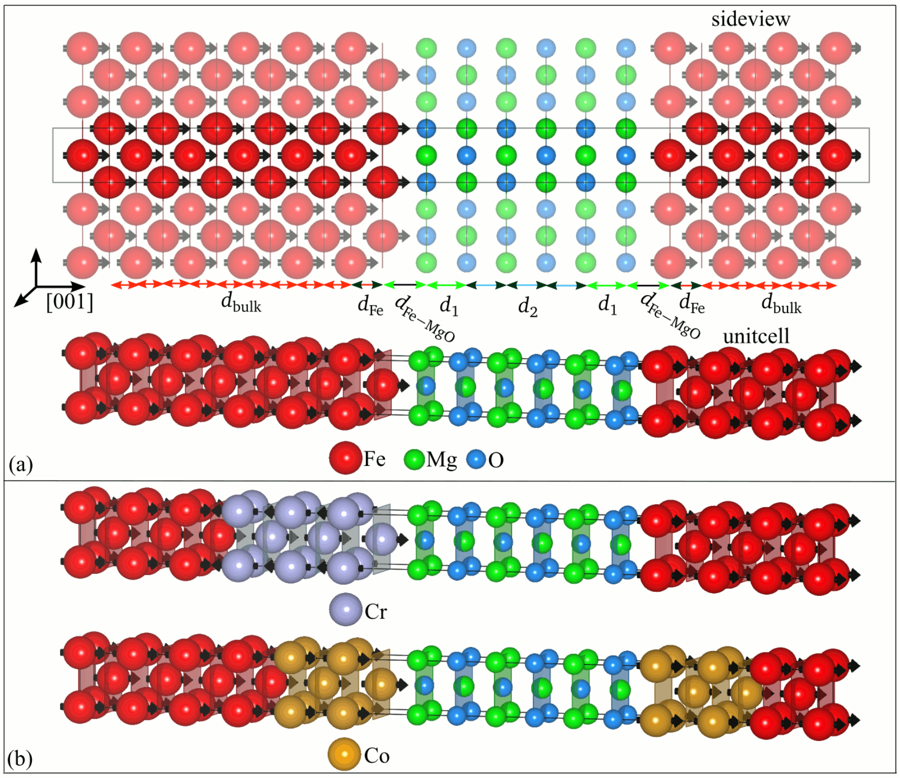

Figure 3.4: (a) Schematic of a structural setup Fe(001)/6MgO/Fe(001) magnetic tunnel junction (MTJ) with layer distances $d_{\mathrm{bulk}} = 1.43$Å, $d_{\mathrm{Fe}} = 1.69$Å, $d_{\mathrm{Fe-MgO}} = 2.35$Å, $d_1 = 2.15$Å, and $d_2 = 2.12$Å. The interlayers in (b) are embedded by replacing Fe atoms at the interfaces with Cr and Co atoms, respectively. Black arrows at the Fe, Cr, and Co sites indicate the local magnetic directions. The MTJs are shown here for a parallel magnetic configuration. Cr films (top MTJ in (b)) grow layer-wise antiferromagnetically on the Fe substrate.

3.3 Cr and Co interlayers in Fe/MgO/Fe magnetic tunnel junctions

In this project I addressed the question how the spin-dependent tunneling currents in Fe/MgO /Fe magnetic tunnel junctions (MTJs) are affected by the insertion of layer-wise antiferromagnetic (LAFM) Cr or by the embedding of ferromagnetic Co interlayers (see Fig. 3.4).

The thickness dependence of Cr in Fe(001)/x(Cr)/MgO/Fe(001) MTJs has been experimentally investigated to clarify two aspects of the fundamental physics in MTJs [103]: on the one hand to study non-specular scattering processes (see P41ff), which are assumed to appear at the Cr/MgO interfaces, and on the other hand to elucidate the role of the electrode/barrier interface in tunneling conductances. Since the computation of non-specular conductance contributions requires numerical very time-consuming supercell calculations I focused in my first-principles investigations only on the latter aspect.

The calculated TMR ratios as a function of the Cr thicknesses exhibit, similar to the experiment, a strong decay with an additional even-odd modulation. The analysis of the associated transmission probabilities reveals that the tunneling of Bloch states is affected by a combination of two main mechanisms. *(i)* A spin-filter effect which is induced by the enhanced magnetic moments of the Cr interface layers; and *(ii)* the presence of complex bands which are formed within the Cr interlayers. The oscillations are therefore mixtures of 2 ML oscillations of magnetic origin and superpositions of the individual modulations of the tunneling Bloch states, which can be traced back to the complex wave vectors in the complex band structure.

Motivated by theoretical predictions with infinite bcc Co leads [104], it has been experimentally found that tunnel magnetoresistance ratios in Fe/MgO/Fe MTJs could be enhanced by the insertion of ultrathin bcc Co interlayers [27]. Based on these measurements I performed ab *inito* electronic transport calculations of Fe/MgO/Fe MTJs with small embedded Co interlayers to reproduce and analyze the experimental findings. It turns out that Co interlayers in the regarded setup do not enhance the TMR ratios with respect to MTJs without interlayers.

Mater. Res. Soc. Symp. Proc. Vol. 1183 © 2009 Materials Research Society 1183-FF07-02

Tailoring TMR ratios by ultrathin magnetic interlayers: A first-principles investigation of Fe/MgO/Fe

Peter Bose,[1,3] Peter Zahn,[1] Jürgen Henk,[2] and Ingrid Mertig[1,2]

[1]Physics Institute of the Martin Luther University Halle-Wittenberg, Theory Department,
von Seckendorff-Platz 1, D-06120 Halle (Saale), Germany
[2]Max Planck Institute of Microstructure Physics, Theory Department,
Weinberg 2, D-06120 Halle (Saale), Germany
[3]International Max Planck Research School for Science and Technology of Nanostructures,
MPI of Microstructure Physics, Weinberg 2, D-06120 Halle (Saale), Germany

ABSTRACT

For spintronic device applications, large and in particular tunable tunnel magnetoresistance (TMR) ratios are inevitable. Fully crystalline and epitaxially grown Fe/MgO/Fe magnetic tunnel junctions (MTJs) are well suited for this purpose and, thus, are being intensively studied [1]. However, due to imperfect interfaces it is difficult to obtain sufficiently large TMR ratios that fulfill industrial demands (e.g. [2]).

A new means to increase TMR ratios is the insertion of ultra-thin metallic buffer layers at one or at both of the Fe/MgO interfaces. With regard to their magnetic and electronic properties as well as their small lattice mismatch to Fe(001), Co and Cr spacer are being preferably investigated.

We report on a systematic first-principles study of the effect of Co and Cr buffers (with thicknesses up to 6 ML) in Fe/MgO/Fe magnetic tunnel junctions (MTJs) on the spin-dependent conductance. The results of the transport calculations reveal options to specifically tune the TMR ratio. Symmetric junctions, i.e. with Co buffers at both interfaces, exhibit for some thicknesses much larger TMR ratios in comparison to those obtained for Fe-only electrodes. Further, antiferromagnetic Cr films at a single interface introduce TMR oscillations with a period of 2 ML, a feature which provides another degree of freedom in device applications. The comparison of our results with experimental findings shows agreement and highlights the importance of interfaces for the TMR effect.

INTRODUCTION

Fully crystalline Fe/MgO/Fe MTJs show very high TMR ratios [3-6]. After intensive studies of these systems, the research was gradually extended to other promising systems. MgO tunnel junctions with amorphous CoFeB electrodes for instance were found to improve structural and magnetic properties, resulting in giant TMR ratios [1].

The detailed structure of the interfaces in Fe/MgO/Fe essentially determines the spin-polarized current. Thus, it is obvious to manipulate the interfaces in a controlled way to achieve larger TMR ratios. Considering the magnetic profiles in Figs. 1 and 2, it is expected that Cr and Co buffers have a sizable effect on the tunnel current, and especially on its spin-polarization.

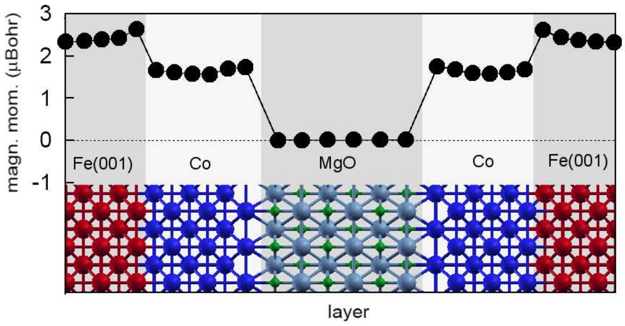

Figure 1. Layer-resolved magnetic moments of bcc Fe(001)/*x*(Co)/6MgO/*x*(Co)/Fe(001) magnetic tunnel junction with *x* = 6. The geometry of the MTJ is sketched at the bottom.

Magnetic tunnel junctions with bcc Co electrodes are theoretically predicted [7] to provide much larger TMR ratios than those with Fe electrodes. However, Co grows only up to a few monolayers on MgO in the bcc phase; for thicker layers a structural transition to the hcp structure takes place, thus introducing imperfections which definitely reduce the TMR ratio. One aim of this work is to investigate whether thin Co interlayer in Fe/MgO/Fe increase the TMR ratios, similar to those ratios predicted with infinite Co leads and comparable with those obtained with CoFeB electrodes.

Nagahama et al. [8] showed that the insertion of Cr films in MTJs with amorphous AlO tunnel barriers and Fe leads exhibits a 2-ML oscillation of the experimental TMR ratio as a function of Cr thickness. A 2-ML oscillation is a signature of a layerwise antiferromagnetic order in the Cr film, in agreement with theoretical findings for Mn buffers [9]. In the latter work, the even-odd effect in the sign of the TMR ratio was attributed to the atomic Mn layer adjacent to the tunnel barrier: its magnetization direction plays a key role in the spin-dependent electronic transport.

Cr couples antiferromagnetically to Fe(001) and shows layerwise AFM order (Fig. 2). In addition, a large magnetic moment is found at the interface with MgO. This finding raises the question whether a single Cr spacer at a single interface produces a defined sign reversal of the TMR ratio.

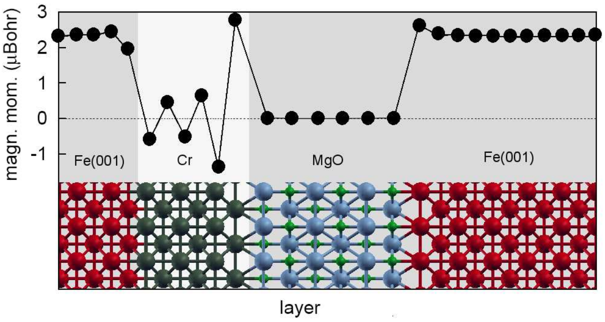

Figure 2. As Figure 1, but for bcc Fe(001)/*x*(Cr)/6MgO/ Fe(001) MTJ with *x* = 6.

THEORETICAL BACKGROUND

In a first step, *ab-initio* electronic-structure calculations were performed within the framework of the local spin-density approximation to density functional theory. The so achieved self-consistent potentials serve as input for the subsequent transport calculations. Both electronic-structure and transport properties are obtained by a Korringa-Kohn-Rostoker multiple-scattering Green's function formalism. Due to its perfect adaptation to the planar geometry a layer-KKR computer code was used for the electronic transport calculations. The self-consistent treatment of the Fe(001)/*x*(Co)/MgO/*x*(Co) /Fe(001) and Fe(001)/ *x*(Cr)/MgO/Fe(001) MTJs, x = 1, …, 7 ML, follows closely those for Fe(001)/MgO/Fe(001) reported in [10]. In particular, atomic positions and interlayer distances were taken from experiment [11]. So, slight changes are expected due to the different atomic volumes of Co and Cr with respect to Fe. The number of MgO layers was fixed for each set-up to 6 ML (corresponding to a thickness of 10.7 Å).

Within the Landauer-Büttiker approach [12], the zero-bias conductance is calculated in terms of the transmittances $T(E)$ at the Fermi level. The latter is computed by integrating the wavevector-resolved transmittances $T(E, k_{||})$ over the two-dimensional Brillouin zone (2BZ) [13], where $T(\mathrm{E}, k_{||})$ is the sum of the transmission probabilities of all Bloch states in the leads. Since both setups exhibit *4mm* symmetry, the number of wavevectors $k_{||}$ in the 2BZ integration was reduced from 80 000 equidistant mesh points to about 10000 of the irreducible part while maintaining the same level of accuracy.

The TMR ratio is expressed by the asymmetry of the conductances for the parallel (G_P) and antiparallel (G_{AP}) magnetic configurations of the Fe electrodes, normalized by the conductance of the AP case (`optimistic TMR ratio').

RESULTS AND DISCUSSION

Co interlayers at both Fe/MgO interfaces

The conductance for the parallel configuration G_P is almost constant with an apparent 2-ML oscillation, with maximum (minimum) conductance for an even (odd) number of x ML. In contrast G_{AP} shows a more complex thickness dependence (Fig. 3). G_{AP} starts approximately two orders of magnitudes smaller than GP at x = 0 ML, but reaches a pronounced maximum an order of magnitude larger at a thickness of two Co layers. For x = 3 – 5 ML it decreases and reaches nearly the level obtained without Co spacers. Another, but some smaller maximum is obtained for one additional Co layer (x = 6 ML). In comparison to the Fe/MgO/Fe MTJ without Co film, a sizably smaller G_P but larger G_{AP} value is achieved for infinite Co electrodes.

The calculated TMR ratios exhibit three noticeable characteristics. Firstly, 3 and 5 ML thick Co interlayers lead to huge TMR ratios: 10000% at 3 ML and 15700% at 5 ML – which are significantly larger than the 6800% obtained without Co spacers (indicated by the green horizontal line in Fig. 3). Secondly, the TMR at 2 ML Co drops as a consequence of the large G_{AP} value, caused by interface resonances, nearly to zero. Thirdly, a much smaller TMR value is calculated for infinite Co leads in comparison to that determined with pure Fe leads, a finding in contrast to results reported in [7]. This may be related to differences in the geometries. Previous investigations of Fe/MgO/Fe systems have shown that slightly differing atomic positions in the interface region can lead to sizably different conductances and TMR ratios.

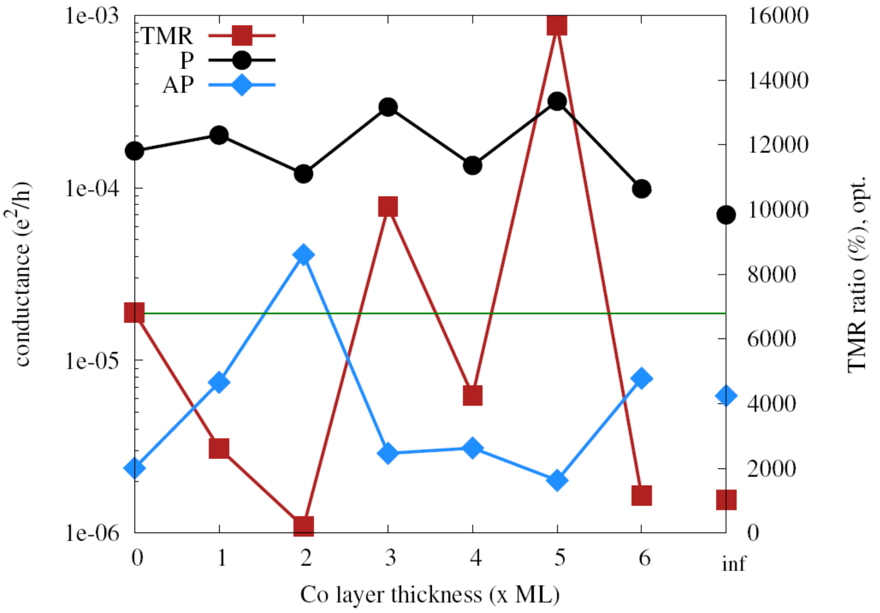

Figure 3. Conductances for the P (black circles) and AP (blue diamonds) magnetic configurations of Fe/x(Co)/MgO/x(Co)/Fe versus Co thickness. The `optimistic' TMR ratio is shown as red squares. Results for Co electrodes, replacing the Fe electrodes are shown in addition (`inf').

Cr interlayers at one Fe/MgO interface

Fig 4a. displays in analog to Fig 3., the thickness dependence of the P and AP conductance with up to 7 Cr layers. Both, G_P and G_{AP} exhibit an exponential decay as a function of the Cr thickness x. The G_P decay rate is hereby visibly larger than that one for G_{AP}.

G_P and G_{AP} reveal superimposed to the exponential decay, even-odd oscillations that are in antiphase. These characteristics can be traced back to the layer-wise antiferromagnetism of the Cr layers. In Fig 2. the exemplary case with $x = 6$ ML shows that Cr couples layer-wise antiferromagnetically to the Fe(001) substrate. It turns out and can be seen too in Fig 2. that the magnetic layer at the Cr/MgO interface possesses the largest uncompensated local magnetic moment of the Cr spacer. It can be deduced from previous tunnel magneto-resistance investigations with layer-wise antiferromagnetic Mn films [9] that the Cr film acts generally as a spin-filter for the electron currents. But the decisive influence which changes the spin-polarization of the currents can be directly addressed to the magnetic atom adjacent to the MgO barrier.

With help of Fig 4b, which displays the local magnetizations of these interface layers, it is clear that an even number of Cr layers leads to a positive local magnetic moment which results directly in local maxima (minima) for G_P (G_{AP}). Vice versa, negative local moments for odd Cr layers cause a local maxima (minima) for G_{AP} (G_P).

The periodic maxima and minima of G_P and G_{AP} cause a pronounced even-odd effect with periodic changes of $G_P > G_{AP}$ and $G_P < G_{AP}$. Consequently, this results in an oscillation of the TMR ratio shown in Fig 4a. This oscillation with a period of 2-ML is connected to a periodic sign reversal of the TMR ratio.

The TMR ratio with no Cr spacer is about 6800%. This order of magnitude shows up again only for a Cr thickness of 2 monolayers. In particular we would like to emphasize that the TMR value of approximately 8200% is larger than that one found for Fe/MgO/Fe MTJs without any Cr interlayers. The TMR ratio for 1 ML is strongly reduced about two orders of magnitude. Apart from the large amplitude for 2 ML, this reduced level is reached and maintained – alternating between about plus-or-minus 100% – for all thicker Cr films.

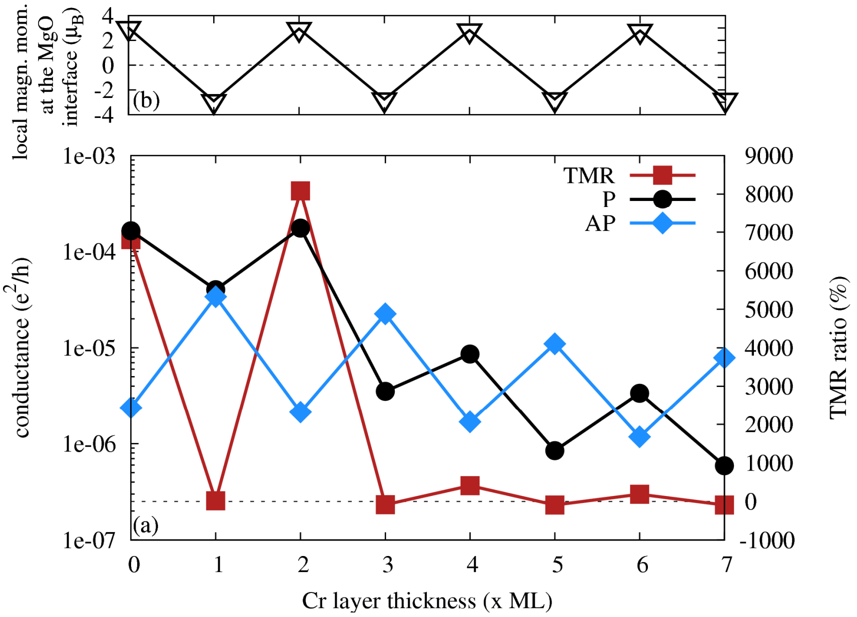

Figure 4. (a) As Figure 3, but for Fe/x(Cr)/MgO/Fe versus Cr thickness. (b) Local magnetic moment of the magnetic layer at the interface for each Cr thickness x.

CONCLUSIONS

Bcc Co interlayers at both interfaces of Fe/MgO/Fe junctions do not *per se* improve TMR ratios as compared to Fe/MgO/Fe junctions. Only specific Co thicknesses, namely 3 and 5 ML, result in larger TMR ratios.

The insertion of a single, layer-wise antiferromagnetic Cr buffer causes 2-ML oscillations of the conductances as a function of the Cr thickness, which show up as an even-odd change of the TMR's sign. The TMR ratio is generally, compared to the case with no Cr spacer, reduced about two orders of magnitude. Only a 2 ML thick Cr spacer is found to reproduce a sizeable larger TMR ratio.

ACKNOWLEDGEMENTS

One of us (PB) acknowledges support by the International Max Planck Research School for Science and Technology of Nanostructures. We thank R. Matsumoto and S. Yuasa (AIST, Tsukuba, Japan) for fruitful discussions.

REFERENCES

[1] S. Yuasa, and D. D. Djayaprawira, J. Phys. D: Appl. Phys. **40** (2007), R337-R354
[2] P. Bose, A. Ernst, I. Mertig, and J. Henk, Phys. Rev. B **78**, 092403 (2008)
[3] W. H. Butler, X.-G. Zhang,T. C. Schulthess and J. M. MacLaren, Phys. Rev. B **63**, 054416 (2001)
[4] J. Mathon and A. Umerski, Phys. Rev. B **63**, 220403 (2001)
[5] S. Yuasa, T. Nagahama, A. Fukushima, Y. Suzuki, and K. Ando, Nat. Mat. **3**, 868 (2004)
[6] Parkin et al., Nat. Mat. **3**, 862 (2004)
[7] X.-G. Zhang and W. H. Butler, Phys. Rev. B **70**, 172407, (2004)
[8] T. Nagahama, S. Yuasa, E. Tamura, and Y. Suzuki, Phys. Rev. Lett. **95**, 086602, (2005)
[9] P. Bose**,** I. Mertig, and J. Henk, Phys. Rev. B **75**, 100402(R) (2007)
[10] Ch. Heiliger, P. Zahn, B. Yu. Yavorsky and I. Mertig, Phys. Rev. B **73**, 214441 (2006)
[11] Ch. Tusche et al., Phys. Rev. Lett. **96**, 119602 (2006)
[12] Y. Imry and R. Landauer, Rev. Mod. Phys. **71**, S306 (1999)
[13] J. M. MacLaren, X.-G. Zhang, W. H. Butler and X. Wang Phys. Rev. B **59**, 5470 (1999)

Tailoring tunnel magnetoresistance by ultrathin Cr and Co interlayers: A first-principles investigation of Fe/MgO/Fe junctions

Peter Bose,[1, 2] Peter Zahn,[1] Jürgen Henk,[3] and Ingrid Mertig[1, 3]
[1]*Martin Luther University Halle-Wittenberg, Institute of Physics, D-06099 Halle (Saale), Germany*
[2]*International Max Planck Research School for Science and Technology of Nanostructures, Weinberg 2, D-06120 Halle (Saale), Germany*
[3]*Max Planck Institute of Microstructure Physics, Weinberg 2, D-06120 Halle (Saale), Germany*

(Dated: January 13, 2010)

We report on systematic ab-initio investigations of Co and Cr interlayers embedded in Fe(001)/MgO/Fe(001) magnetic tunnel junctions, focusing on the changes of the electronic structure and the transport properties with interlayer thickness. The results of spin-dependent ballistic transport calculations reveal options to specifically manipulate the tunnel magnetoresistance ratio. The resistance area products and the tunnel magnetoresistance ratios show a monotonous trend with distinct oscillations as a function of the Cr thickness. These modulations are directly addressed and interpreted by means of magnetic structures in the Cr films and by complex band structure effects. The characteristics for embedded Co interlayers are considerably influenced by interface resonances which are analyzed by the local electronic structure.

PACS numbers: 72.25.Mk, 73.22.-f, 73.40.Gk, 75.47.-m

I. INTRODUCTION

During the last years magnetoresistive effects — in particular the tunnel magnetoresistance (TMR) effect[1,2] — became increasingly important for the fast developing field of spintronic devices[3,4]. The first industrial applicable TMR contacts have been built using crystalline MgO insulators which are epitaxially grown on as well as coated with iron electrodes[5,6]. Fe/MgO/Fe magnetic tunnel junctions (MTJs) have been extensively investigated to elucidate the mismatch between theoretically predicted[7,8] and the at least one order of magnitude smaller measured[9,10] TMR ratios. It turned out that the disparity can be attributed to differences between idealized (in theory) and real (in experiment) samples. More sophisticated theories which include imperfections, like interface disorder[11–17] or roughness effects[18], were able to close the gap between experiment and theory and highlight the importance of perfect interfaces.

Although other tunnel junctions, like CoFeB/MgO/CoFeB MTJs with their high TMR ratios[19], were put into the focus of attention, Fe/MgO/Fe MTJs are still intensely studied. Besides the emerging field of spin-torque effects[20], research is ongoing in search of other ways to increase the TMR ratio further. Instead of improving the interface quality an alternative means is found in the specific manipulation of the spin-dependent conductances by embedding ultrathin interlayers[21,22].

The insertion of a single layer-wise antiferromagnetic (LAFM) Cr interlayer results into even-odd oscillations of the TMR ratio as a function of the Cr thickness[23,24]. In this paper we report on a first-principles study of these transport characteristics. We discuss the origin of these modulations with the apparent 2 ML-wavelength as well. Additionally, an analysis of the electronic transport results for Co interlayers at both Fe/MgO interfaces is presented. These investigations were motivated by previous ab-initio calculations[25] which predicted larger TMR ratios for MgO tunnel junctions with bcc Co(001) leads instead of Fe(001) electrodes. Due to the fact that Co grows epitaxially only up to a few monolayers on bcc substrates, a question arises whether ultrathin Co interlayers could be alternatively used to obtain an enhancement of the TMR ratios in Fe/MgO/Fe MTJs. To answer this question we computed the conductances and TMR ratios for small Co interlayer thicknesses and analyzed the results by means of the electronic structures.

II. THEORETICAL BACKGROUND

Our computational approach is divided into two steps. Firstly, the electronic structures of the MTJs are calculated from first principles. Secondly, the electronic transport properties are computed, using the potentials obtained in the first step.

The electronic structure is determined self-consistently within the framework of density-functional theory (DFT) using a scalar-relativistic screened Korringa-Kohn-Rostoker (KKR) Green function technique[26,27]. The spherical site potentials were treated in the atomic sphere approximation (ASA) using the local spin density approximation (LSDA) for the exchange-correlation potential[28]. Throughout this work a parameterization following Vosko, Wilk, and Nusair[29] was used.

Since structural information of Fe/MgO/Fe MTJs with embedded ultrathin Cr and Co spacers are not reported so far, we resort to a geometry of planar Fe(001)/MgO/Fe(001) junctions which has been determined experimentally by surface x-ray diffraction analyses[30,31]. This structure has been used in previous theoretical studies[16,32]. In detail, a supercell geometry with six MgO layers sandwiched by 20 Fe layers was used to compute self-consistently the atomic potentials. The insertion of x magnetic interlayers in planar Fe(001)/x(Cr)/6(MgO)/Fe(001) and Fe(001)/x(Co)/6(MgO)/x(Co)/Fe(001) junctions was achieved by replacing x Fe monolayers (ML) at the Fe/MgO interfaces by x Cr or Co layers. This procedure implies that Cr and Co atoms occupy the same positions as the replaced Fe atoms; worded differently, the interlayers follow the bcc structure of the Fe(001) leads.

Due to the broken translational invariance in transport direction (z, i. e. [001]) and the in-plane translational invariance, the eigenstates of the electrodes are labeled by in-plane wave vectors $\boldsymbol{k}_{||} = (k_x, k_y)$. The point group of the two-dimensional lattice is $4mm$.

The ballistic conductance C per unit cell area $A_\square$ is computed for zero bias voltage in terms of transmission probabilities (Landauer-Büttiker approach[33]) at the Fermi energy E_F,

$$C = \frac{e^2}{h} \int_{2\mathrm{BZ}} T(\boldsymbol{k}_{||}, E_F) d\boldsymbol{k}_{||}. \tag{1}$$

The transmission probability $T(\boldsymbol{k}_{||}, E_F)$ is obtained by means of a Green function approach[34]. The integration over the two-dimensional Brillouin zone (2BZ) requires typically about 90 000 $\boldsymbol{k}_{||}$. The use of special $\boldsymbol{k}_{||}$ points[35] reduces that number to 1/8. The resistance area product

$$RA = \frac{1}{C}, \tag{2}$$

as normalized quantity, is used to compare the theoretical with experimental data.

The optimistic TMR ratio is obtained from the RAs which are computed for the parallel (P) and the antiparallel (AP) alignment of the two Fe(001) lead magnetizations,

$$\mathrm{TMR} = \frac{RA^{\mathrm{AP}} - RA^{\mathrm{P}}}{RA^{\mathrm{P}}}. \tag{3}$$

For the normalized TMR ratio the denominator is replaced by $RA^{\mathrm{AP}} + RA^{\mathrm{P}}$. Since interfaces determine considerably the transport properties, transmittance maps which display $T(\boldsymbol{k}_{||}, E_F)$ versus $\boldsymbol{k}_{||}$ need to be interpreted by means of the local electronic structure, rather than by the electronic structures of the bulk electrodes. The former is obtained from the layer-resolved Bloch spectral density (SD)

$$N_{al}(E, \boldsymbol{k}_{||}) = -\frac{1}{\pi} \mathrm{Im} \mathrm{Tr} G^{+}_{al}(E, \boldsymbol{k}_{||}), \tag{4}$$

of atom a in layer l. $G^{+}_{al}(E, \boldsymbol{k}_{||})$ is the site-diagonal Green function of that site. The trace involves integration over the ASA sphere and summation over spin-angular quantum numbers.

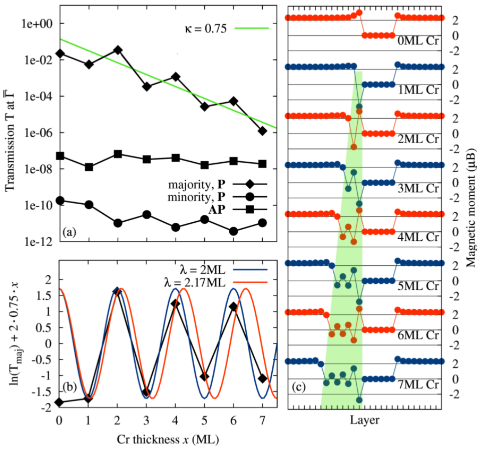

Figure 1: (Color) (a) Dependence of spin-resolved P (majority, minority) and AP transmissions on a logarithmic scale versus Cr thickness x for Bloch states at $\boldsymbol{k}_{||} = 0$ in Fe(001)/x(Cr)/6(MgO)/Fe(001) MTJs, $x = 0, \ldots, 7$. The green line is a fitted exponential to the majority transmission. The deviation of the majority transmission from this fit is shown in panel (b). These data are fitted by cosine functions (fixed at $x = 1$) with 2 ML (blue) and 2.17 ML (red) periods. (c) Magnetic profiles of MTJs with Cr layer thicknesses $x = 0, \ldots, 7$ ML. The green area highlights the magnetic moments of the Cr layers.

III. RESULTS

A. Cr interlayer in Fe(001)/MgO/Fe(001)

In the following we present results of the thickness dependence of both the conductances and the TMR ratios for ultra-thin Cr interlayers which are embedded at a single interface in Fe(001)/x(Cr)/6(MgO)/Fe(001) MTJs. The Cr thickness d_{Cr} is varied in steps of monolayers (ML), $x = 0, \ldots, 7$ with $d_{\mathrm{Cr},1\,\mathrm{ML}} = 2.35\,$Å, $d_{\mathrm{Cr},2\,\mathrm{ML}} = 4.04\,$Å and $d_{\mathrm{Cr},x\,\mathrm{ML}} = d_{\mathrm{Cr},2\,\mathrm{ML}} + x \cdot 1.69\,$Å.

We start with the tunneling behavior of Bloch states at $\bar{\Gamma}$ ($\boldsymbol{k}_{||} = 0$). The associated transmission probabilities for $x = 0, \ldots, 7$ are plotted in Fig. 1a. Both the minority spin contribution for P and the AP contribution stay almost constant, whereas the majority spin contribution of P decays exponentially with an oscillatory modulation. Its decay rate is estimated by an exponential fit, $\exp(-2\kappa x)$ with $\kappa = 0.75$ (green line in Fig. 1a).

It turns out that an oscillatory modulation of $T^{\mathrm{P}}_{\mathrm{maj}}$ shows up for all $\boldsymbol{k}_{||}$ within the 2BZ. These oscillations are also present in the conductance C which is an integral over the transmission probabilities, eq. (1); hence, there is no destructive interference which would lead to (complete) cancellation. Thus, it is essential to eluci-

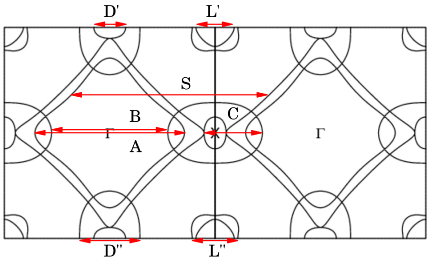

Figure 2: (Color online) Fermi surface cross sections in the (100) plane of commensurate AFM Cr (c-afm). The nesting vectors along [001] (arrows) are shown in an extended zone scheme and are listed in Table I.

Table I: Nesting vectors of commensurate AFM (c-afm) Cr along [001], as given in Fig. 2, are characterized by their oscillation periods (in ML).

c-afm	L'	L"	S	A	B	C	D'	D"
λ[ML]	11.03	9.21	2.12	2.82	3.62	7.21	13.26	6.96

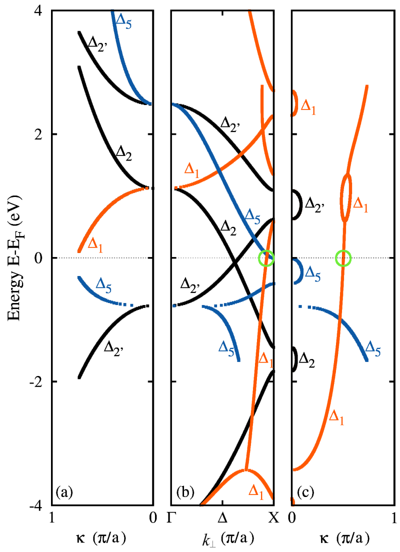

Figure 3: (Color) Complex bandstructure of bulk bcc Cr in the commensurate AFM (c-afm) phase along [001] for $\boldsymbol{k}_{||} = 0$. The real part of $k_\perp$ and the exponential decay rate κ (imaginary part of $k_\perp$) are shown in panels (b) and (a, c), respectively. The color code of the bands indicates the irreducible representations of the point group $4mm$ of the associated Bloch states. The green circles at the Fermi energy mark the complex Δ_1-band of second kind, to $k_\perp = (0.922, 0.503)^{\pi}/_{a}$, which governs the transmission of majority electrons at $\bar{\Gamma}$ (cf. Fig. 1a).

date the underlying mechanism of these oscillations. To strengthen the discussion we focus in the following on the transmissions at $\bar{\Gamma}$.

The oscillation period can be estimated by fitting cosine functions to the deviation of $T^{\mathrm{P}}_{\mathrm{maj}}(\boldsymbol{k}_{||} = 0)$ from the averaged exponential decay (black diamonds in Fig. 1b). The fit with a period of 2 ML (blue) reproduces only the peak positions but deviates significantly in amplitude. A second fit, with 2.17 ML period (red), hits the data best.

The 2 ML oscillation can be explained by the local magnetic structure of the layer-wise antiferromagnetic (LAFM) Cr interlayers (Fig. 1c). The magnetic moments of the Cr layers at the Cr/MgO interface is sizably enhanced due to the nonmagnetic MgO film. As a consequence of these partially uncompensated magnetic moments, the Cr interface layers act as spin filters for the tunnel currents. Hence, the latter are increased (decreased) if the magnetic moments within the Cr interface layers are parallel (anti-parallel) to the magnetization of the opposite Fe electrode. Due to the LAFM growth of the Cr interlayer the tunnel current characteristics should exhibit signatures of 2 ML oscillations. The maxima of these oscillations should arise for P (AP) magnetic configurations of the Fe leads at even (odd) multiples of the Cr interlayer thickness x. This behaviour was already found for LAFM Mn interlayers in Fe(001)/x(Mn)/Vac/Fe(001) MTJs[36]. However, the mismatch in Fig. 1b appears like an undersampling which cannot be satisfactorily explained by means of the spin filter effect. The better match of the other oscillation period with 2.17 ML points to another effect which additionally influences the electronic transport.

There are two possible mechanisms that may explain other wavelengths than the 2 ML. Firstly, one could think of spin-density waves within the Cr interlayers. Spin-density waves are found for Cr bulk systems[37] and are related to nesting vectors of the Fermi surface. Nesting vectors that come into question are shown in Fig. 2 for a cross section of the Fermi surface in the (100) plane. The corresponding wavelengths of these vectors along the [001] direction (i. e. in transport and growth direction) are given in Table I. The only vector that exhibits a wavelength which is comparable to that of the transmission (2.17 ML) is S, with an oscillation period of 2.12 ML. However, since we are interested in the oscillatory onset at $\boldsymbol{k}_{||} = 0$, the vector S cannot explain our findings because it is offset from $\bar{\Gamma}$.

The oscillatory exponential decay of $T^{\mathrm{P}}_{\mathrm{maj}}(\boldsymbol{k}_{||} = 0)$ is explained most promisingly in terms of the complex bandstructure[38] of the Cr interlayers. Since a (continuous) dispersion relation is not defined for thin films, due to lack of translational invariance, we refer to the complex bandstructure of bulk Cr along [001]. The latter is decomposed with respect to the irreducible representa-

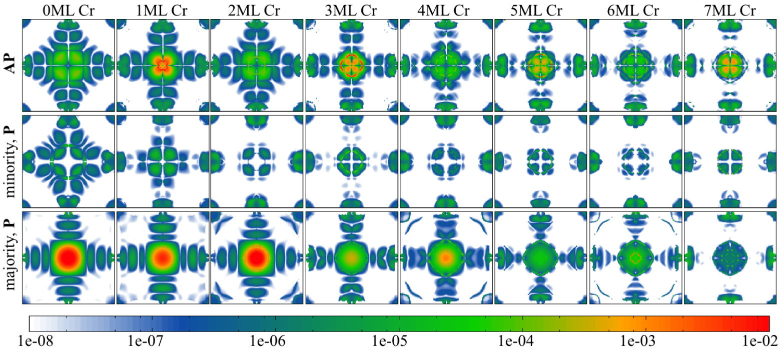

Figure 4: (Color online) Majority (P, bottom row), minority (P, middle row) and AP (top row) transmission $T(\boldsymbol{k}_{||}, E_F)$ within two-dimensional Brillouin zones for Fe(001)/x(Cr)/6(MgO)/Fe(001) MTJs with Cr layer thicknesses of $x = 0, \ldots, 7$ ML (from left to right). The two-dimensional Brillouin zones cover the range between $-\pi/a$ and π/a.

tions of the point group $4mm$ (Δ_1, Δ_5, Δ_2 and $\Delta_{2'}$) of the associated Bloch states (Fig. 3).

A complex band structure of a periodic system is the conventional band structure extended to Bloch vectors $(\boldsymbol{k}_{||}, k_\perp)$ with complex wave numbers $k_\perp$. The associated bands can be cast into four categories[39]: (i) *real bands* which correspond to the conventional band structure and have $\mathrm{Im}k_\perp = 0$; (ii) *imaginary bands of the first kind* have $\mathrm{Re}k_\perp = 0$ and $\mathrm{Im}k_\perp \neq 0$; (iii) *imaginary bands of the second kind* with $\mathrm{Re}k_\perp = \pi/a$ and $\mathrm{Im}k_\perp \neq 0$; and (*iv*) *complex bands* with $\mathrm{Re}k_\perp \neq 0$, $\mathrm{Re}k_\perp \neq \pi/a$ and $\mathrm{Im}k_\perp \neq 0$.

The imaginary part of $k_\perp$ is denoted as κ and represents a measure for the decay rate of evanescent Bloch states[43]. At the Fermi energy, a complex band of the second kind shows up at $k_\perp = (0.922, 0.503)\pi/a$ (circles in Fig. 3). The corresponding decay rate of $\kappa = 0.78/\mathrm{ML}$ matches well the estimated exponential decay of the majority transmission ($\kappa = 0.75/\mathrm{ML}$, Fig. 1a). Due to the nonvanishing real part the exponential decay exhibits an oscillatory envelope with a wavelength $\lambda = \pi/\mathrm{Re}[k_\perp] \approx 2.17$ ML which agrees well with the fit in Fig. 1b. We conclude therefore that the thickness dependence of the transmission for the majority states at the $\bar{\Gamma}$ point is very likely governed by this Δ_1 state, provided the electronic structure of ultra-thin Cr films is well described by that of bulk Cr.

Transmission maps display the spin-resolved transmission for P and AP versus $\boldsymbol{k}_{||}$ for each Cr thickness x (Fig. 4). As observed for $T^{\mathrm{P}}_{\mathrm{maj}}(\boldsymbol{k}_{||} = 0)$ one finds within the majority transmission maps a clearly visible modulation of $T^{\mathrm{P}}_{\mathrm{maj}}(\boldsymbol{k}_{||})$ for $\boldsymbol{k}_{||}$-points in the center regions with maxima (minima) at even (odd) multiples of x. It is reasonable to assume that the oscillations of these transmissions are caused by the same bandstructure effect as it was discussed for $T^{\mathrm{P}}_{\mathrm{maj}}$ at $\bar{\Gamma}$. Furthermore, the majority RA products in Fig. 5 exhibit even-odd oscillations as well, indicating constructive superposition of the oscillations of the individual $T^{\mathrm{P}}_{\mathrm{maj}}(\boldsymbol{k}_{||})$.

Although the cloverleaf-like structures within the mi-

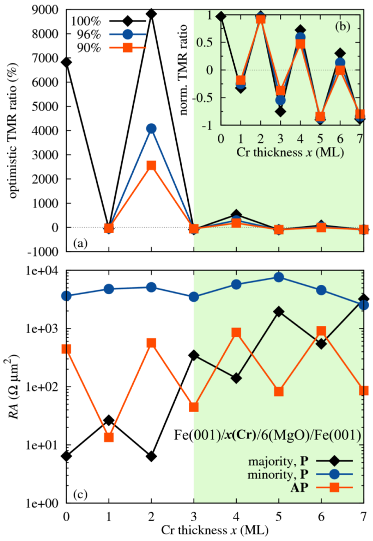

Figure 5: (Color online) Cr thickness dependence of (a) optimistic and (b) normalized TMR ratios in Fe(001)/x(Cr)/6(MgO)/Fe(001) MTJs. Since variations of the Cr layer thickness cannot be ruled out in experiment, a model with resistors in parallel connection is assumed to mimic Cr-thickness fluctuations (line styles indicate the weight w; see text). (c) Resistance area product RA for parallel magnetic (P: majority, minority) and anti-parallel magnetic configurations (AP), shown on a logarithmic scale.

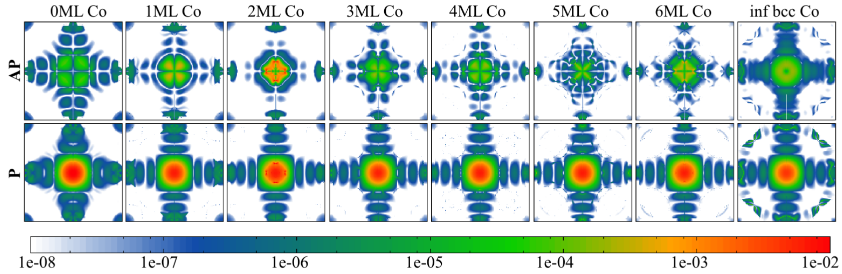

Figure 6: (Color online) Transmission $T(\boldsymbol{k}_{||}, E_F)$ for the P (bottom row) and AP (top row) magnetic configuration within two-dimensional Brillouin zones for Fe(001)/x(Co)/6(MgO)/ x(Co)/Fe(001) MTJs, $x = 0, \ldots, 6$ ML (from left to the right). The panels on the right hand side are for Co(001)/6(MgO)/Co(001) MTJs with infinite bcc Co leads. The Brillouin zones cover the range between $-\pi/a$ and π/a.

nority transmission maps in Fig. 4 exhibit slight variations which are in anti-phase to the majority transmission modulations, the corresponding RA products in Fig. 5 reveal no signatures of such an even-odd characteristic. The weak thickness dependence can be understood with help of the complex bandstructure in Fig. 3. From first-principles investigations on Fe/MgO/Fe it is known[40,41] that Δ_5 states are the main carrier within the minority transport channel. Due to the Δ_5 *real band* at the Fermi energy it is very likely that these Bloch states just propagate undamped through the Cr interlayer. The minority RA is therefore marginally affected by the Cr spacer and gives contributions which are similar to those of Fe/MgO/Fe MTJs.

In contrast to the above finding, the pronounced modulations within the AP transmission maps in Fig. 4 — with maxima (minima) at odd (even) x — lead to an even-odd oscillation of the corresponding RA. Due to the spin-filter effect of the Cr interface layer RA^{AP} is in anti-phase to $RA^{\mathrm{P}}_{\mathrm{maj}}$. This behavior results in TMR ratios which exhibit 2 ML oscillations with periodic changes of the sign. The amplitudes of the TMR ratios, are with about 7000 % and 9000 % at $x = 0$ ML and 2 ML, considerably larger than for the other thicknesses, with values between about -100 % and $+100$ %. This even-odd oscillation of the TMR ratio as a function of the Cr thickness has been observed experimentally[24] but with a phase shift of 1 ML. In more recent experiments[44] it has been found that this phase shift depends on whether the Cr interlayer is grown after or before growth of the MgO barrier. However, a large maximum of the TMR ratio for small Cr thicknesses does not show up in both growth conditions. Instead, an exponential decay of the optimistic TMR ratio for increasing x is reported[24]. Since variations of the Cr layer thickness cannot be ruled out in experiment, we assume a model with resistors in parallel connection to mimic Cr-thickness fluctuations. The resistance of the mean thickness x is weighted by w, the contributions from $x-1$ and $x+1$ are weighted by $(100\,\% - w)/2$, respectively. With already large central weights of $w = 96$ % and $w = 90$ % this model is able to reproduce the principal experimental TMR characteristics[24]. For a detailed analysis of the effect of structural imperfections, however, one has to rely on more sophisticated computational approaches, like the coherent potential approximation or a supercell method.

B. Fe(001)/ x(Co)/ 6(MgO)/ x(Co)/ Fe(001)

In this section we discuss the effects of Co interlayers embedded into Fe(001)/MgO/Fe(001) MTJs on the electronic transport. With respect to previous theoretical investigations of MgO barriers with bcc Co leads[25] we specifically studied the thickness dependence of ultrathin Co interlayers which are inserted at *both* Fe/MgO interfaces. Since Co grows epitaxially only up to few ML on a bcc substrate, the Co thicknesses d_{Co} are restricted to $x \leq 6$ ML. The monolayer separations are taken identical to the case of Cr interlayers. Substituting all Fe atoms with Co atoms the effect of semi-infinite bcc Co leads is studied in addition.

First, we recall previously reported conductances and TMR ratios in MTJs with equal thickness variations of both Co interlayers[42]. The corresponding $\boldsymbol{k}_{||}$-resolved transmissions versus x are shown in Fig. 6 for both magnetic configurations (P, AP). The shapes of the transmission maps for P configuration (bottom row) are — beside the case of the semi-infinite Co leads — very similar. In contrast to this weak dependence, one observes a rise and a decline of the transmission probabilities in the central regions of the Brillouin zones for the AP configuration for small x (top row). The maximum shows up at $x = 2$ ML. Based on these observations it is reasonable to expect a relatively constant behavior of the P conductance and a maximum at $x = 2$ ML for the AP conductance.

The elsewhere published conductances and TMR ratios[42] are inserted into Fig. 7 as red boxes. In accordance with the findings for bcc Co leads[25], we identify specific Co thicknesses ($x = 3$ ML and 5 ML) that ex-

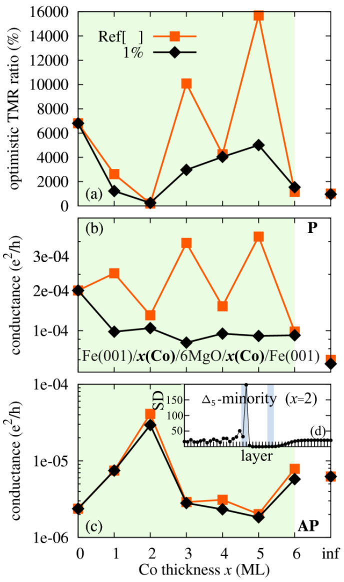

Figure 7: (Color) Co thickness dependence of (a) optimistic TMR ratio, P (b), and AP (c) conductances in symmetric Fe(001)/x(Co)/6(MgO)/x(Co)/Fe(001) MTJs. Red squares, taken from Ref. 42, are for data which exhibit hotspots in the transmission probabilities $T(\boldsymbol{k}_{||}, E_F)$. The black symbols show the data with these hot spots being removed (see text). Panel (d) displays the layer-resolved spectral density (in states/Hartree) of a Δ_5-minority interface resonance with $\boldsymbol{k}_{||} = (0.095, 0.008)^{\pi}/_{a}$. The blue areas mark the position of the 2 ML thick Co interlayers within the MTJ.

hibit larger TMR values than those obtained for pure Fe/MgO/Fe junctions. In particular, the TMR ratio follows the even-odd type characteristic which shows up for the conductance C^{P}. But, this behavior of C^{P} does not reflect the weak thickness dependence as expected from the transmission probabilities (Fig. 6). It turned out that this even-odd change is considerably affected by single interface resonances whose transmission probabilities contribute with up to 70 % to the conductance. These hot spots within the transmission maps occur preferably in ideal, symmetric MTJs at zero bias voltage[21]. They are strongly diminished by breaking the symmetry, for instance by means of a tiny bias voltage or structural imperfections of the sample. A bias voltage of 0.02 V is sufficient to destroy the resonant states and to reduce the corresponding transmission probabilities by several orders of magnitude.

The total number of hot spots in each transmission map of Fig. 6 is less than 10. Instead of removing the resonances by a small bias voltage, the transmissions of these states are identified and neglected. These filtered data are shown as black diamonds in Fig. 7. The effect of the resonances shows up mainly for C^{P}. For the latter one obtains, after an initial decrease of about 50 % from $x = 0$ ML to 1 ML, the expected nearly constant behavior.

The filtered AP conductances agree well with unfiltered ones, in particular the maximum at $x = 2$ ML. Inspecting the corresponding transmission map (Fig. 6), this maximum is attributed to enhanced transmissions in the center region of the 2BZ which are caused by Δ_5-minority interface resonances within the Co interface layer (Fig. 7d). In contrast to the transmission resonances (hot spots), these transmissions are unaffected by small bias voltages.

Since the thickness dependence of C^{P} is weakened by the filter procedure, that of the TMR ratio is as well. In particular, the maxima at $x = 3$ ML and 5 ML do not show up. The minimum of approximately 200% at $x = 2$ ML is, however, still present; it is explained by the increase of C^{AP} — up to a value comparable with C^{P} — due to the Δ_5-minority interface resonances. For increasing x the TMR ratio increases monotonously up to a maximum at $x = 5$ ML, with 4600 % considerably smaller than the 7000 % obtained for pure Fe/MgO/Fe MTJs.

We note in passing that the enhanced TMR ratio in MTJs with semi-infinite bcc Co leads, reported in

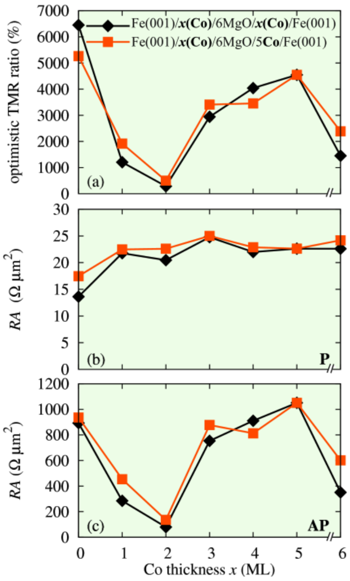

Figure 8: (Color) Optimistic TMR ratios (a) and resistance-area products RA for P (b) and AP (c) of symmetric (black) and asymmetric (red) Fe(001)/x(Co)/6(MgO)/y(Co)/Fe(001)MTJs. Hot spots were filtered out (see e. g. Fig. 7).

Ref. 25, are not reproduced. Previous investigations of Fe/MgO/Fe systems have shown that conductances depend strongly on details of the calculations, in particular on the atomic positions in the interface region. Thus, one is lead to attribute the above mentioned discrepancy to computational details.

Since increased TMR ratios are not obtained by symmetric MTJs, we studied the effect of asymmetric MTJs, with one interlayer thickness fixed to 5 ML, in addition. The fixed thickness of 5 ML is chosen with respect to the largest TMR ratio in symmetric MTJs (Fig. 7). Both the RA products and the TMR ratios of the asymmetric junctions do not differ significantly from those of the symmetric junctions (Fig. 8). For both kinds of MTJs, the TMR ratio follows the characteristics of RA^{AP} because RA^{P} is almost constant. The presence of the minimum at $x = 2\,\mathrm{ML}$ additionally substantiates that the Δ_5-minority interface resonances, which cause the drop of RA^{AP}, are marginally affected by symmetry breaking of an ideal MTJ.

IV. CONCLUSION

In summary, the computed conductances and TMR ratios exhibit the oscillatory decays for thickness variations of ultrathin Cr interlayers, which have been found in experiment. The analysis of the associated transmission probabilities reveals that the tunneling of Bloch states is affected by the interplay of two mechanisms. On the one hand a spin-filter effect which is induced by the enhanced magnetic moments of the Cr interface layers and on the other hand the presence of complex bands which are formed within the Cr interlayers. The oscillations are therefore mixtures of 2 ML oscillations of magnetic origin and superpositions of the individual modulations of the tunneling Bloch states, which can be traced back to the corresponding complex wave vectors. Our results further indicate that spin-density waves are of minor importance for understanding of electronic transport through Fe/MgO/Fe MTJs with ultrathin Cr interlayers.

The embedding of Co interlayers at both interfaces does not lead to an increase of the TMR ratios with respect to Fe/MgO/Fe MTJs. Please note that the reference values for $x = 0$ (i.e. no Co interlayer) have been calculated under the assumption of ideal interface structures and are therefore probably considerably overestimated. Thus, we suggest to include the effects of imperfect interfaces, which are unavoidable in real samples, in a future investigation.

Acknowledgments

Helpful discussions with S. Yuasa, R. Matsumoto, and N. F. Hinsche are gratefully acknowledged. This work is supported by the Sonderforschungsbereich 762, Functionality of Oxidic Interfaces. P. B. is supported by the International Max Planck Research School for Science and Technology of Nanostructures.

---

[1] M. Julliere, Physics Letters A **54**, 225 (1975), ISSN 0375-9601.
[2] J. S. Moodera, L. R. Kinder, T. M. Wong, and R. Meservey, Physical Review Letter **74**, 3273 (1995).
[3] I. Žutić, J. Fabian, and S. Das Sarma, Reviews of Modern Physics **76**, 323 (2004).
[4] S. A. Wolf, A. Y. Chtchelkanova, and D. M. Treger, IBM J. Res. Dev. **50**, 101 (2006), ISSN 0018-8646.
[5] W. J. Gallagher and S. S. P. Parkin, IBM J. Res. Dev. **50**, 3 (2006).
[6] S. Yuasa and D. D. Djayaprawira, Journal of Physics D: Applied Physics **40**, R337 (2007).
[7] W. H. Butler, X.-G. Zhang, T. C. Schulthess, and J. M. MacLaren, Physical Review B **63**, 054416 (2001).
[8] J. Mathon and A. Umerski, Phys. Rev. B **63**, 220403 (2001).
[9] S. Yuasa, T. Nagahama, A. Fukushima, Y. Suzuki, and K. Ando, Nature Materials **3**, 868 (2004).
[10] S. S. P. Parkin, C. Kaiser, A. Panchula, P. M. Rice, B. Hughes, M. Samant, and S.-H. Yang, Nat Mater **3**, 862 (2004), ISSN 1476-1122.
[11] X.-G. Zhang, W. H. Butler, and A. Bandyopadhyay, Physical Review B **68**, 092402 (2003).
[12] J. Mathon and A. Umerski, Physical Review B **74**, 140404 (2006).
[13] H. Itoh, J. Ozeki, and J. Inoue, Journal of Magnetism and Magnetic Materials **303**, e205 (2006).
[14] D. Waldron, V. Timoshevskii, Y. Hu, K. Xia, and H. Guo, Physical Review Letters **97**, 226802 (2006).
[15] C. Heiliger, P. Zahn, and I. Mertig, Journal of Magnetism and Magnetic Materials **316**, 478 (2007).
[16] P. Bose, A. Ernst, I. Mertig, and J. Henk, Physical Review B **78**, 092403 (2008).
[17] F. Bonell, S. Andrieu, A. M. Bataille, C. Tiusan, and G. Lengaigne, Physical Review B **79**, 224405 (2009).
[18] P. X. Xu, V. M. Karpan, K. Xia, M. Zwierzycki, I. Marushchenko, and P. J. Kelly, Phys. Rev. B **73**, 180402 (2006).
[19] S. Ikeda, J. Hayakawa, Y. Ashizawa, Y. M. Lee, K. Miura, H. Hasegawa, M. Tsunoda, F. Matsukura, and H. Ohno, Applied Physics Letters **93**, 082508 (2008).
[20] R. Matsumoto, A. Fukushima, K. Yakushiji, S. Yakata, T. Nagahama, H. Kubota, T. Katayama, Y. Suzuki, K. Ando, S. Yuasa, et al., Phys. Rev. B **80**, 174405 (2009).
[21] K. D. Belashchenko, J. Velev, and E. Y. Tsymbal, Physical Review B **72**, 140404 (2005).
[22] F. Greullet, C. Tiusan, F. Montaigne, M. Hehn, D. Halley, O. Bengone, M. Bowen, and W. Weber, Phys. Rev. Lett. **99**, 187202 (pages 4) (2007).
[23] T. Nagahama, S. Yuasa, E. Tamura, and Y. Suzuki, Physical Review Letters **95**, 086602 (2005).
[24] R. Matsumoto, A. Fukushima, K. Yakushiji, S. Nishioka, T. Nagahama, T. Katayama, Y. Suzuki, K. Ando, and S. Yuasa, Physical Review B **79**, 174436 (2009).

[25] X.-G. Zhang and W. H. Butler, Physical Review B **70** (2004).

[26] R. Zeller, P. H. Dederichs, B. Ùjfalussy, L. Szunyogh, and P. Weinberger, Physical Review B **52**, 8807 (1995).

[27] N. Papanikolaou, R. Zeller, and P. H. Dederichs, J. Phys.: Condens. Matter **14**, 2799 (2002).

[28] W. Kohn and L. J. Sham, Physical Review **140**, A1133 (1965).

[29] S. H. Vosko, L. Wilk, and M. Nusair, Canadian Journal of Physics **59**, 1200 (1980).

[30] H. L. Meyerheim, R. Popescu, N. Jedrecy, M. Vedpathak, M. Sauvage-Simkin, R. Pinchaux, B. Heinrich, and J. Kirschner, Physical Review B **65**, 144433 (2002).

[31] C. Tusche, H. L. Meyerheim, N. Jedrecy, G. Renaud, A. Ernst, J. Henk, P. Bruno, and J. Kirschner, Physical Review Letters **95**, 176101 (2005).

[32] C. Heiliger, P. Zahn, B. Y. Yavorsky, and I. Mertig, Physical Review B **72**, 180406 (2005).

[33] Y. Imry and R. Landauer, Reviews of Modern Physics **71**, S306 (1999).

[34] J. Henk, A. Ernst, K. K. Saha, and P. Bruno, Journal of Physics: Condensed Matter **18**, 2601 (2006).

[35] R. A. Evarestov and V. P. Smirnov, physica status solidi (b) **119**, 9 (1983).

[36] P. Bose, I. Mertig, and J. Henk, Physical Review B **75**, 100402 (2007).

[37] E. Fawcett, Review of Modern Physics **60**, 209 (1988).

[38] V. Heine, Physical Review **138**, A1689 (1965).

[39] Y.-C. Chang, Physical Review B **25**, 605 (1982).

[40] C. Heiliger, P. Zahn, and I. Mertig, Materials Today **9**, 46 (2006).

[41] W. H. Butler, Science and Technology of Advanced Materials **9**, 014106 (2008).

[42] P. Bose, P. Zahn, J. Henk, and I. Mertig, Novel Materials and Devices for Spintronics **1183**, FF07 (2009).

[43] Since $k_\perp$ is commonly defined in units of π/a and a corresponds to an interlayer distance of 2 ML, a factor of $\pi/2$ has to be incorporated to obtain it in units of $1/\mathrm{ML}$.

[44] R. Matsumoto and S. Yuasa, private communication.

Chapter 4

Summary

Previous theoretical investigations on the tunnel magnetoresistance in planar tunnel junctions have found that the electronic transport properties are significantly affected by the properties of the interfaces. In this thesis, I present studies which investigate this important issue in more depth. The *ab initio* computations for ballistic transport rely on the Landauer-Büttiker approach, as formulated in multiple-scattering theory (layer Korringa-Kohn-Rostoker method). The addressed issues can be cast into two categories: substitutional disorder and the effect of magnetic interlayers which are embedded in Fe/MgO/Fe tunnel junctions.

Experimentally it was found that the interfaces in Fe/MgO/Fe junctions can be partially oxidized, leading to substitutionally disordered FeO_c interface layers. These have been treated within a supercell approach which allows to decompose the conductances into a specular, i. e. $\boldsymbol{k}$-conserving, and into a diffuse, i. e. not $\boldsymbol{k}$-conserving, contributions. The main result is that the specular contribution is strongly reduced, by 75 %, for an oxygen concentration of $c = 4\,\%$, as compared to the ideal junction ($c = 0$). Further, the diffuse contributions increase with disorder and show a maximum at $c = 50\,\%$. The strong reduction of the tunnel magnetoresistance (TMR) ratio for $c = 4\,\%$ strongly diminishes the mismatch of experimental and theoretical ratios, the latter obtained for ideal junctions.

The other focus in the thesis is to answer the question whether the embedding of magnetic interlayers allows to increase and to tune the tunnel magnetoresistance ratio. The importance of the magnetic properties of the interface layer was elaborated for Fe/Mn/vacuum/Fe junctions. Both the conductances and the TMR ratios show distinct 2-ML oscillations with Mn-film thickness for moderate bias voltages. These oscillations are clearly attributed to the layer-wise antiferromagnetic (LAFM) order in the Mn films. The Mn layers at the Mn/vacuum interface can be regarded as spin filters.

Replacing the homogenous vacuum barrier by a crystalline MgO barrier leads to an additional symmetry selection of the tunneling Bloch states, as is addressed for Fe/Cr/MgO/Fe. Besides the spin filter effect of the LAFM Cr films, it turned out that the complex band structure of Cr gives rise to an additional modulation of the conductances. Consequently, the thickness dependence can be regarded as a superposition of the 2-ML oscillations of the spin filter effect and an oscillations induced by damped electronic states in the Cr interlayer. The conductances for the parallel and the antiparallel configuration of the lead magnetizations are in antiphase, leading to strong oscillations in the TMR ratios.

Systematic calculations for ferromagnetic Co interlayers in Fe/MgO/Fe corroborate that the TMR ratio is not enhanced with respect to ideal Fe/MgO/Fe junctions, in contrast to experimental findings. However, a TMR maximum for five monolayer thick Co films exceeds that for Fe/MgO/Fe with partially oxidized FeO interface layers.

The investigations highlight the importance of perfect interfaces for achieving large TMR ratios. In a next step, one could apply the supercell approach for substitutional disorder to magnetic tunnel junctions with embedded interlayers, in order to improve the theoretical description even further and to predict systems with large TMR ratios.

Bibliography

[1] BAIBICH, M. N. et al., Physical Review Letters **61** (1988) 2472.

[2] BINASCH, G. et al., Physical Review B **39** (1989) 4828.

[3] WOLF, S. A. et al., Science **294** (2001) 5546.

[4] ZUTIĆ, I. et al., Reviews of Modern Physics **76** (2004) 323.

[5] WOLF, S. A. et al., IBM J. Res. Dev. **50** (2006) 101.

[6] SENEOR, P. et al., Journal of Physics: Condensed Matter **19** (2007) 165222.

[7] WINKLER, R., *Spin-orbit Coupling Effects in Two-Dimensional Electron and Hole Systems*, Springer, Berlin, 2003.

[8] JULLIERE, M., Physics Letters A **54** (1975) 225.

[9] MOODERA, J. S. et al., Physical Review Letter **74** (1995) 3273.

[10] YUASA, S. et al., Journal of Physics D: Applied Physics **40** (2007) R337.

[11] YUASA, S. et al., Nature Materials **3** (2004) 868.

[12] PARKIN, S. S. P. et al., Nature Materials **3** (2004) 862.

[13] GALLAGHER, W. J. et al., IBM J. Res. Dev. **50** (2006) 3.

[14] SLONCZEWSKI, J. C., Physical Review B **39** (1989) 6995.

[15] BUTLER, W. H. et al., Physical Review B **63** (2001) 054416.

[16] MATHON, J. et al., Physical Review B **63** (2001) 220403.

[17] MATHON, J. et al., Physical Review B **74** (2006) 140404.

[18] ITOH, H. et al., Journal of Magnetism and Magnetic Materials **303** (2006) e205.

[19] XU, P. X. et al., Physical Review B **73** (2006) 180402.

[20] MEYERHEIM, H. L. et al., Physical Review Letters **87** (2001) 076102.

[21] MEYERHEIM, H. L. et al., Physical Review B **65** (2002) 144433.

[22] TUSCHE, C. et al., Physical Review Letters **95** (2005) 176101.

[23] ZHANG, X.-G. et al., Physical Review B **68** (2003) 092402.

[24] HEILIGER, C. et al., Journal of Magnetism and Magnetic Materials **316** (2007) 478.

[25] CARVA, K. et al., Physical Review B **73** (2006) 144421.

[26] BELASHCHENKO, K. D. et al., Physical Review B **72** (2005) 140404.

[27] YUASA, S. et al., Applied Physics Letters **89** (2006) 042505.

[28] KORRINGA, J., Physics Reports **238** (1994) 341.

[29] FAULKNER, J. S., Physical Review B **19** (1979) 6186.

[30] STRANGE, P. et al., Journal of Physics: Condensed Matter **1** (1989) 2959.

[31] GONIS, A., *Theoretical Materials Science - Tracing the Electronic Origins of Materials Behavior*, Materials Research Society, Warrendale, 2000.

[32] WEINBERGER, P., *Electron Scattering Theory For Ordered And Disordered Matter*, Oxford University Press, New York, 1990.

[33] BÜTTIKER, M. et al., Physical Review B **31** (1985) 6207.

[34] IMRY, Y. et al., Reviews of Modern Physics **71** (1999) S306.

[35] SCHRÖDINGER, E., Physical Review **28** (1926) 1049.

[36] BORN, M. et al., Annalen der Physik **84** (1927) 457.

[37] BARTH, U. V., Physica Scripta **T109** (2004) 9.

[38] HOHENBERG, P. et al., Physical Review **136** (1964) B864.

[39] KOHN, W. et al., Physical Review **140** (1965) A1133 .

[40] BARTH, U. V. et al., Journal of Physics C: Solid State Physics **5** (1972) 1629.

[41] ZELLER, R., *NIC Series 31 - Spin-Polarized DFT Calculations and Magnetism*, John von Neumann-Institut für Computing, Forschungszentrum Jülich, 2006.

[42] STODDART, J. C. et al., Annals of Physics **64** (1971) 174.

[43] STODDART, J. C., Journal of Physics C: Solid State Physics **8** (1975) 3391.

[44] PAULI, W., Zeitschrift für Physik **43** (1927) 601.

[45] GUNNARSSON, O. et al., Physical Review B **13** (1976) 4274.

[46] VIGNALE, G. et al., Physical Review Letters **59** (1987) 2360.

[47] JONES, R. O. et al., Physical Review Letters **55** (1985) 107.

[48] VOSKO, S. H. et al., Canadian Journal of Physics **59** (1980) 1200.

[49] PERDEW, J. P. et al., Physical Review B **45** (1992) 13244.

[50] PERDEW, J. P. et al., Physical Review Letters **77** (1996) 1396.

[51] PERDEW, J. P. et al., Physical Review B **23** (1981) 5048.

[52] LüDERS, M. et al., Physical Review B **71** (2005) 205109.

[53] KITTEL, C., *Introduction to Solid State Physics*, Wiley & Sons, New York, 1995.

[54] FERRY, D. K. et al., *Transport in Nanostructures*, Cambridge University Press, Cambridge, 1997.

[55] IMRY, Y., *Directions in Condensed Matter Physics*, World Scientific, Singapore, 1986.

[56] DE PICCIOTTO, R. et al., Nature **411** (2001) 51.

[57] VAN WEES, B. J. et al., Physical Review B **38** (1988) 3625.

[58] IMRY, Y., *Introduction to Mesoscopic Physics*, Oxford University Press, New York, 2002.

[59] SHARVIN, Y. V., Soviet Physics JETP **21** (1965) 655.

[60] KUBO, R. et al., *Statistical Physics Vol.2 Nonequilibrium Statistical Mechanics*, Springer, Berlin, 1991.

[61] GALPERIN, Y. M., Quantum transport - lecture notes (www.freescience.info), 1998.

[62] DAS, M. P. et al., Journal of Physics: Condensed Matter **15** (2003) L687.

[63] MAEKAWA, S., *Spin Dependent Transport In Magnetic Nanostructures*, CRC Press, Boca Raton, 2002.

[64] MERTIG, I. et al., *Multiple Scattering Theory of Point Defects in Metals: Electronic properties*, Teubner-Verlagsgesellschaft, Leipzig, 1987.

[65] KORRINGA, J., Physica **13** (1947) 392.

[66] KOHN, W. et al., Physical Review **94** (1954) 1111.

[67] WILDBERGER, K. et al., Physical Review B **55** (1997) 10074 .

[68] ZAHN, P., *Screened Korringa-Kohn-Rostoker-Methode für Vielfachschichten*, PhD thesis, Technische Universität Dresden, 1998.

[69] GYORFFY, B. L., Physical Review B **5** (1972) 2382.

[70] FAULKNER, J. S. et al., Physical Review **B21** (1980) 3222.

[71] HENK, J., *Handbook of thin film materials*, volume 2, Academic Press, San Diego, 2001, Theory of Low-energy Electron Diffraction and Photoelectron Spectroscopy from Ultrathin Films.

[72] RAYLEIGH, L., Philosophical Magazine **34** (1892) 481.

[73] FAULKNER, J. S., Physical Review B **38** (1988) 1686.

[74] BLOCH, F., Zeitschrift für Physik A **52** (1928) 555.

[75] FEDER, R., *Polarized Electrons In Surface Physics*, World Scientific, Singapore, 1985.

[76] MACLAREN, J. M. et al., Physical Review B **40** (1989) 12164.

[77] MACLAREN, J. M. et al., Computer Physics Communications **60** (1990) 365.

[78] DE LACHEISSERIE, E. D. T. et al., *Magnetism: Materials and Applications*, Springer, New York, 2004.

[79] MOTT, N. H., Proceedings of the Royal Society of London **153** (1936) 699.

[80] FLOQUET, G., Ann. Ècole Norm. Sup. **12** (1883) 47.

[81] MACLAREN, J. M. et al., Physical Review B **59** (1999) 5470.

[82] ELLIOTT, R. J. et al., Reviews of Modern Physics **46** (1974) 465.

[83] FAULKNER, J. S., *The modern theory of alloys*, Pergamon Press, Oxford, 1982.

[84] SOVEN, P., Physical Review B **3** (1967) 809.

[85] SCHWARTZ, L. et al., Annals of Physics **64** (1970) 100.

[86] STOCKS, G. M. et al., Physical Review Letters **41** (1978) 339.

[87] GONIS, A. et al., Physical Review B **29** (1984) 555.

[88] MOOKERJEE, A., Journal of Physics F: Metal Physics **17** (1987) 1511.

[89] PELLA, S. et al., Physical Review B **70** (2004) 064203.

[90] ZABLOUDIL, J. et al., *Electron Scattering in Solid Matter*, Springer, Heidelberg, 2004.

[91] ROWLANDS, D. A. et al., Physical Review B **67** (2003) 115109.

[92] KÖDDERITZSCH, D. et al., New Journal of Physics **9** (2007) 81.

[93] TULIP, P. R. et al., Physical Review B **77** (2008) 165116.

[94] ABRIKOSOV, I. A. et al., Physical Review Letters **76** (1996) 4203.

[95] BUTLER, W. H., Physical Review B **31** (1985) 3260.

[96] BANHART, J., *Transporteigenschaften komplexer metallischer Systeme*, Habilitation thesis, Universität Bremen, 1997.

[97] VELEV, J. et al., Physical Review B **69** (2004) 024404.

[98] VELEV, J. et al., Journal of Applied Physics **97** (2005) 10C517.

[99] NAGAHAMA, T. et al., Physical Review Letters **95** (2005) 086602.

[100] ERNST, A. et al., Journal of Physics: Condensed Matter **17** (2005) 3269.

[101] HEILIGER, C. et al., Materials Today **9** (2006) 46.

[102] BUTLER, W. H., Science and Technology of Advanced Materials **9** (2008) 014106.

[103] MATSUMOTO, R. et al., Physical Review B **79** (2009) 174436.

[104] ZHANG, X.-G. et al., Physical Review B **70** (2004) 172407.

Danksagung

An dieser Stelle möchte ich allen herzlich danken, die zum Gelingen dieser Arbeit beigetragen haben.

Mein besonderer Dank gilt Prof. Ingrid Mertig für die interessante und herausfordernde Themenstellung und ihr Vertrauen in meine Person zur selbständigen Bearbeitung dieser Thematik. Ich bin dankbar für ihre stete Förderung in allen Phasen dieser Arbeit, die zahlreichen Diskussionen und ihre wertvollen Anregungen und Tipps.

Ganz außerordentlich dankbar bin ich PD Dr. Jürgen Henk für seine ausgezeichnete und umfassende Betreuung. Ohne seine stete Bereitschaft zur Diskussion wäre ein gutes Gelingen der vorliegenden Arbeit kaum denkbar gewesen. Ich danke ihm für die Einführung in den layer-KKR code *omni*, mit dessen Hilfe alle Ergebnisse der vorliegenden Arbeit berechnet worden sind. Neben seiner außerordentlichen fachlichen Kompetenz schätze ich auch seine freundschaftliche und offene Art.

Bei PD Dr. Peter Zahn bedanke ich mich für die Bereitstellung der selbst-konsistenten Potentialen zum 'füttern' von *omni*. Desweiteren danke ich ihm für die langen und konstruktiven Diskussionen mit vielen wertvollen Impulsen. Ich schätze sehr sein kritisches Auge für Details.

PD Dr. Arthur Ernst danke ich als meiner zweiten Quelle von selbst-konsistenten Potentialen für *omni*. Die freundschaftliche und konstruktive Zusammenarbeit mit ihm gefiel mir immer äußert gut.

Ich danke allen Mitgliedern der Fachgruppe Theoretische Physik und insbesondere meiner Arbeitsgruppe für das angenehme Arbeitsklima. Besonders danke ich Dr. Nicholas Sedlmayr und Martyna Polok für das Einfügen englischsprachiger Feinheiten in diese Arbeit.

Ohne den unermüdlichen Einsatz des Clusteradminstratorenteams bestehend aus Dr. Markus Däne, Dr. Michael Czerner und Steven Walczak wären die in dieser Arbeit vorgestellten Berechnungen nicht möglich gewesen. Vielen Dank hierfür!

Zum Schluss möchte ich meinen Freunden und meiner Familie dafür danken, dass sie mir abseits der Pfade der Physik Kraft für das Gelingen dieser Arbeit gespendet haben. Insbesondere bedanke ich mich bei meiner Liebsten Nancy, die mir in den schwierigsten Stunden aufmunternd beigestanden und unbeschreiblich viel Rückhalt gegeben hat.

Eidestattliche Erklärung

Hiermit erkläre ich, dass ich keine anderen als die von mir angegebenen Quellen und Hilfsmittel zur Erstellung meiner Dissertation verwendet habe. Den benutzten Werken wörtlich oder inhaltlich entnommene Stellen sind als solche gekennzeichnet. Ich erkläre, die Angaben wahrheitsgemäß gemacht und die wissenschaftliche Arbeit an keiner anderen wissenschaftlichen Einrichtung zur Erlangung eines akademischen Grades eingereicht zu haben.

Peter Bose

Halle (Saale), den 14. Januar 2010

Curriculum vitae

Personal data:

name	Peter Bose
address	Harz 10, 06108 Halle (Saale)
date of birth and place	08. October 1979, Lutherstadt Eisleben (Germany)

Education:

1986 - 1991	Primary school: Hans Seidel Schule Eisleben
1991 - 1998	Grammar school: Martin Luther Gymnasium Eisleben
1998 - 1999	Military service as medic
1999 - 2005	Studies of physics at Martin Luther University Halle-Wittenberg completed as graduate physicist (degree: Diplom-Physiker) Diploma title: ”Tunneln im Modell Fast Freier Elektronen” (”Tunneling in the nearly-free-electron model”)
since 2005 -	PhD Studentship at Martin Luther University Halle-Wittenberg
since 2005 -	Member of the International Max Planck Research School for Science and Technology of Nanostructures

Peter Bose

List of abbreviations

PW	plane wave
BW	Bloch wave
LKKR	layer-Korringa-Kohn-Rostoker
CPA	coherent potential approximation
UC	unitcell
SC	supercell
DFT	density functional theory
KSE	Kohn-Sham equation
MTJ	magnetic tunnel junction